

Ultrafast and Continuous-Wave Spectroscopy of Multiferroic Oxide Thin Films



Kathleen Ishbel Doig
Corpus Christi College
University of Oxford

A thesis submitted for the degree of
Doctor of Philosophy
Trinity 2014

Abstract

Thin film multiferroic oxides with co-existing ferroelectric and ferromagnetic ordering have attracted much interest in recent years, partly as a result of the enhancements achieved through the adoption of strained thin film geometries. This thesis presents work on two such thin film oxides; lanthanide substituted BiFeO_3 and Fe substituted PbTiO_3 .

Coherent magnons and acoustic phonons were impulsively excited and probed in thin films of the room temperature multiferroic $\text{Bi}_{1-x-y}\text{Dy}_x\text{La}_y\text{FeO}_3$ using femtosecond laser pulses. The elastic moduli of rhombohedral, tetragonal and rare-earth doped BiFeO_3 were determined from acoustic mode frequencies in conjunction with spectroscopic ellipsometry. A weak ferromagnetic order, induced alternately by magnetization in the growth direction or by tetragonality, created a magnon oscillation at 75 GHz, indicative of a Dzyaloshinskii-Moriya interaction energy of 0.31 meV.

Bulk crystals and thin films of $\text{PbTi}_{1-x}\text{Fe}_x\text{O}_3$ (PTFO) are multiferroic, exhibiting ferroelectricity and ferromagnetism at room temperature. Here we report that the Ruddlesden-Popper phase $\text{Pb}_{n+1}(\text{Ti}_{1-x}\text{Fe}_x)_n\text{O}_{3n+1-\delta}$ forms spontaneously during pulsed laser deposition of PTFO on LaAlO_3 substrates. High-resolution transmission electron microscopy, x-ray diffraction and x-ray photoemission spectroscopy were utilised to perform a structural and compositional analysis, demonstrating that $n \simeq 8$ and $x \simeq 0.33$. The complex dielectric function of the films was determined from far-infrared to ultraviolet energies using a combination of terahertz time-domain spectroscopy, Fourier transform spectroscopy, and spectroscopic ellipsometry. The simultaneous Raman and infrared activity of phonon modes, and the observation of second harmonic generation, establishes a non-centrosymmetric point group for $\text{Pb}_{n+1}(\text{Ti}_{0.67}\text{Fe}_{0.33})_n\text{O}_{3n+1-\delta}$ consistent with ferroelectricity. No evidence of macroscopic ferromagnetism was found in SQUID magnetometry. The ultrafast optical response exhibited coherent magnon oscillations compatible with local magnetic order, and additionally was used to study photocarrier cooling on picosecond timescales. An optical gap smaller than that of BiFeO_3 and long photocarrier lifetimes may make this system interesting as a ferroelectric photovoltaic.

Publications

1. **K. I. Doig**, F. Aguesse, A. K. Axelsson, N. M. Alford, S. Nawaz, V. R. Palkar, S. P. P. Jones, R. D. Johnson, R. A. Synowicki, J. Lloyd-Hughes. *Coherent magnon and acoustic phonon dynamics in tetragonal and rare-earth-doped BiFeO₃ multiferroic thin films*. Phys. Rev. B, **88**, 9, 094425, September 2013.
2. J. Lloyd-Hughes, S. P. P. Jones, E. Castro-Camus, **K. I. Doig**, J. L. MacManus-Driscoll, *Modifying the polarization state of terahertz radiation using anisotropic twin-domains in LaAlO₃*. Opt. Lett., **39**, 5, 1121-1124, March 2014.
3. S. P. P. Jones, S. M. Gaw, **K. I. Doig**, D. Prabhakaran, E. M. Hetroy Wheeler, A. T. Boothroyd, J. Lloyd-Hughes. *High-temperature electromagnons in the magnetically induced multiferroic cupric oxide driven by intersublattice exchange*. Nat. Commun., **5**, 3787, April 2014.
4. **K. I. Doig**, J. J. P. Peters, S. Nawaz, D. Walker, M. Walker, M. R. Lees, A. M. Sanchez, C. F. McConville, V. R. Palkar, J. Lloyd-Hughes. *Structural, optical and vibrational properties of self-assembled Pb_{n+1}(Ti_{1-x}Fe_x)_nO_{3n+1} Ruddlesden-Popper superstructures*. Sci Rep, 2014 (Under Review)

Acknowledgements

It is as a result of the support and encouragement that I have received from many individuals that I am able to present this thesis. It is my pleasure to be able to thank them now.

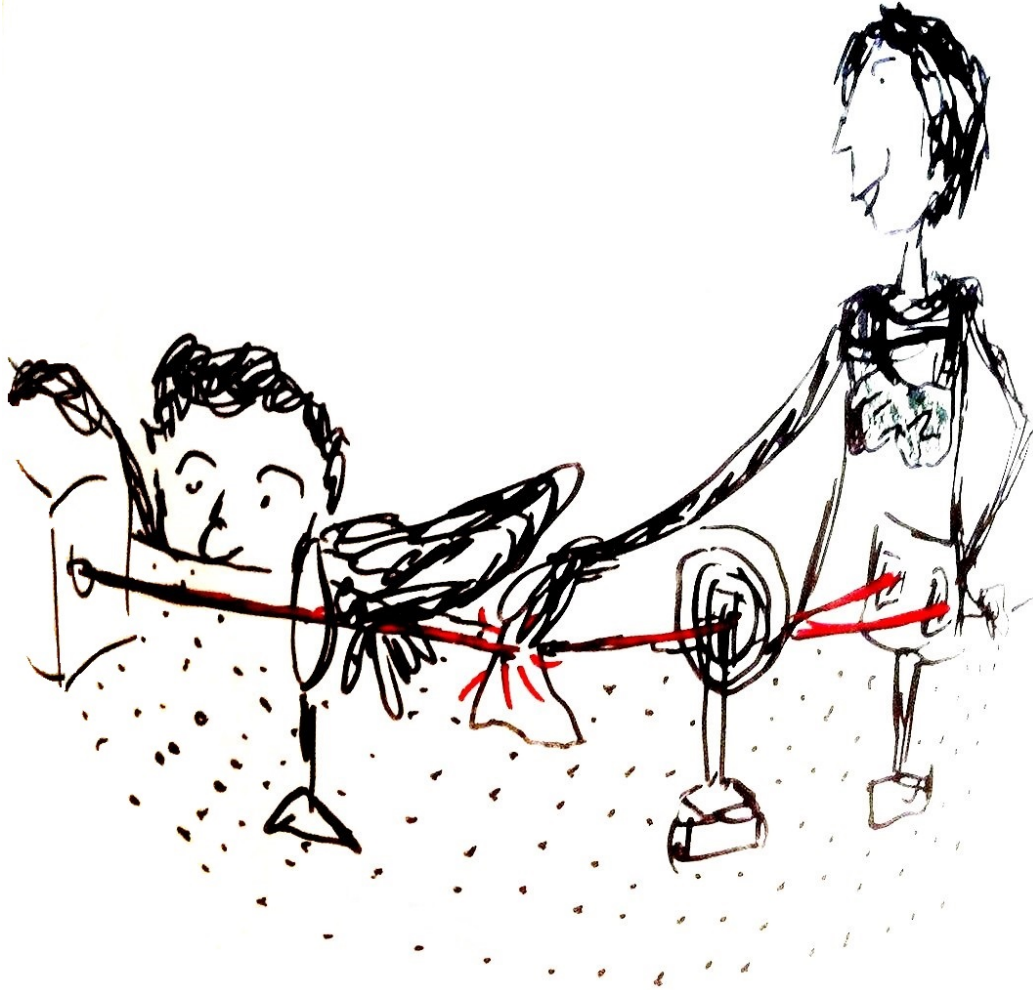
Firstly, I would like to thank my supervisor, Dr. James Lloyed-Hughes. It is thanks to much dedication on his part that I have been able to produce the work I present here at all. I would also like to thank Dr. Michael Johnston for sharing his lab with us so amicably over the last four years and for all the help and encouragement he has given me since my first arrival in Oxford. It is also with great thanks to a large number of colleagues who have both helped me in my work and have been extent friends to me. I would like to take this opportunity to thank Sam Jones, Christian Wehrenfennig, Chris Menelaou, Jack Alexander-Webber and Hannah Joyce, for the numerous occasions they have helped with experiment or to solve various problems and who have on many occasions simply made my day more enjoyable.

There are also a large number of people without whose contributions this would not have been possible. I would like to thank M. Schubert, T. Dekorsy and C. He for allowing me to carry out ASOPS measurements in Konstanz. D. Walker for helping me with X-ray. J. Bowen and R. A. Synowicki for helping me with Ellipsometry. F. Aguesse, N. M. Alford, A. K. Axelsson, S. Nawaz and V. R. Palkar for providing me with samples. J.J.P.Peters, R.Beanland, A.M.Sanchez, M.Walker, C.F.McConville, M.R.Lees for undertaking TEM,XPS and SQUID measurements to aid my study.

I have been lucky to have shared my time in Oxford with some fantastic friends. I would like to give a particular note of thanks to my friends in the OUCB and the coaches and players of the OWWPC. In addition to those I have already thanked I would also like to thank Iona, Peggy and Simone for their constant friendship.

Finally I would like to express my immense gratitude and love for parents, grandparents and extended family. Everything I have done is because of their love and support and they make my life an extremely happy one. And to Christian, I thank for all your love and support and for all the happiness you have brought me.

Gu mo luchd-gaoil le sòlas is taing.



Contents

Abstract	ii
Publications	iv
Acknowledgements	vi
1 Introduction	1
1.1 Multiferroics	1
1.2 Lanthanide Substituted BiFeO ₃	5
1.2.1 BiFeO ₃	5
1.2.2 Bi _(1-x) Re _x FeO ₃	8
1.3 Fe Substituted PbTiO ₃	14
1.3.1 PbTiO ₃	14
1.3.2 PbTi _{1-x} Fe _x O ₃	16
1.4 Optical Techniques Applied to Multiferroics	18
1.4.1 Excitations	19
1.4.2 Transient Reflectivity	22
1.4.3 Ellipsometry	25
1.4.4 SHG	26
1.4.5 THz	29
1.4.6 Raman Spectroscopy	30
2 Experimental Methods & Theoretical Background	33
Transient Techniques -----	33
2.1 Optical Pump Probe Reflectivity	33
2.1.1 Experimental Setup	34
2.1.2 Coupling Mechanisms	38
2.1.3 Magnons	42
Linear and Non-linear Optical Techniques -----	42

2.2	Ellipsometry	42
2.2.1	Absorption Depth	44
2.3	Second Harmonic Generation (SHG)	44
	Vibrational Mode Techniques _____	45
2.4	THz Time-Domain Spectroscopy (THz-TDS)	45
2.5	Fourier Transform IR Spectroscopy (FTIR)	49
2.6	Raman Spectroscopy	50
3	Coherent magnon and acoustic phonon dynamics in tetragonal and rare-earth-doped BiFeO₃ multiferroic thin films	52
3.1	Introduction	52
3.2	Sample characterization	53
3.2.1	Growth and X-ray Diffraction	53
3.2.2	Ellipsometry and DFT	56
3.2.3	Second Harmonic Generation	57
3.3	Time-Resolved Reflectivity	62
3.4	Elastic Moduli and Acoustic Phonons	64
3.4.1	Acoustic Phonon Contribution to Reflectivity Change	64
3.4.2	Elastic Properties of Anisotropic BiFeO ₃	65
3.4.3	Results and Discussion	67
3.5	Magnon Resonance	70
3.5.1	Magnetic Field Dependence	70
3.5.2	Temperature Dependence	71
3.5.3	Wavelength Dependence	73
3.5.4	Influence of Substrate	74
3.5.5	Magnon Mode Evolution and Pump Fluence	76
3.5.6	Magnon Resonance: Discussion	77
3.6	Conclusions	80
4	Structural, optical and vibrational properties of self-assembled Pb_{n+1}(Ti_{1-x}Fe_x)_nO_{3n+1} Ruddlesden-Popper superstructures	81
4.1	Introduction	81
4.2	Structure and composition	82
4.2.1	Sample Growth	82
4.2.2	Transmission Electron Microscopy	83
4.2.3	XPS	85
4.2.4	X-Ray	87

4.2.5	Magnetization Measurement	91
4.3	Linear and non-linear optics in the visible-UV	93
4.3.1	UV-Vis	93
4.3.2	Ellipsometry	94
4.3.3	Second Harmonic Generation	97
4.4	Ultrafast Optical Reflectivity	100
4.4.1	Electronic Component	100
4.4.2	Oscillatory Component	104
4.5	IR active phonons	105
4.5.1	FTIR	105
4.5.2	THz Time-Domain Spectroscopy	107
4.5.3	Raman active phonons	109
4.5.4	Vibrational Modes in LaAlO ₃ Substrate	112
4.6	Conclusions	114
5	Conclusions	115
	Bibliography	117

Chapter 1

Introduction

1.1 Multiferroics

Multiferroics are materials that exhibit two or more forms of ferroic ordering in a single homogeneous phase [1, 2]. There are four types of ferroic ordering: ferroelectric, which has a stable electric polarisation \mathbf{P} that can be switched hysteretically by the application of an external electric field \mathbf{E} ; ferromagnetic, which has a stable magnetisation \mathbf{M} that can be switched hysteretically by an external magnetic field \mathbf{M} [3]; ferroelastic, which has two or more orientation states with different spontaneous strain that can be switched by mechanical stress; and the more recently observed ferrotoroidic, which fulfils the missing criteria of breaking both space-inversion and time reversal symmetries [4]. Multiferroics exhibiting simultaneous ferroelectric and ferromagnetic ordering have been of particular interest because of the magnetoelectric coupling between ferroelectric and magnetic orderings that exists in some ferroelectric ferromagnetic multiferroics [1]. In magnetoelectric multiferroics, the magnetisation and electrical polarisation are strongly coupled [1, 5, 6, 7], which makes them of great potential for application. Figure 1.1 shows a schematic representation of the ordering types associated with ferroelectric-ferromagnetic multiferroics and magnetoelectrics.

The coexistence of magnetic and electric ordering is relatively uncommon owing to the paradoxical nature of their common underlying mechanisms [3]; ferroelectricity generally requiring empty d-orbitals while ferromagnetic ordering generally requires

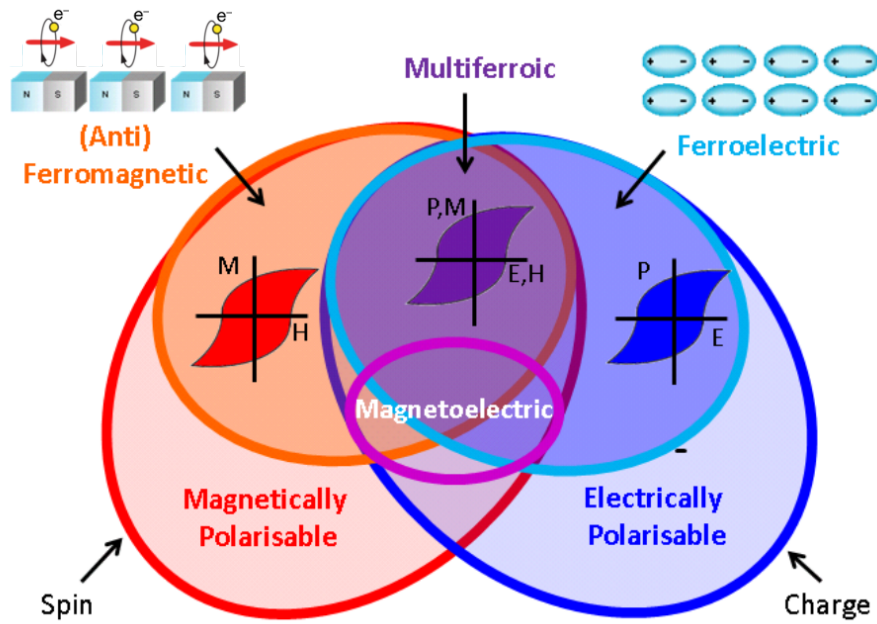


Figure 1.1: Schematic representation of the relationship between multiferroic and magnetoelectric materials. Ferromagnets (orange shading), which have a magnetic hysteresis, are a subset of magnetically polarizable materials (red shading), where spins are ordered. The equivalent is true for Ferroelectrics, which have an electric hysteresis, and are a subset of electrically polarisable materials where charge is ordered (blues). Where these orders occur simultaneously materials are multiferroic (represented by the purple shading in the intersection region). Multiferroics where magnetoelectric coupling can occur form a subset of multiferroics. Magnetoelectric coupling (represented by the pink circle) is an independent phenomenon that can, but need not, arise in any of the materials that are both magnetically and electrically polarizable. In practice, it is likely to arise in all such materials, either directly or via strain. [Adapted from [2]]

partially filled d-orbitals [1]. As such, in order for multiferroism to be achieved the atoms that move off centre to form a electric dipole have to be different from the ones that carry the magnetic moment. This requires an alternative mechanism for either ferroelectricity or ferromagnetism. No such mechanism for magnetism (i.e. non-d) has been determined, however, a number of different approaches have been employed to achieve alternative mechanisms for ferroelectricity. Type I multiferroics are materials where the mechanisms for the two order parameters are independent. Routes to achieving simultaneous ferroelectric and ferromagnetic multiferroics can be split

into two types. Multiferroics of this type generally have high spontaneous polarisations ($10\text{-}100\mu\text{cm}^{-2}$) and high ($\geq 100\text{ K}$) ferroelectric and ferromagnetic transition temperatures, but often suffer from poor coupling between the order parameters [8]. An example of these are where magnetic perovskite structures achieve multiferroism by stereochemical activity of the lone pair on the (A-site) cation while, keeping the small (B-site) cation magnetic, as is the case in BiFeO_3 [6]. It is multiferroics of this type that will be under consideration in this thesis. In Type II multiferroics the ferroelectricity is caused by magnetic ordering. These materials often have low transition temperatures ($\sim 10\text{ K}$) and weak polarisations ($\sim 0.01\mu\text{Ccm}^{-2}$), but with strong coupling between the order parameters [8]. Examples of this type of multiferroic include where ferroelectricity, which is compatible with the coexistence of magnetism, is geometrically driven. This is the case in the highly studied rare earth manganates (Re-MnO_3) [5, 9]. Symmetry-lowering magnetic ground states and non-centrosymmetric charge ordering arrangements have also been used to alter the ferroelectric mechanism to allow multiferroism [7].

The magneto-electric effect was first predicted in 1959 [10] and experimentally verified the following year [11]. However, it has been the last ten years that has seen a surge in interest in multiferroics. The reasons for this have been three fold; the production of high-quality single-crystal samples, improved first principle calculation techniques and advances in thin-film growth techniques. This latter approach has provided routes to structures and phases that are inaccessible by traditional chemical means, and have allowed the properties of existing materials to be modified by strain engineering [7, 12]. Single-component thin film approaches have been in two classes of multiferroics (hexagonal manganites and Bi-based perovskites) while horizontal and vertical multilayer structures have also been developed creating artificially engineered magnetoelectrics. Various measurement techniques, such as TEM, x-ray and neutron diffraction have been employed to study the structures and properties of multiferroics.

In magnetoelectric multiferroics where ferroelectric and ferromagnetic orders are strongly coupled there is the possibility of being able to control the ferroelectric polarisation using a magnetic field and conversely, manipulating the magnetization using an electric field. This gives the potential for various applications such as electrically (rather than magnetically) tuneable microwave applications such as filters, oscillators and phase shifters [13], spintronic devices and magnetic data storage such as magnetoelectric RAMs which drastically reduce the writing energies required [14]. Coupled ferroelectric and ferromagnetic orders provide additional possibilities for device design, such as the development of 4-state resistive memory devices ($\mathbf{P} \uparrow, \mathbf{P} \downarrow, \mathbf{M} \uparrow, \mathbf{M} \downarrow$) [15]. There is also potential for application as capacitors, transducers and actuators [16]. Ferroelectric photovoltaics are an emerging area of interest as, unlike traditional semiconductor p-n junctions, ferroelectric materials can generate photovoltages above their band gap [17].

Structure of Thesis: The rest of this chapter is divided into three sections. The first two of these, Section 1.2 and 1.3, will outline some relevant background details and literature on the two material systems studied in this thesis. Section 1.2 examines lanthanide substituted BiFeO_3 while Section 1.3 discusses Fe substituted PbTiO_3 , which have both been reported as perovskite multiferroics at room temperature. The final Section of this chapter, Section 1.4 outlines some background literature on optical techniques that give helpful insight into the phenomena that methods couple to, focusing on those that are relevant in the study of multiferroics in bulk and thin film. Chapter 2 sets out the experimental techniques and theoretical background for the optical techniques used in this thesis. The methods discussed are Optical Transient Reflectivity, Spectroscopy Ellipsometry, Second Harmonic Generation, Terahertz time-domain spectroscopy, Fourier Transform Infrared spectroscopy and Raman Spectroscopy. Chapters 3 and 4 present the results and discussion on the two material systems examined; 3 - lanthanide substituted BiFeO_3 and 4 - Fe

substituted PbTiO_3 .

1.2 Lanthanide Substituted BiFeO_3

1.2.1 BiFeO_3

Bismuth ferrite (BFO) is one of the few room temperature multiferroics, with magnetic ordering below the Néel temperature, $T_N=643$ (370°C) and ferroelectric ordering up to the Curie temperature $T_C=1103\text{K}$ (830°C). As such has been studied extensively [18] since the first demonstration of thin-film BFO in 2003 [6]. In the bulk phase, ferroelectricity arises from a rhombohedral distortion to the perovskite structure: the $6s^2$ lone pair on Bi^{3+} creates a polarisation along $[111]_{pc}$ in the pseudocubic setting (pc), with a concomitant tilt of the oxygen octahedra. The G-type antiferromagnetic order on the $3d^5$ Fe^{3+} sites is disrupted by a weak ferromagnetic component. The Fe-O-Fe chain has no centre of symmetry, resulting in the canting of adjacent spins via the Dzyaloshinskii-Moriya (DM) interaction [18, 19]. However, in bulk crystals of BFO, a long range spin cycloid [20] along $[10\bar{1}]_{pc}$ (spin rotations in $(\bar{1}2\bar{1})$ plane) with a wavelength of 64 nm averages the weak ferromagnetic moment to zero. These aspects of the structure of BFO are summarised in Figure 1.2.

Dzyaloshinskii-Moriya Interaction: The Dzyaloshinskii-Moriya interaction or antisymmetric exchange is a contribution to the total magnetic exchange interaction between two neighbouring magnetic spins. It was first proposed by Dzyaloshinskii to phenomenologically modify the Hamiltonian to account for a modification of the superexchange by the spin-orbit coupling. This modification can be written as:

$$\mathcal{H}_{DM} = \mathbf{D}_{ij} \cdot (\mathbf{S}_i \times \mathbf{S}_j) \quad (1.1)$$

where \mathbf{S}_i and \mathbf{S}_j are neighbouring magnetic spins and \mathbf{D}_{ij} is the Dzyaloshinskii vector [21, 22]. The exchange between the spins of transition metals is usually medi-

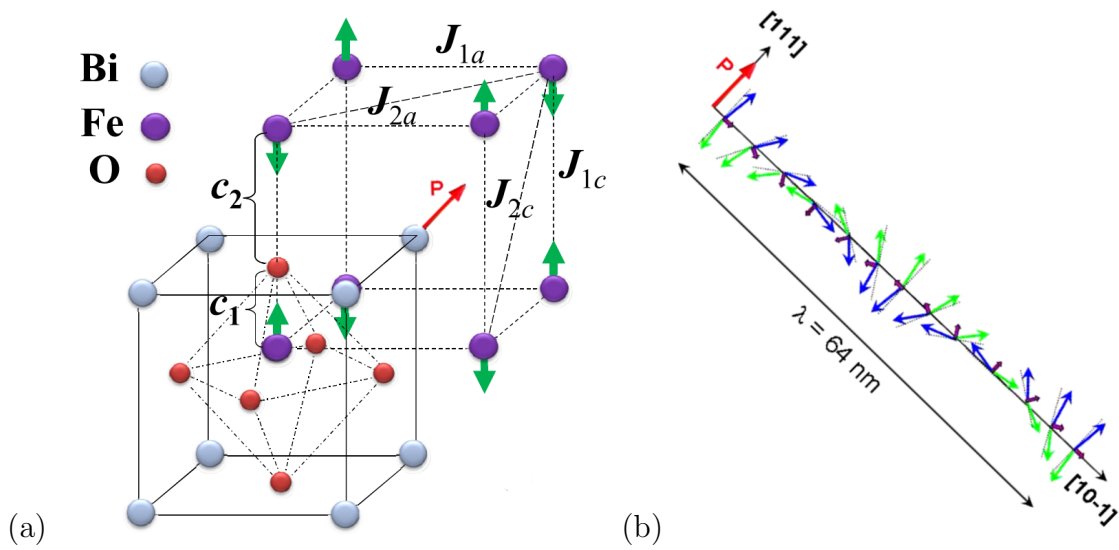


Figure 1.2: (a) Structure of BFO in the pseudocubic setting, highlighting the G-type antiferromagnetic (AFM) order on the Fe sites. The ferroelectric polarisation (P) is along [111]. (b) Blue and green arrows indicate the canting for spins of adjacent Fe sites, where the smaller purple arrows are the resulting weak ferromagnetic moment. The spin orientations of the circular cycloid along [10-1] is also shown. [Figures (a) and (b) reproduced from [23] and [24] respectively.]

ated by a third ion (a ligand); in the case of BiFeO_3 the Oxygen ion. The Dzyaloshinskii vector, \mathbf{D}_{ij} is proportional to $\mathbf{r} \times \mathbf{x}$, where \mathbf{r} is the vector between the two adjacent spins and \mathbf{x} is the vector between the midpoint of the spins and the ligand. This means that where the centre of symmetry of a system is broken that the energy of the system can be reduced if spins align away from the parallel, i.e. if they cant. The canting of spins then results in a weak ferromagnetism in the material. In BiFeO_3 the canting of spins via the DM interaction comes about because of the breaking of the ferroelectric polarization breaks the centre of symmetry[18]. The DM interaction can also describe the inverse effect, where cycloid magnetic ordering can reduce the interaction energy by causing ionic shifts, resulting in a ferroelectric polarisation[85].

Drawbacks of BiFeO_3

BiFeO_3 , however, suffers from various drawbacks which hinder its application, hence much of the current research on the material has been devoted to overcoming these.

BiFeO₃ suffers from a high leakage current, attributed to the small amounts of Fe²⁺ ions and oxygen vacancies [25], which is detrimental to its ferroelectric functionality. In contrast to the strong magnetoelectric coupling observed for multiferroics such as RMnO₃, where polarisation stems directly from magnetic order [5], static magnetoelectric coupling in BFO is weak as ferroelectric and antiferromagnetic orders originate from different ions. In the bulk phase, BiFeO₃ has a long-range spin cycloid [20] with a wavelength of 64 nm that averages the weak ferromagnetic moment to zero and prohibits the linear magnetoelectric effect in bulk [18]. While the application of a large magnetic field (20 T) can suppress the cycloid and recover a linear magnetoelectric effect [26], epitaxial strain [6] and chemical doping [27, 28] have been explored as routes to obtain stronger coupling at lower magnetic fields.

Overcoming the Drawbacks

The approach to overcoming all of these drawbacks and the root to general enhancement of the functional properties of the material revolves around epitaxial strain and ionic substitution. Straining through thin film geometry [6] and the construction of composite materials [7] have been explored as routes to both improve the individual functional orderings as well as their cross-coupling. Although initial reports appeared to suggest improvements to both ferroelectric and ferromagnetic component [6] later some doubt was cast over the enhancements in the magnetic properties achieved [29, 30]. It has been shown that, rather than geometry, impurity phases play a critical role in the enhancements observed in the ferromagnetic component. Irrespective of strain, there is virtually no magnetic moment in BiFeO₃ and it is an additional γ -Fe₂O₃ phase that is entirely responsible for the magnetic moment in the films [31]. The γ -Fe₂O₃ phase is a ferromagnetic material with high $T_C \sim 850\text{K}$ [32]. The spin cycloid, which can be suppressed under high magnetic fields [33, 34], can also be suppressed through either ionic substitution [35, 36] or strain [37]. The suppression of the spin cycloid restores the weak ferromagnetic component. The electric-field

control of magnetism at room temperature by the conversion of the magnetic cycloid into a homogeneous state by application of an external electric field has also been shown to be possible [38]. Improvements to leakage current have been achieved through substituting Fe^{3+} with higher valence ions to fill oxygen vacancies and reduce the formation of Fe^{2+} [36, 39, 40]. Enhanced processing techniques with high heating rates and short sintering periods have also been employed to suppress the leakage current [25].

1.2.2 $\text{Bi}_{(1-x)}\text{Re}_x\text{FeO}_3$

The partial substitution of Bi on the perovskite *A*-site with lanthanides (Re¹) has been explored as a route to enhance the remnant polarisation, saturation magnetisation and the coupling between the two orders [41, 42, 43, 44, 45, 46]. In this work BFO substituted with Dy and both Dy and La have been studied.

Among the lanthanides Dy^{3+} has a relatively high magnetic moment (electron configuration $[\text{Xe}]4f^9$) yielding a greater magnetisation both in bulk and thin films [47]. La^{3+} is non-magnetic (electron configuration $[\text{Kr}]4d^{10}5s^25p^6$). The reason for the simultaneous addition of La and Dy is that it is known that BFO with a perovskite structure has a significantly reduced leakage current, but that the temperature window for obtaining the perovskite phase is very narrow [48]. La substitution is thought to reduce leakage current [49].

An initial study of Dy substituted BiFeO_3 was undertaken by Murashov *et. al.* in 1990 [50]. Solid solutions samples of $\text{Bi}_{(1-x)}\text{ReFeO}_3$ where $\text{Re}=\text{La}_{x=0.55}$, $\text{Gd}_{x=0.45}$ and $\text{Dy}_{x=0.55}$ were examined. A non-linear response of the magnetic field induced electric charge with applied magnetic-field-indicated a linear magnetoelectric effect at low temperature. The effect was particularly pronounced in the case of Dy substitution and was the only sample to show the effect at higher temperature (77 K). Hysteresis

¹The lanthanide are the fifteen metallic elements with atomic numbers 57-71. These along with the chemically similar elements scandium and yttrium, are often collectively known as the rare earth elements (Re))

in the electric charge with applied magnetic field was also seen for BDFO.

The next studies on this material looked at the dielectric response at sub-microwave [51] and microwave frequencies [28, 40]. For the microwave frequencies this was undertaken with a view to addressing the issue of the lack of multiferroic material properties reported at higher than a few MHz, especially in thin films, because of the high leakage current in these materials. In particular the tenability of capacitance (defined as $(C(0V)-C(100V))/C(0V)$) was examined. This was found to be enhanced for BiFeO₃ thin films with the addition of both La and Dy in comparison to Dy alone and for MgO substrates in comparison to LaAlO₃ ones. The presence of La was also seen to weaken the magnetic response of the system.

The first clear evidence of the presence of both ferroelectric and ferromagnetic orders was seen in BFO doped with both Dy_(x=0.3) and La_(y=0.1) thin films on Pt/TiO₂/SiO₂/Si substrates [27]. It was later seen that the magnetic properties were enhanced with the removal of La. Enhancements were also observed for both Dy substituted and dual Dy-La substituted samples in thin film compared to the bulk [52]. This can be seen from Figure 1.3(a). However in a film thickness dependent study in the range 100-500 nm neither the magnetic nor ferroelectric properties appeared to scale with the film thickness [53].

Evidence of magnetoelectric coupling has also been seen in BDFO. Increases in the ferroelectric remnant and saturation polarisation with the application of an external magnetic field were observed (See Figure 1.3(b)) [54]. This effect was seen to have some dependence on the concentration of the Dy present, with $x < 0.07$ not showing this effect [58]. Changes in the magnetic domain structure with applied electric field have also been demonstrated. A short zigzag domain structure was seen to elongate into striped domains with applied voltage (See Figure 1.4(a)). The change to the domain structure was retained after removal of the applied bias, indicating an electric field controlled hysteresis. Confirmation of the absence of leakage current in the films

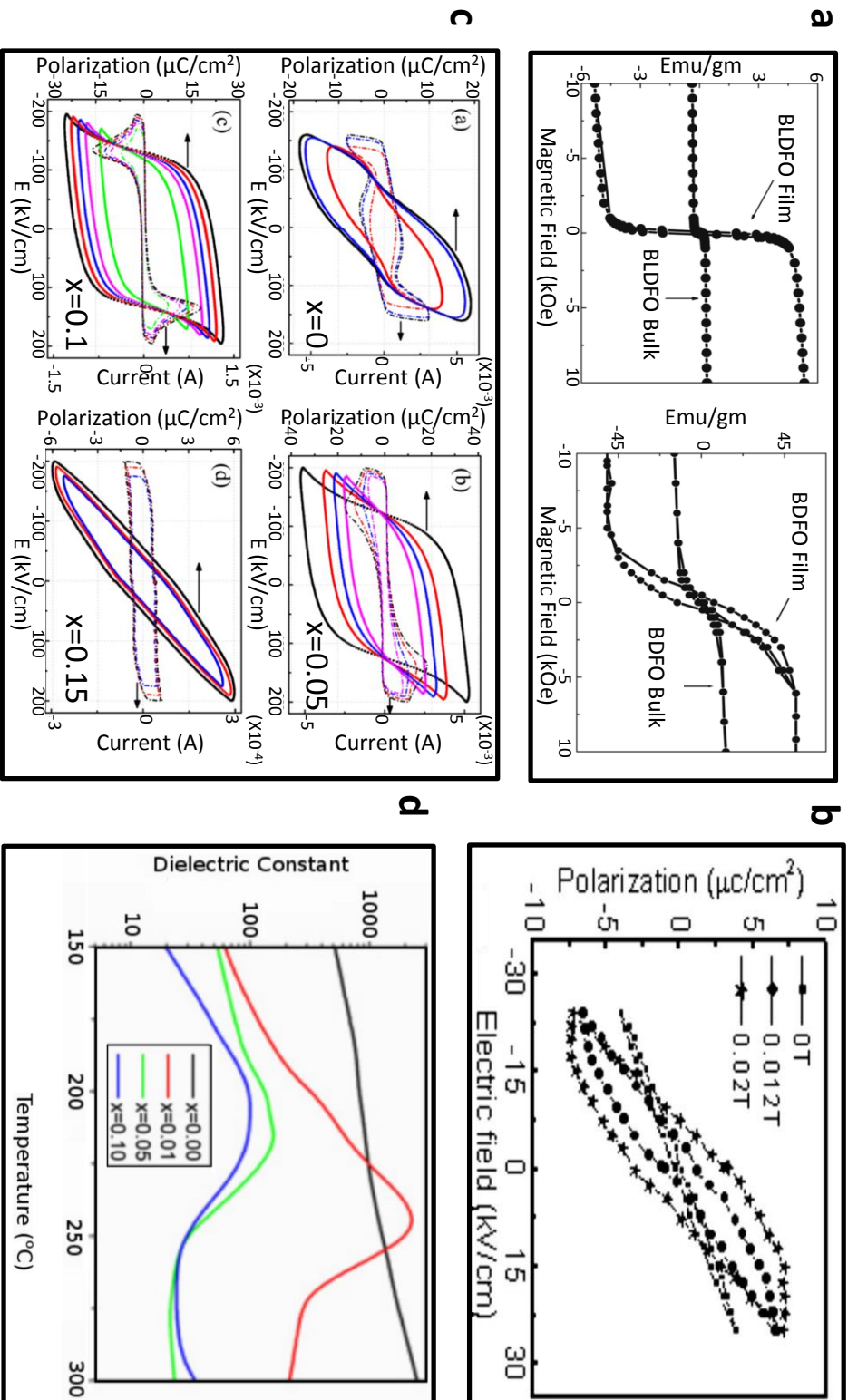


Figure 1.3: **BDFO Literature:** (a) M-H curves obtained for bulk and thin films of BLDFO and BDFO samples using vibrating sample magnetometer at room temperature [52]. (b) Effect of dc magnetic field on ferroelectric hysteresis loop of BDFO thin film [54]. (c) Ferroelectric polarization and displacement current vs electric field as measured for $\text{Bi}_{1-x}\text{Dy}_x\text{FeO}_3$ [55]. (d) Dielectric constant versus temperature curves of $\text{Bi}_{1-x}\text{Dy}_x\text{FeO}_3$ at 10 kHz [56]. [All Figures and Captions re-produced from literature as indicated by citation]

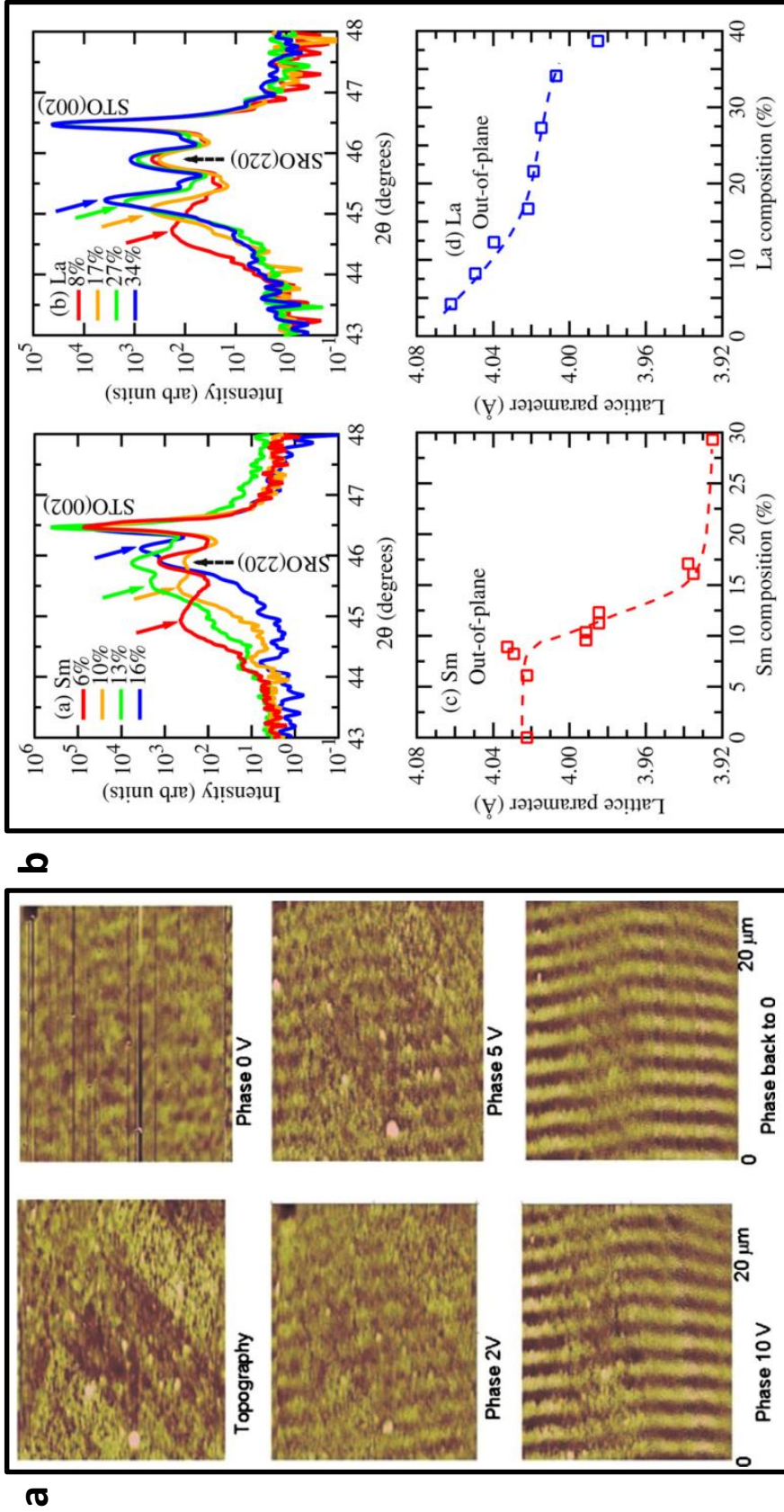


Figure 1.4: **BDFO Literature:** (a) Topography and magnetic domain imaging using MFM at different applied voltages for BDFO thin film [54]. (b) (a)-(b) X-ray 2θ - θ profiles across the structural phase transition for (a) Sm- and (b) La-substituted BFO thin films at room temperature. Coloured solid arrows denote $(002)_{pc}$ reflections from RE-substituted BFO layer. (c)-(d) substitution-induced evolution of the out-of-plane lattice parameter d_{001-pc} determined from the $(002)_{pc}$ reflection for (c) Sm- and (d) La-substituted BFO [57]. [All Figures and Captions re-produced from literature as indicated by citation]

ruled out that the effect actually arises from the current developed due to the applied voltage [54].

Numerous studies have shown that increasing the concentration of Dy improves the Magnetisation saturation [55, 58, 59, 60, 61]. This is associated with the suppression of the spin-cycloid. It has been seen that changing the substitution level can cause changes in the crystal structure and lattice parameters. As Dy is increased, although it initially increases, reductions in the saturation polarisation have been observed above a certain point. An example of this can be seen in Figure 1.3(c) where at the highest concentration the clear hysteresis of the lower samples has broken down. This effect has been associated with a structural transition from rhombohedral to orthorhombic [55, 57]. The orthorhombic phase is more centrosymmetric which is what degrades the ferroelectric response. The origin of this structural change has been attributed to ionic size. This was evident from the different behaviour of the lattice contents for La^{3+} and $\text{Dy}^{3+}/\text{Gd}^{3+}/\text{Sm}^{3+}$ substituted BFO. This is demonstrated by the concentration dependent X-ray data shown in Figure 1.4(b). With increasing Sm substitution a jump in the $(002)_{pc}$ (indicated by the arrows) reflection peak can be seen on transition to the orthorhombic phase between 13% and 16%. In contrast La substitution gives a gradual shift of this peak. The behaviour for Dy and Gd substitution, both of which have smaller ionic radii than Sm, followed a similar pattern to that of Sm. Combined with a temperature dependant study, these results were used to construct phase diagrams for different rare earth dopants. The leakage current has also been seen to follow the same trend with Dy substitution; i.e. it improves with concentration up until the structural transition [55].

Another effect that, in some cases, has been observed with increasing Re-substitution and the in perovskite BFO along with the structural transition from the ferroelectric rhombohedral phase to an orthorhombic phase is the emergence of a double-ferroelectric-polarization hysteresis loop [57]. This process has been seen

to occur independent of the RE dopant species. First principles calculations have suggested that the origin of the double hysteresis loop and the associated enhancement in the piezoelectric coefficient is an electric-field-induced transformation from a paraelectric orthorhombic phase to the polar rhombohedral phase [62].

Temperature dependent dielectric measurements have shown that the Neel temperature for magnetic ordering (T_N) reduces with Dy substitution. Over the range of $0.01 \leq x \leq 0.1$ T_N was seen to drop from 250° C to 200°C, which is much reduced compared to $T_N=370^\circ\text{C}$ of the unsubstituted phase [56] (see Figure 1.3(d)). Magnetic annealing during the sample preparation has also been seen to have an effect on the ferroelectric polarisation. Although no effect is observed for pure BFO, for Dy-substituted BFO this process enhances the polarisation. No effect on the magnetic properties was observed with annealing [63].

Optical Studies

There has previously been very little optical characterisation of Dy substituted BiFeO_3 carried out. Most of the studies that have been done present Raman or FTIR spectra as a mainly qualitative auxiliary to X-ray structural characterisation [51, 63, 64]. There has however been one more in-depth study of the lattice and spin dynamics of $\text{Bi}_{1-x}\text{Dy}_x\text{FeO}_3$ nanoparticles in the range $0 \leq x \leq 0.4$ using FTIR and Raman which gives insight into the tailoring of the structural and magnetic properties by chemical substitution multiferroic [65]. The linewidths of their observed phonon peaks were found to broaden with increasing Dy concentration. This reflects an increase in local lattice disorder. A significant change in the phonon parameters, was seen to occur at $x=0.15$, which corresponds to the structural transition from rhombohedral to orthorhombic. They also report the observation of a two-magnon excitation with increasing Dy substitution. Factors supporting this assignment include that the substitution dependence of the frequency for one of the observed modes is consistent with shifts observed in other rare earth substituted BFO. In other systems this has been

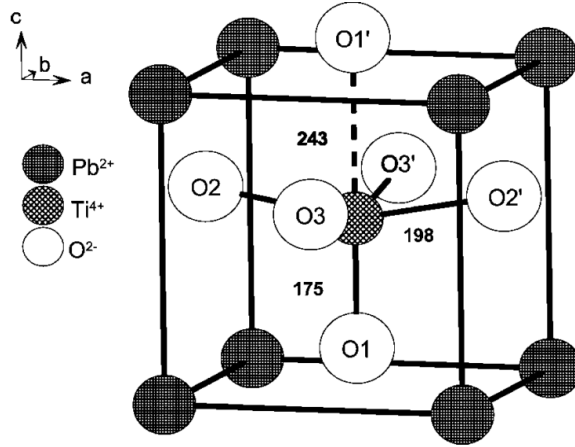


Figure 1.5: Schematic representation of the tetragonal unit cell of PbTiO_3 with designation of the different oxygen sites. The experimental atomic distances for the Ti site to the surrounding oxygen octahedra are given in pm. [Figure from [66]]

attributed to transformation from cycloidal to canted antiferromagnetic state. Furthermore Raman-active phonons of pure BiFeO_3 behave anomalously above the 640K antiferromagnetic transition temperature, while Dy substitution disrupts the lattice-spin interactions at high temperatures. They also observed a chemically enhanced dielectric constant.

1.3 Fe Substituted PbTiO_3

1.3.1 PbTiO_3

PTFO is a displacive ferroelectric [67] that exhibits a tetragonal bulk phase with space group $P4mm$ [68, 69]. Ferroelectric polarisation arises from the displacement of Ti^{4+} ions with respect to the surrounding oxygen ions. The oxygen octahedron is elongated and shifted along the c -direction, with respect to Pb^{2+} ions, as illustrated in Figure 1.5. The ionic radii of Pb and Ti, respectively on the A- and B- sites are 1.63 \AA and 0.605 \AA [70]. PbTiO_3 has long been of great interest as it has a particularly large polarisation.

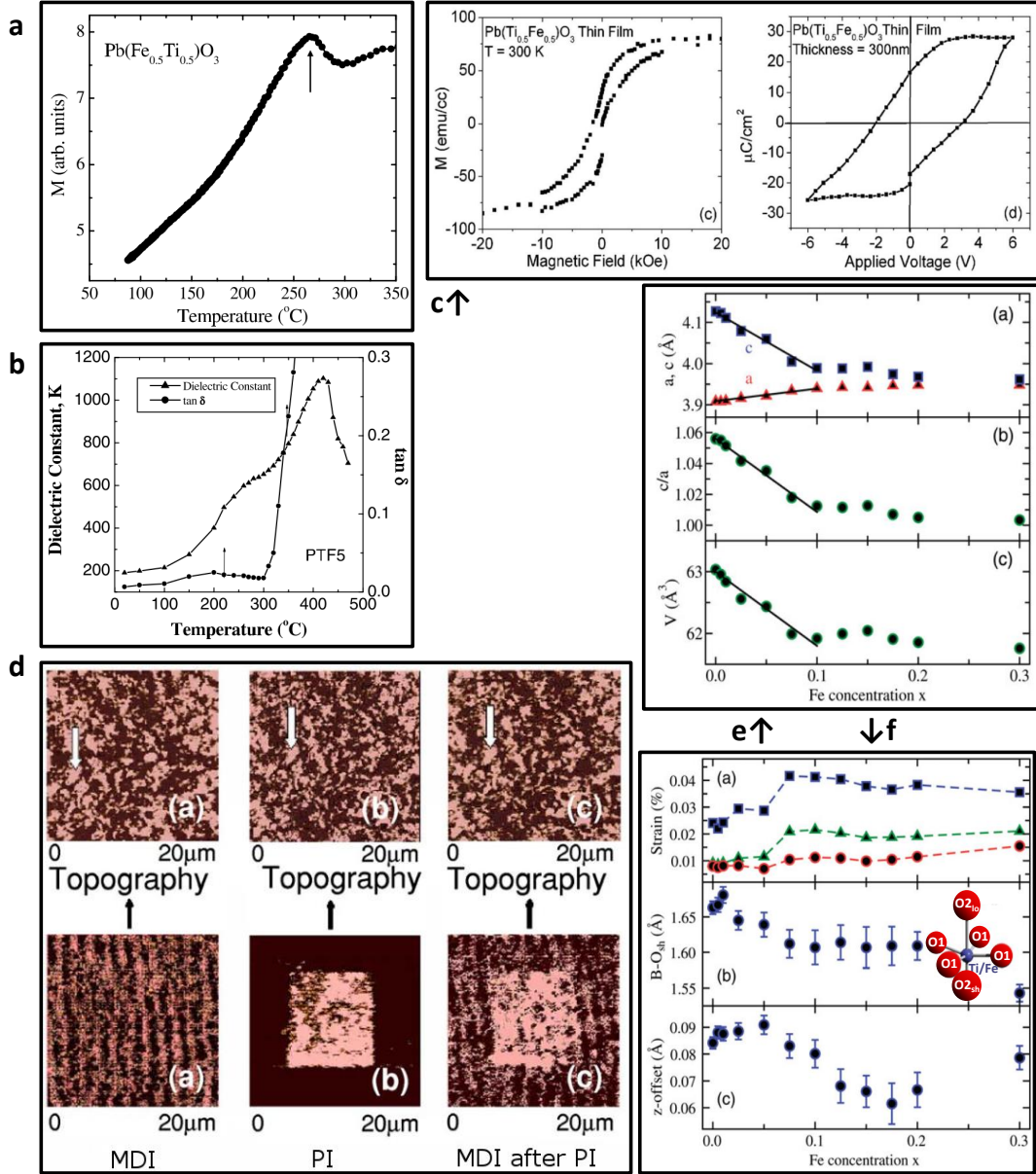


Figure 1.6: **PTFO Literature:** (a) AC magnetization vs. temperature for $\text{Pb}(\text{Fe}_{0.5}\text{-Ti}_{0.5})\text{O}_3$ (magnetic field of 1.1 Oe at 245 Hz) [71]. (b) Dielectric constant and $\tan(\delta)$ vs. temperature for $\text{Pb}(\text{Fe}_{0.5}\text{-Ti}_{0.5})\text{O}_3$ pellet sintered at $1000^\circ\text{C}/2\text{ h}$. Measurements were done at 1 MHz [71]. (c) M-H isotherm (SQUID magnetometer) and (d) P-E loop using Pt as top and bottom electrodes obtained for $\text{PbTi}_{0.5}\text{Fe}_{0.5}\text{O}_{3-\delta}$ thin film ($\sim 3000\text{\AA}$) [27]. (d) $\text{PbTi}_{0.5}\text{Fe}_{0.5}\text{O}_{3-\delta}$ thin film. [Bottom Row] (a) MFM magnetic domain image. (b) PFM piezoresponse image with written domains. (c) MFM domain imaging after writing ferroelectric domains. [Top Row] Topography [27]. (e) Cell parameters obtained from PTFO XRD data at room temperature as a function of Fe concentration. (a) Unit-cell parameters a and c , (b) tetragonal distortion c/a , and (c) cell volume [68]. (f) As a function of Fe concentration: (a) the variation of strain in the (001) (triangles), (hk0) (squares), and (111) (circles) planes; (b) the shortest B-O bond length (B-O_{2sh}); (c) the offset in the z-direction between the B-site cation and oxygens in a, b faces ($|\text{B}(z)\text{-O1}(z)|$) [68]. [All Figures and Captions re-produced from literature as indicated by citation]

1.3.2 $\text{PbTi}_{1-x}\text{Fe}_x\text{O}_3$

The ionic radius of Fe^{3+} is 0.58 Å, which is similar to that of Ti on the B-site, which means that Fe^{3+} is preferentially substituted at the B-site [70]. When a Ti^{4+} is replaced by Fe^{3+} , charge compensation necessitates formation of oxygen vacancies. Density functional theory (DFT) calculations [66] using a $2 \times 2 \times 2$ PbTiO_3 supercell have shown that the formation of oxygen vacancies along the c-direction (removing O1 or O1') is energetically more favourable than other directions. Furthermore, the cation nearest to the vacant site moves away from the vacancy, shortening the metal-oxygen bond distance.

$\text{PbTi}_{1-x}\text{Fe}_x\text{O}_3$ (PTFO) has been reported to be multiferroic at room temperature [71], with the partial substitution of Fe on the B-site allowing magnetism to be induced. Hysteresis was observed for both the magnetisation and polarisation with applied magnetic and electric fields respectively. Coupling between the orders was also demonstrated with the saturation polarisation increasing when subjected to a 2 T magnetic field. A broad peak in the dielectric function was observed around 260°C, while in high temperature susceptibility measurements a peak in the magnetisation was seen at $\sim 270^\circ\text{C}$ (See Figures 1.6(b) and (a) respectively). As Landau-Devonshire theory [72] predicts a dielectric anomaly near a magnetic transition the mode observed in the susceptibility measurement was attributed to a magnetic phase transition. A peak at 420° was also observed in dielectric response, which was attributed to the ferroelectric transition [71].

Increasing the level of Fe substitution has been seen to enhance the magnetisation [73, 74]. As with other multiferroics the switch to thin films [27] and nanoparticle [73, 75, 76, 77] geometries is thought to potentially enhance ferroelectricity and ferromagnetism in comparison to the bulk phase. Figure 1.6(c) shows a M-H and a P-E loop for thin film PTFO. The saturation magnetisation and polarisation here are $M_s=74\text{emu}\text{cm}^{-3}$ and $P_s=30\mu\text{C}\text{cm}^{-2}$ at $200\text{kV}\text{cm}^{-2}$ [27] while bulk samples had

reported values of the order of $M_s \sim 0.5\mu_B/\text{fu}$ and $P_s \sim 10\mu\text{Ccm}^{-2}$ at 200kVcm^{-2} [71]. Increased Dy levels lead to reduced particle size and increased saturation magnetisation [73]. Negligible leakage current and unsaturated ferroelectric hysteresis loops have been reported for PTFO thin films [78]. Evidence of magneto-electric coupling in PTFO has been observed with electrically written domains visible in magnetic force microscopy images (See Figure 1.6(d)) [27]. The top row shows the topology only, while the bottom row shows: (a) The ferromagnetic domains using MFM before any polling. (b) Ferroelectric domains written by polling the sample. The piezoresponse remains polling voltages were switched off, and thus show the existence of remnant polarization. (c) MFM domain image taken after the writing of the ferroelectric domains. This image gives information of both ferromagnetic and ferroelectric domain structures and is a composite of the two previous images. The clear presence of the electrically written domains the purely magnetic measurements demonstrates the coupling between the ferroelectric and ferromagnetic orders.

Although the substitution of Fe on the B site allows magnetism to be induced, at low concentrations this also causes a reduction in the tetragonal distortion c/a [73, 75, 79] (studies go up to a maximum of 4%). As this distortion is associated with the magnitude of the remnant polarization this would be expected to decrease with reduced c/a , although this has not been observed directly. At higher concentrations there have been some differing reports. A detailed X-ray study of the effect of Fe concentration over the full range $0 \leq x \leq 1$ [68] showed a rapid decrease of (001)-(100) tetragonal splitting up to $x = 0.1$, after which splitting was no longer visible (see Figure 1.6)(e). Samples with Fe concentration $x \leq 0.3$ were observed to be free from impurity phases, while above this minor reflections from the ferromagnetic magnetoplumbite phase, $\text{PbFe}_{12}\text{O}_{19}$ were observed. The authors proposed that the formation of this phase is what could be responsible for the room-temperature ferromagnetism reported by other authors [27, 71, 73, 75, 78]. The disappearance of

the tetragonal distortion with higher concentrations of Fe substitution reported by Ganegoda *et al.* [68] is in contrast to the work of Palkar and Malik [71] and Schofield *et al.* [80]. Palkar and Malik saw clear evidence of (001)-(100) tetragonal splitting in $\text{PbTi}_{0.5}\text{Fe}_{0.5}\text{O}_{(3-\delta)}$, which gives a tetragonal distortion of 1.028 allowing the existence of magneto-electric properties in a sample [71]. Ganegoda *et al.* [68] suggest that the splitting of diffraction peaks at $x=0.5$ in Palkar and Malik [71] could be the result of phase segregation where a Ti-rich phase remains tetragonally distorted. They suggest that this could arise as these samples were prepared at 1000°C [71] which is 300°C higher than their own processing temperature [68]. They also observe that the strain in the c -direction is distinctly higher as a result of inhomogeneity in tetragonality, and suggested additional contributions from oxygen vacancies formed in the $(hk0)$ planes (see Figure 1.6(e)). Formation of oxygen vacancies at O_{2i_o} sites and the lowering of B-O_{2sh} bond length with Fe doping is consistent with theoretical predictions of Meštrić *et al.* [66] and EPR results [81, 82, 83]. Distorted oxygen octahedra with off-centre shifted B-site cation imply the continued existence of displacive type ferroelectric properties. Defect dipole formation may contribute to enhanced ferroelectric properties [68]. This could account for the observed ferroelectric properties despite the reduction in c/a with increased substitution. In contrast X-ray and TEM measurement in the range $0 \leq x \leq 0.5$ on nanopowders have also reported that c/a decreased up until $x=0.3$ but showed a slight increase for $x > 0.3$ [80].

The differing properties as a result of strain, processing temperature, geometry and composition suggest the need for multiple to probe the (micro)structure and properties of each sample. This is the approach that is followed in Chapter 4

1.4 Optical Techniques Applied to Multiferroics

In addition to their response to static stimuli, dynamic magnetoelectric coupling under alternating fields is of great interest [84] because Maxwell's equations permit a

linear magnetoelectric coupling if the electric and magnetic fields vary temporally and spatially [85]. To couple to different underlying mechanisms a range of techniques spanning the electromagnetic spectrum are required. Figure 1.7 outlines a spectrum for the dielectric permittivity over a wide spectral range, highlighting various processes that occur at different energies. Some processes which are of particular relevance in multiferroics, namely electromagnons, phonons, ferromagnetic (FM) and antiferromagnetic (AFM) magnons, are also highlighted [86]. Recent demonstrations of novel dynamic magnetoelectric effects include the electric field control of Raman-active spin modes [87], the time-resolved reflectivity of magnons in a hexaferrite [88] and the discovery of electric dipole-active spin waves (electromagnons) [89, 90, 91]. This section will examine some recent literature where similar optical techniques to those used in this work (see Methods, Chapter 2) have been used to examine properties of multiferroics. This section is divided up in terms of technique as follows: 1.4.2 Transient Reflectivity; 1.4.3 Ellipsometry; 1.4.4 ,Second Harmonic Generation; 1.4.5 Thz Time-Domain Spectroscopy; 1.4.6 Raman and FTIR.

1.4.1 Excitations

Phonons

Phonons are vibrations of the atoms making up a crystal lattice. In solids, the atoms that make up the material are bound to equilibrium lattice positions. When they are displaced from these they experience restoring forces which cause them to vibrate at characteristic frequencies [92]. The resulting dispersion relation leads to two branches; acoustic, at lower frequencies with in-phase (coherent) movement of adjacent atoms in the lattice and optic, at higher frequencies with out-of-phase movement of adjacent atoms in the lattice [93]. Phonons can be longitudinal or transverse depending on whether the atoms are displaced in the same direction or perpendicularly to the mode's propagation direction. Thus there are 4 distinct types of phonon; transverse acoustic, transverse optic, longitudinal acoustic and longitudinal optic (TA, LA,

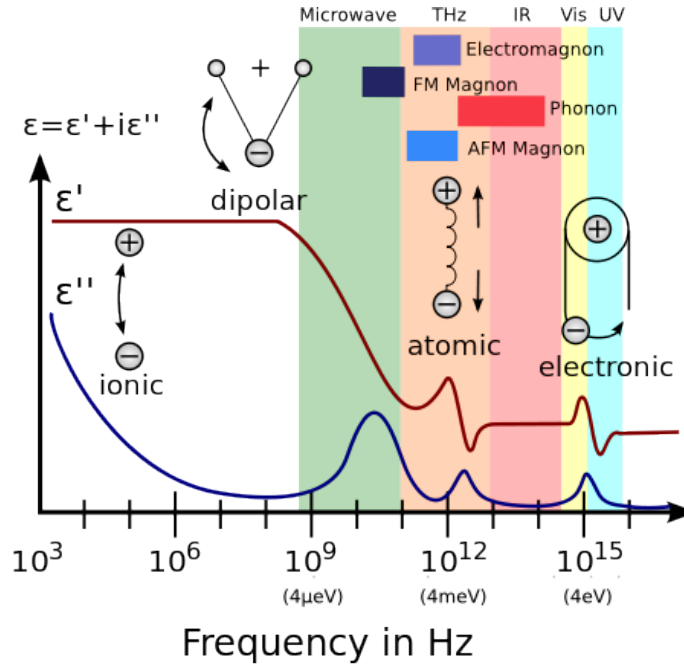


Figure 1.7: A dielectric permittivity spectrum over a wide range of frequencies. ϵ' and ϵ'' denote the real and the imaginary part of the permittivity, respectively. Various processes are labelled on the image: ionic and dipolar relaxation, and atomic and electronic resonances at higher energies. The energy range over which some phenomena which are of particular relevance in multiferroics can be observed spectroscopically are also highlighted [86]. These are; electromagnons (purple), phonons (red), ferromagnetic (FM) and antiferromagnetic (AFM) magnons (dark and light blue respectively). *[Figure modified from Wikipedia]*

TO, LO). Different optical techniques can couple to different types of phonon. Optical techniques such as FTIR and Raman will couple to the higher energy optical phonons [92], while transient reflectivity can couple to acoustic phonons.

Magnons

Perturbing a crystal lattice produces a lattice wave or phonon mode. In ferromagnets (and antiferromagnets) magnons are analogous to phonon modes but where the spin states rather than lattice positions are perturbed. Magnons are hence also frequently referred to as spin waves [94].

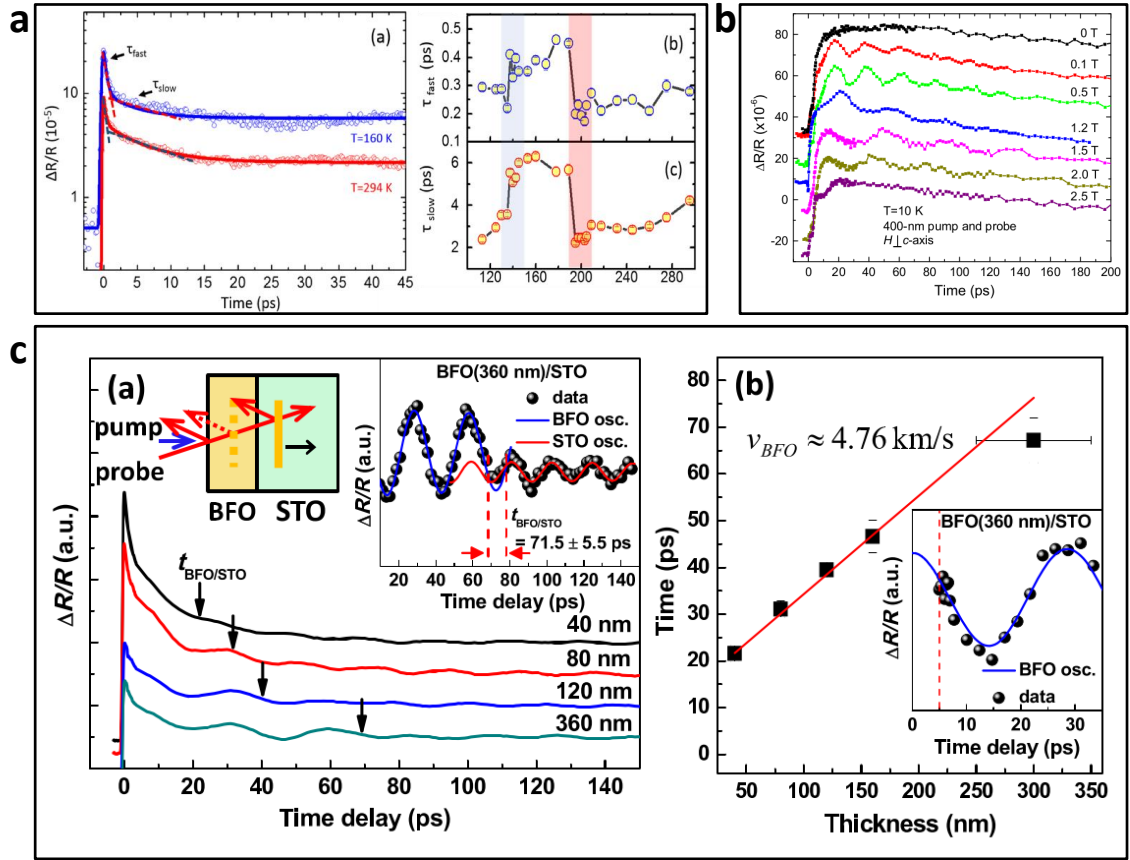


Figure 1.8: **Transient Reflectivity:** (a) (a) Logarithmic plot of optical reflectivity change as a function of time delay at two temperatures, 294 K and 160 K, at photoexcited energy of 3.1 eV and probed at 1.55 eV in a BFO film on STO substrate. (b) and (c) The temperature-dependent fast and slow time constants, τ_{fast} and τ_{slow} , respectively [95]. (b) (a) The $\Delta R/R$ on (110) BFO thin films with various thicknesses. The arrows indicate the BFO/STO interface. Left inset: schematic illustration of the propagation of strain pulse inside BFO and STO substrate. Right inset: the oscillation signal was obtained by subtracted the decay background from $\Delta R/R$ of (a). Solid lines are the sinusoidal fitting. (b) The thickness-dependent strain pulse propagating time ($t_{BFO/STO}$) through the interface between BFO and STO. Solid line is the linear fitting curve. Inset shows a part of the right inset in (a) on an enlarged scale [96]. (c) Pump-probe reflectance of BSZFO in the magnetic field. The spectra are shifted along the vertical axis for clarity [88]. [All Figures and Captions re-produced from literature as indicated by citation]

1.4.2 Transient Reflectivity

Transient reflectivity (optical pump-probe) measurements can couple to a wide range of phenomena that allow the physical mechanisms in multiferroics to be studied. A few such studies are outlined here. When multiferroics are photoexcited a charge transfer process occurs, for instance in BFO this occurs between $O_{2p} \rightarrow Fe_{3d}$ states [97]. This leads to a rapid rise in reflectivity after excitation and subsequent decay which is observed by optical pump-probe experiments. Rapid rise and a non-exponential decay have been reported in recent studies of bulk BFO [98, 99] and thin films grown on a variety of substrates [100, 100, 101, 102]. Aspects of these features can be used to understand a variety of processes in multiferroics. Decay lifetimes have been used to examine the structural differences of BFO films on different substrates [100]. The electronic response for 150 nm BFO films on ZrO_2 (YSZ) and $SrTiO_3$ (STO) which respectively give tetragonal and rhombohedral films were used to show that the electron-phonon interaction bigger for T- than R- because of structural strain and symmetry breaking. Anomalies in decay lifetimes at particular temperatures (as those shown in Figure 1.8(a)) have also been identified to coincide with changes in the magnetic ordering [95]. Temperature anomalies at 137.5 K and 195 K which align with the previously reported hidden phase transition, where an anomaly in Raman studies at 140 K (discussed later) have been assigned as a spin reorientation transition [87, 103].

Phonons: Optical reflectivity is a sensitive tool for coupling to coherent acoustic phonons. Coupling to phonons can come about through a number of mechanisms, which are thoroughly discussed in a review by Ruello and Gusev [104]. Coupling mechanisms include: (i) the deformation potential, where a modification of the electronic energy distribution causes strain in the material. This comes about because the interatomic forces are dependent on the electronic distribution; thus when modi-

fied the equilibrium position of the lattice is modified, causing the crystal to deform. (ii) Thermoelasticity, where a change in temperature induces a change in the material's elasticity i.e a volume change. (iii) Inverse piezoelectricity, where there is coupling between strain and internal electrical field in the material. This arises in non-centrosymmetric materials from the macroscopic polarisation that comes about as a result of separation of the of positive and negative charges when induced by lattice stain. (iv) Electrostriction, where the local electric field of the pump light causes the material to be polarised, inducing a deformation of the electric orbitals [104].

Phonon modes have been studied in a wide variety of multiferroic systems. Due to crystal symmetry both LA and TA phonons have been observed in bulk BFO. This allows experimental evaluation of the elastic coefficients, which had previously only been estimated through *ab initio* calculations [99]. Transient reflectivity has also been used to look at thin films of BFO. As with earlier studies on semiconductor layers on substrates [105] for multiferroic thin films the time after excitation will determine whether a phonon mode is in the film or has propagated into the substrate. An example of this can be seen in Figure 1.8(b) for BFO films on STO [96]. When strain pulses propagate through the BFO/STO interface, both the amplitude and period of the $\Delta R/R$ oscillation decrease. The time at which this occurs can clearly be seen to increase with increasing film thickness. This work also suggests photostriction derived from the optical rectification effect as the phonon mechanism. This conclusion was based on a combination of observations: (i) that the oscillation signal starts within ps after excitation (see inset of Figure 1.8(b)-b). (ii) That although, with sample rotation angle in the plane of the sample, they observed no change in the magnitude of $\Delta R/R$ at $t=0$ (indicating that the photo induced excitation is isotropic in BFO films) there was a strong dependence of the oscillation amplitude of $\Delta R/R$ on ϕ . and (iii) the observation of a two-fold symmetry of oscillation amplitude with pump polarisation. Another example of work on transient reflectivity examines the effect

of the substrate on phonon modes in co-doped BFO ($\text{Bi}_{1-x}\text{La}_x$)($\text{Fe}_{1-y}\text{Nb}_y\text{O}_3$, $x=0.2$ and $y=0.01$). This is used to give the insight on the dynamical coupling between electrical polarization and lattice deformation.

Temperature Dependence: Coherent acoustic phonons have been observed in multiferroic LuMnO_3 [106, 107] and YMnO_3 [108] in temperature dependent optical pump-probe studies. The periodicity of the observed oscillatory feature was dependent on the wavelength and the angle of incidence of the probe, while the frequency, dephasing time and phase of the oscillation were found to be temperature dependent [106] and to be consistent with a propagation strain pulse model [109]. Large phase shifts have been observed at T_N with differing oscillation periods above and below. Coherent oscillation of the acoustic modes has been observed above T_N with the phonon weakening as the temperature decreases towards T_N . These observations have been attributed to an electric-dipole allowed d-d transition that is coupled to short-range antiferromagnetic spin fluctuations. This reveals that coherent acoustic phonons are strongly coupled to spins, allowing the origin of the acoustic phonon generation to be attributed to magnetic ordering [106, 107, 108]. This is supported by thermal analysis showing that the acoustic phonon can be strongly coupled to spin fluctuations above and below T_N [110]. The measured reflectivity oscillation is also sensitive to change in the group symmetry. The combined effects of the geometrically frustrated triangular Mn arrangement and the strong two-dimensionality of the magnetic ordering results in a reduction of the ordered magnetic moment [111]. Thus the observed changes in the phonon mode near T_N can be related to the large magneto-elastic coupling [112].

Symmetry Considerations: Attention has been given to the symmetry considerations of the optical phonon mode in LuMnO_3 [113]. The reflectivity from the *ab*- and *ac*-planes was examined with the pump and probe polarised both parallel and per-

pendicularly with respect to each other. Analysis of the oscillation feature from these faces revealed modes at 3.54 THz and 3.61 THz, which were identified as transverse (TO) and longitudinal (LO) respectively. Applying an exponentially decaying cosine fit to the observed reflectivity oscillation revealed that LO and TO modes have a phase shift of π with respect to each other indicating a displacive mechanism. Considering the Raman tensor components in light of the crystal orientation and the phase of the reflectance oscillation the mode was determined to have totally symmetric, A_1 symmetry [113].

Magnons: Magnon modes in multiferroics have also been coupled to with optical pump probe studies. A magnetic field dependant study using optical pump-probe reflection spectroscopy has been used to observe a magnetic resonance mode in large magnetoelectric response multiferroic $\text{Ba}_{0.6}\text{Sr}_{1.4}\text{Zn}_2\text{Fe}_{12}\text{O}_{22}$ (BSZFO) [88] (see Figure 1.8(c)). The period of an oscillatory feature in the reflectance spectrum was seen to increase with increasing magnetic field but remained the same under electrical polling. It was also observed that the oscillation frequency decreased as the Néel temperature was approached. Furthermore the frequency of the oscillation was sufficiently low as to exclude the possibility of it having arisen from coherent optical phonons and the absence of a λ dependence on the reflectance oscillation excluded coherent acoustic phonons, which should exhibit a n/λ dependence [109], where n is the refractive index of the material. The strong dependence of the oscillation frequency on the magnetic field strength together with the temperature and λ dependencies indicates that the nature of the oscillatory feature is magnetic in origin and that coherent magnons are responsible for giving rise to the observed features [88].

1.4.3 Ellipsometry

Ellipsometry allows the complex refractive index and thickness of thin films to be measured. The oscillator modes that give rise to the complex refractive index can

be used to give insight into structural and charge transfer processes. Ellipsometry measurements in BiFeO₃ thin films have shown that an increased tetragonal distortion leads to a blue-shifting of the complex dielectric function [114] (see Figure 1.9(a)). In BFO an octahedral crystal field will cause a splitting of the 3*d* orbital into *t*_{2*g*} and *e*_{*g*} levels. The presence of strain from the substrate will then modify the local structure. This modification will further split the *t*_{2*g*} into *d*_{*xy*} and degenerate *d*_{*xz*} and *d*_{*yz*} and the *e*_{*g*} into a lower energy *d*_{*z*²} and a higher *d*_{*x*²-*y*²} level. This is known as the Jahn-Teller effect, see Figure 1.9(b). Differences in the resulting energy levels will be reasonable for the shift in the complex refractive index.

1.4.4 SHG

Nonlinear optical processes are a useful tool for the investigation of magnetic and structural properties of materials; χ^2 processes such as SHG are the lowest order of these processes. The technique has many advantages and applications. As SHG can only be generated in non-centrosymmetric materials this makes it a useful probe of whether materials are polar. It is however also possible to get SHG from surface and interface states in centrosymmetric materials, because of the breaking of inversion symmetry at the boundary. A thickness dependent characterisation can be used to rule out this effect. Additional contributions to the SHG through the breaking of time-inversion symmetry can be made by spontaneous long-range magnetic order and/or the application of external magnetic fields. Using SHG it is possible to discriminate between different space groups based on the symmetry of the SHG polarisation; this is achieved by comparing the spectra obtained for different SHG components by changing the orientation of the sample. The spatial resolution that is offered by SHG has made it a useful tool for imaging of domain structures and examining the microstructure of multiferroics [116].

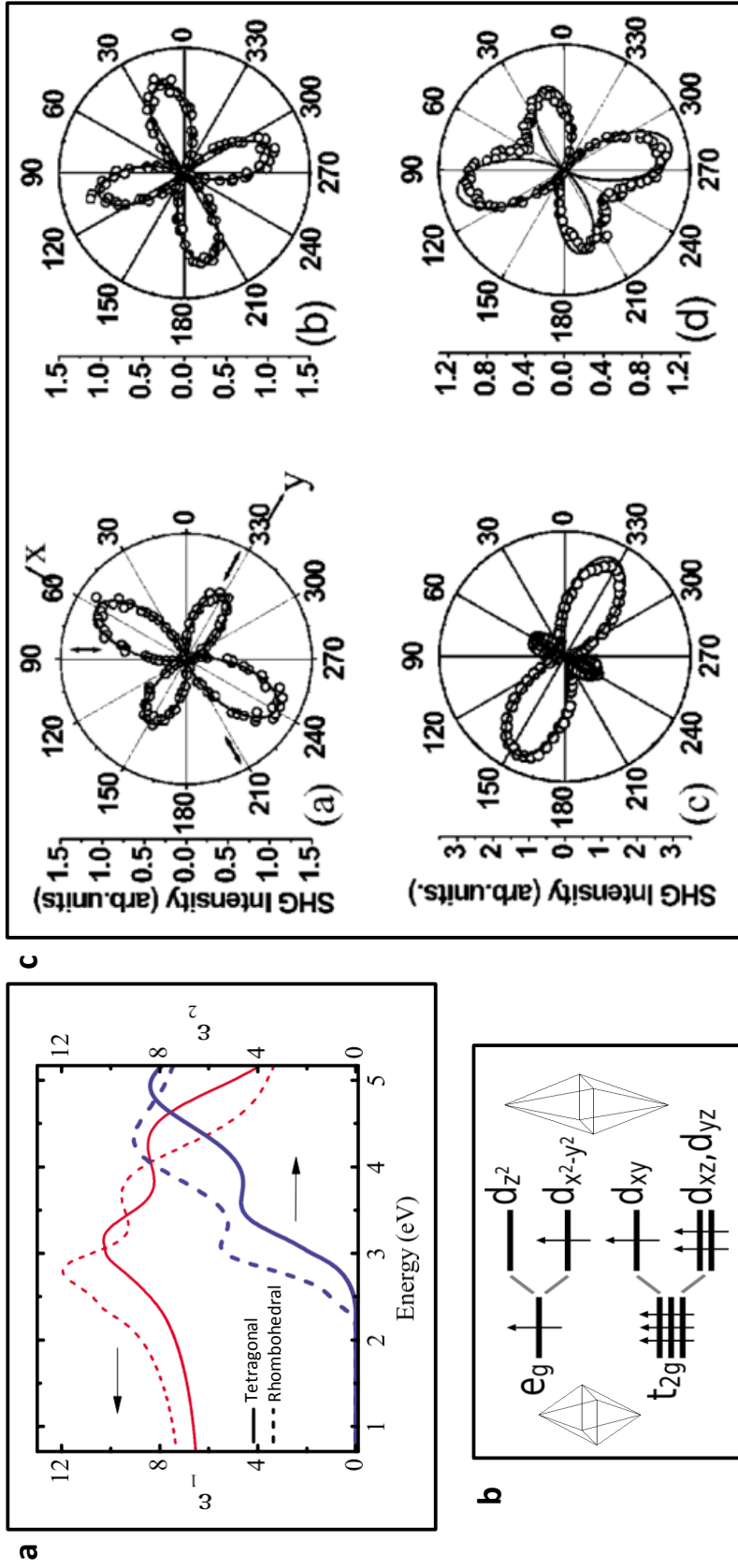


Figure 1.9: (a) **Ellipsometry**: Complex dielectric function for tetragonal [114] (solid line) and rhombohedral [115] (dashed line) BiFeO_3 [114]. (b) Jahn-Teller effect [94, 97]. (c) **SHG**: Polar plots (82K) of the SHG intensity polarized along $\text{SrTiO}_3[10\bar{1}]$ [x axis; I_y (b) and (d)] or $[12\bar{1}]$ [y axis, I_y (a) and (c)] as function of the input polarization direction of the fundamental beam at an angle θ to the x axis. (a)-(b) before application of any voltage. (c)-(d) after application and removal of $V=-2$ kV. Solid lines: theoretical fits. Arrows in (a) indicate the projection of possible ferroelectric polarization directions P_s plots [9]. [All Figures and Captions re-produced from literature as indicated by citation]

Domain Imaging

Spatially resolved SHG can be used to image the domain structure of multiferroics. The underlying principle that makes this possible is that adjacent domains with oppositely orientated order parameter (for example the spontaneous polarisation, P_S for ferroelectric order, or the antiferromagnetic ordering vector, for antiferromagnetic domain structures) will have a 180° phase shift with respect to each other. This causes the domains of opposite ordering to appear bright or dark with respect to the other [116, 117].

The nature of the domain structure in the ferroelectric and antiferromagnetic phases of YMnO_3 has been investigated in this way [116]. The ferroelectric domain structure was imaged by interference of the SHG signal were studied, however no relationship between the degree of anisotropy and the growth technique was found. From this it was concluded that the preference of a specific crystal orientation must depend on a factor that uniformly affects the whole crystal.

Multiferroic Order

SHG can also provide evidence for different ordered phases in materials. Ferroelectricity was observed in BiMnPO_3 epitaxial films on SrTiO_3 substrates using SHG [9]. It was seen that changes in the polar symmetry of the SHG signal under external electric fields was correlated to the changes in the ferroelectric domain microstructures. Changes in the magnitude and symmetry of the second harmonic response with an applied external field can provide a unique signature that indicates the presence of ferroelectric domains. Considering the SHG components it was suggested that for electric-field-induced microstructural bias, the terms A_y^2 and B_y^2 of the second harmonic intensity patterns given by $I_j / (A_j \cos^2 \theta + B_j \sin^2 \theta + C_j \sin^2 \theta)^2$ would dominate I_y , and terms C_x^2 would dominate I_x . This can be seen from Figure 1.9(c) where $\sin^2(2\theta)$ (associated with C_x^2) dominates the intensity patterns $I\theta$. Similarly, $\sin 2\theta$ and $\cos 2\theta$

terms (associated with A_y^2 and B_y^2) dominate the SHG signal I_y in Figure 1.9(c). Change induced by the electric field can be observed when going from $I_y(0^\circ)$ (Figure 1.9(c)-a) to $I_y(90^\circ)$ (Figure 1.9(c)-c). Similarly, it can be seen that change in applied field between Figures 1.9(c)-b and d produced a change in intensity. These modifications can be related to the coefficients of the second harmonic intensity and thus the changes in the SHG signal with external field can be seen to be consistent with the presence of ferroelectric domains in BiMnO_3 films under these conditions. SHG has been used to report a new unique form of multiferroism in SrTiO_3 which is induced by applying biaxial strain [118]. A transition from the $4/mmm$ to the ferroelectric $mm3$ followed by a transition to a ferroelastic-ferroelectric $mm3$ phase has been reported in the thin-film. This is a ferroelectric-antiferrodistortive form of multiferroism. SHG was used to study the domain structure and phase transitions. The ferroelectric domains have been directly imaged at room temperature for the first time. SHG was also used to understand the mechanism for coupled ferroelastic-ferroelectric domain wall motion.

1.4.5 THz

Observing Electromagnons

GdMnO_3 and TbMnO_3 , along with other multiferroic manganites, possess a strong magneto-electric coupling. As a consequence of this an electrically-active spin state, an electromagnon, was first shown to exist in GdMnO_3 and TbMnO_3 [119]. Electromagnons can be identifiable as magnons that are excited by an a.c. electric field.

The dielectric function obtained by THz spectroscopy for GdMnO_3 and TbMnO_3 can be seen in Figure 1.10(a). The measurements made without magnetic field (open symbols) with $E \parallel a$ show a broad absorption feature at $\nu_0 = 23 \pm 3 \text{cm}^{-1}$ and $\nu_0 = 20 \pm 3 \text{cm}^{-1}$ for GdMnO_3 and TbMnO_3 respectively. This dielectric contribution increases with decreasing temperature and saturates in the low temperature magnetic phase. The connection between the observed excitation and the magnetic subsystem

were investigated by applying a static magnetic field along the c axis (closed symbols). It can be seen that the excitation is suppressed for both the real and imaginary components, which reflects the mutual connection between both properties and identifies the excitation as a magnon.

The inset in Figure 1.10(a)-b demonstrates that the spinmode is excited by the a.c. electric field despite the clear connection of the mode to the modulated magnetic structure. It can be seen that the magnetic excitation is suppressed when the a.c. component is rotated from $E||a$ to $E||b$ while leaving the magnetic field unchanged. In contrast the excitation remains unchanged when the a.c. magnetic field is rotated from $H||c$ to $H||b$. This demonstrated that there is a strong coupling between the magnetic and lattice degrees of freedom. Thus it was shown that a new hybrid spin-lattice excitation that can be excited by an a.c. electric field, i.e. an electromagnon exists in magneto-electric multiferroics. When this excitation appears it is accompanied by a significant refractive index change, which has interesting implications for the design of magneto-optic devices [119].

1.4.6 Raman Spectroscopy

Raman spectroscopy can be used as a structural characterisation tool. For example, X-ray and Raman data have together suggested that the BiFeO_3 structure is tetragonal for 70 nm thick films and changes to monoclinic for 240 nm thick films, which remains different from that of the bulk (rhombohedral) structure [120]. Polarized and unpolarized Raman spectra were used in order to better determine the symmetry changes of BFO films observed by XRD. Differences between the thin film Raman spectra and those for bulk confirm the difference in their structures.

Magnetic ordering has also been studied with Raman spectroscopy. Low energy spin excitations in BFO have been observed and attributed to two species of magnon corresponding to spin wave excitations in the cycloid plane [87]. Although no optical phonons are expected in BFO below 50 cm^{-1} [121, 122], a series of Raman modes have

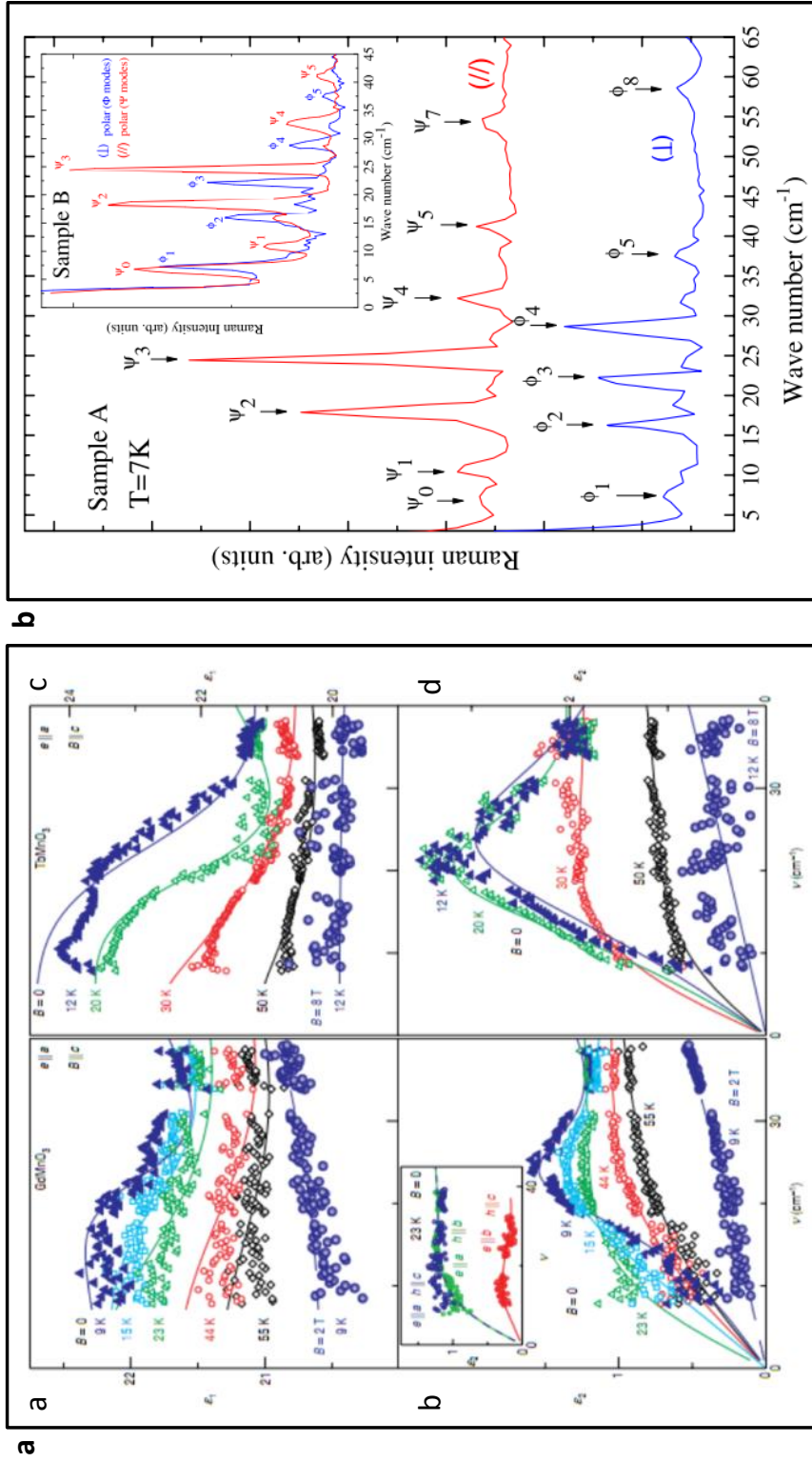


Figure 1.10: (a) **THz**: Electromagnons in GdMnO₃ and TbMnO₃. Frequency dependence of the real (a,c) and imaginary (b,d) parts of the THz-dielectric function in GdMnO₃ (a,b) and TbMnO₃ (c,d) with E||a and B||c. The inset in (b) demonstrates unique (E||a, H-independent) excitation conditions for electromagnons [119]. (b) **Raman**: Raman spectra of spin excitations in BiFeO₃ in two sample (A & B). The equally and non-equally spaced modes at low frequencies correspond, respectively, to ψ and ϕ cycloidal modes selected using parallel (||) and crossed (⊥) polarizations. The ψ series is shifted to higher energy in comparison with the ϕ . ψ_0 and ϕ_1 mode energies are distinct [87]. [All Figures and Captions re-produced from literature as indicated by citation]

been observed at low numberer [87, 123]. These can be seen in Figure 1.10(b) where twelve peaks, in two distinct polarisation dependent sets, have been detected with first mode at $7.4 \pm 0.5 \text{cm}^{-1}$ [87]. The chosen polarisations were in the (010) plane and were parallel (\parallel) and crossed (\perp) with respect to the spin cycloid's propagation wave vector, q , which is along the $[10\bar{1}]$ (as in Figure 1.2(b); the cycloid plane, where spin riation occurs is $(\bar{1}2\bar{1})$). With this it was seen that the ψ modes were equally spaced, while the ϕ where not. These observations were found to be in agreement with a theoretical approach based on the effective Ginzburg-Landau free energy [124], which predicts two species of spin excitations lying in and out of the cycloid plane at small wave vectors. The theory predicts that one of the the cycloids will have a gap due to pinning of the cycloid plane by the electrical polarisation, while the other will have none. This is what is observed experimentally when the mode index is plotted against wave number. The presence of the gap energy indicates that there is coupling between cycloidal magnetic order and electrical polarisation. These findings are in agreement with neutron scattering measurements showing a cycloidal orientation change under an applied electric field [24]. There has been some suggestion that modes are not purely magnetic but have some dipole active character given that the mode intensity does not decrease with index and there is a maximum corresponding to a dipole active mode detected by IR measurements [125]. Electric-field control of the spin waves has also been observed. With applied field the ψ_n modes have been seen to blueshift, while the ϕ_n modes redshift [90].

Chapter 2

Experimental Methods & Theoretical Background

This work investigates the optical and vibrational properties of multiferroic oxide thin films. Both time-resolved and continuous-wave techniques have been used to investigate the optical properties. The time resolved technique used is **Optical Pump Probe Reflectivity (Transient Reflectivity)**. In this technique the sample is excited with an ultra-short laser pulse and the time evolution of the response was measured by a delayed probe. The continuous-wave techniques used to measure the linear optical properties were **Spectroscopic Ellipsometry**, which determines the complex refractive index and thin film thickness, and **Second Harmonic Generation**, which was used to characterise the non-linear optical response. A number of techniques were used to examine the vibrational properties. These include **Terahertz Time-Domain Spectroscopy**, **Fourier Transform Infrared Spectroscopy** and **Raman Spectroscopy**.

Transient Techniques

2.1 Optical Pump Probe Reflectivity

Transient reflectivity works by measuring a pump induced change in a sample's reflectance of a probe beam, arising from induced changes to the complex refractive

index of the sample. The technique can provide a sensitive probe of the microscopic dynamics and coupling between degrees of freedom in complex materials. The technique is suited to the study of multiferroics as it allows both the phonon and magnon responses to be examined in the time domain by recording changes in the reflectance[88]. Pump-probe spectroscopy employing above-band-gap laser pulses can help to ascertain the structural dynamics that arise upon the excitation of localized states. Time-dependent analysis of generated coherent phonons can be used to study the coupling-dynamics of spins and the lattice[107]. The use of the reflection geometry is particularly desirable for the study of multiferroic materials as many of the materials of interest will be opaque at one or both of the pump/probe wavelengths. After discussing the experimental setup in Section 2.1.1, different mechanisms that alter the reflectivity are described in Section 2.1.2.

2.1.1 Experimental Setup

A schematic of the experimental setup used for pump-probe reflectivity measurements can be seen in Figure 2.1. A mode-locked Ti:sapphire laser oscillator (4 MHz, 650 nJ, 50 fs) was used for these experiments. The laser system uses a semiconductor laser to pump a Nd:YAG laser. This is frequency doubled to 532 nm (2.33 eV) and has an output power of 15 W. It is then used to pump the Ti:sapphire crystal of the oscillator which gives stimulated emission at $\lambda=800$ nm (1.55 eV). The system is mode-locked by a saturatable Bragg reflector, and the long cavity path length created by a multi-pass cell gives the 4 MHz repetition rate. This gives a pulse a broad spectra with a full width at half maximum (FWHM) of ~ 40 nm. Due to the positive dispersion regime in which the system operates the spectrum has steep sharp edges. This similarity to a rectangular spectrum means that the pulse envelope in the time-domain bares resemblance to a sinc-function. Only 3-6% of the energy should exist in the wings of the main pulse; this means that the central portion of the beam profile will be well approximated by a Gaussian wave form. Inside the cavity the pulse duration is ~ 1 ps;

a multi-pass prism is used to recompress the pulse to ~ 50 fs.

To perform transient reflectivity measurements the beam is split into two parts; 95% for the pump and 5% for the probe (as labelled in Figure 2.1). The required wavelength of the pump beam is set by the point at which the onset of electronic absorption occurs in the sample under consideration. For the samples studied in Chapters 3 and 4 a pump energy greater than the fundamental ($\lambda=800$ nm \equiv 1.55 eV) was necessary to exceed the bandgap. As such the pump was frequency doubled to $\lambda=400$ nm (3.1 eV). The frequency doubling section is highlighted in Figure 2.1 with a dashed box. The beam is focused near the non-linear crystal (*NLC*), here a BBO (Barium borate, BaB₂O₄), and subsequently re-collimated. Focusing the beam allows for the high electric field required to generate the second harmonic efficiently. The BBO's position with respect to the focus and its angle with respect to the incident beam as well as the dispersion compensation of the laser (i.e. pulse duration) were adjusted to optimise the SHG efficiency of the BBO. This resulted in a pump fluence of $60\mu\text{Jcm}^{-2}$ at $\lambda=400$ nm at the sample. The remnant of the fundamental is then filtered out with a dichroic mirror (*DCM*) and an absorptive filter.

The pump and probe beams are focused onto the surface of the sample. The probe is incident at close to the normal, so as to minimise the effect of angle on the modes probed. The spot sizes of the pump and probe are such that the diameter of the probe is much smaller than that of the pump ($\sigma \approx 0.2:0.02$ mm). The smaller spot size of the probe was achieved by first expanding the probe beam diameter, allowing it to be focused with a smaller waist. A smaller diameter for the probe is desirable as only the regions of the sample that have undergone excitation are of interest. Furthermore this means that the probe examines a region with a uniform excitation profile. The overlap of the pump and probe was adjusted to optimised the signal. A delay stage in the pump path was used to alter the arrival time of the pump with respect to the probe at the sample, allowing time resolved measurements to be made.

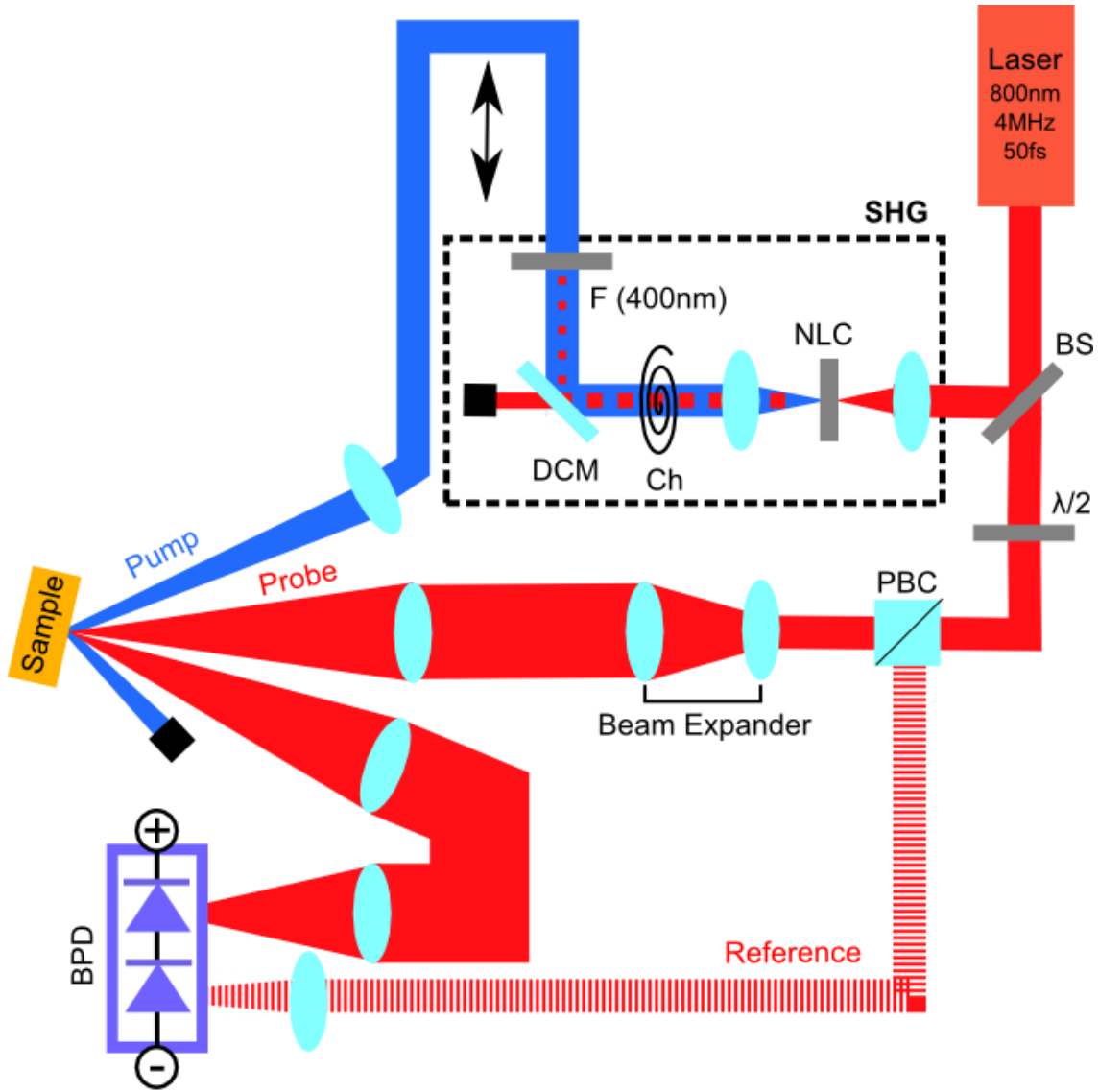


Figure 2.1: **Optical Pump Probe Reflectivity:** Schematic of experimental setup for the optical-pump reflectivity experiment. (*BS*) Beam splitter. (*L*) Lens. ($\lambda/2$) Half wave plate. (*PCB*) Polarising beam cube. (*NCL*) Non-linear crystal. (*Ch*) Chopper. (*DCM*) Dichroic mirror. (*F*) Filter. (\blacksquare) Beam dump. (\updownarrow) Delay stage. (*BPD*) Balanced photodiode detector. NB: Relative lengths of beam paths are not shown to scale.

The probe was also further divided into two parts; the probe itself (red solid), which was incident on the sample and a reference (red dashed), which was not. This allowed a balanced detection system to be used, which improves the signal to noise by filtering out laser noise. A mechanical chopper in the pump beam was used to modulate the pump power and the lock-in was referenced to its frequency. This means that the relative reflectivity of the sample is given by;

$$\frac{\Delta R}{R} = \frac{R_{Illum.} - R_{Dark}}{R_{Dark}} \quad (2.1)$$

where $R_{Illum.}$ and R_{Dark} are the amplitude of the reflected intensity from the sample under photoexcitation and in the dark respectively.

Asynchronous Optical Sampling (ASOPS)

Asynchronous Optical Sampling (ASOPS) can provide an alternative detection method for transient reflectivity experiments. Conventional time-resolved pump probe spectroscopy relies on the use of mechanical delay stages to introduce delay between the pump and probe pulses. In contrast, ASOPS uses two femtosecond lasers with detuned repetition rates (i.e. asynchronously linked) to do this. Using this approach the resolution of the time window that can be achieved is given by the ratio of the repetition rate detuning and the product of the repetition rate and the detection bandwidth. For repetition rates in 100 MHz-GHz and detuning frequencies in kHz range can give time windows of up to \sim ns which are much longer than can be achieved with conventional delay stages. The technique also has a number of other advantages compared to conventional pump-probe experiments; delay lines always a source of mechanical vibration, are limited in speed and may introduce changes in the spot size and position.[126]

Figure 2.2 shows a schematic diagram for the ASOPS experiment. The repetition rates of the pump and probe lasers are electronically synchronised (not shown). The

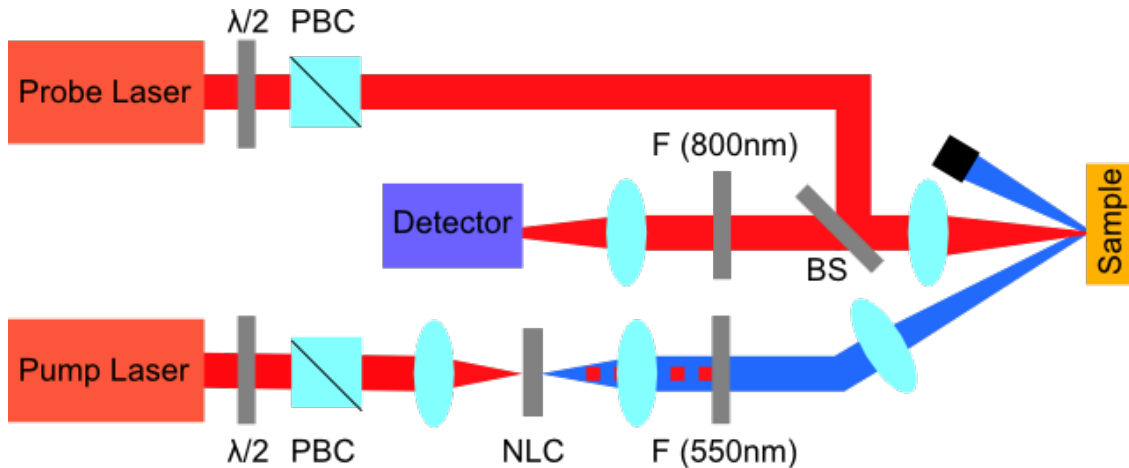


Figure 2.2: **ASOPS**: Schematic of experimental setup for the asynchronous optical sampling (ASOPS) experiment. (*BS*) Beam splitter. ($\lambda/2$) Half wave plate. (*PBC*) Polarising beam cube. (*NLC*) Non-linear crystal (BIBO). (*F*) Filter. (■) Beam dump.

pump beam is focussed onto a BIBO (BiB_3O_6) crystal to generate the second harmonic at $\lambda=400$ nm. This is then focused onto the sample. The probe is beam focused at normal incidence onto the sample and is overlapped with the pump beam. This geometry is achieved by using a beamsplitter. A filter is used to remove any scattered pump light from the probe beam, which is focused onto a photodiode detector.

2.1.2 Coupling Mechanisms

Electronic

For semiconductors, immediately after excitation with above band-gap radiation there will be a sharp change in the reflectivity. This is caused by the rapid transfer of electrons from the valence to conduction band [92]. In multiferroics the excitation process can be understood as a charge transfer process between initial and final energy states which are bound, rather than delocalised bands [97]. This causes a change in the refractive index of the sample altering the reflectivity, R , since at normal incidence;

$$R = \left| \frac{(\tilde{n} - 1)}{(\tilde{n} + 1)} \right|^2 \quad (2.2)$$

where $\tilde{n} = n + ik$ is the complex refractive index [92]. As such the photoinduced change ΔR will be proportional to the change in the complex refractive index, $\Delta R = \frac{dR}{d\tilde{n}} \Delta\tilde{n}$. Whether the sample becomes more or less reflective upon excitation indicates whether the electronic properties have become respectively more metallic-like or insulator-like with the transfer of electrons.

After excitation the system will begin to relax to its original state. In terms of the transient reflectivity response this will present as a decay back to the pre-excitation level. The characteristic lifetime of the decay will depend on the mechanism by which the relaxation is occurring.

Example: To test the pump-probe system measurements were initially carried out on previously well characterised semiconductors. Some of the results are presented here to illustrate the operation of the technique. Figure 2.3(a) presents the transient reflectivity for a 500 nm InAs film on a bulk GaAs substrate. Given the lower band gaps of InAs and GaAs than the multiferroic samples studied (0.354 eV for InAs and 1.424 eV at 300 K) this was pumped and probed at 800 nm (1.55 eV). As can be seen upon photo excitation there is a sharp rise, which is then followed by a slower decay.

Phonons

Transient reflectivity measurements can couple to acoustic phonon modes (also referred to as a strain pulse). A strain pulse is created by the perturbation of the lattice by photoexcitation, and propagates through the multiferroic film. Oscillations in the transient reflectivity arises from interference between a fraction of the probe pulse specularly reflected from the sample surface and a fraction reflected from the propagating strain pulse [109]. This mechanism can also be described as stimulated Brillouin scattering [127]. The strain pulse results in a characteristic frequency;

$$f = \frac{2nv}{\lambda} \cos \theta \quad (2.3)$$

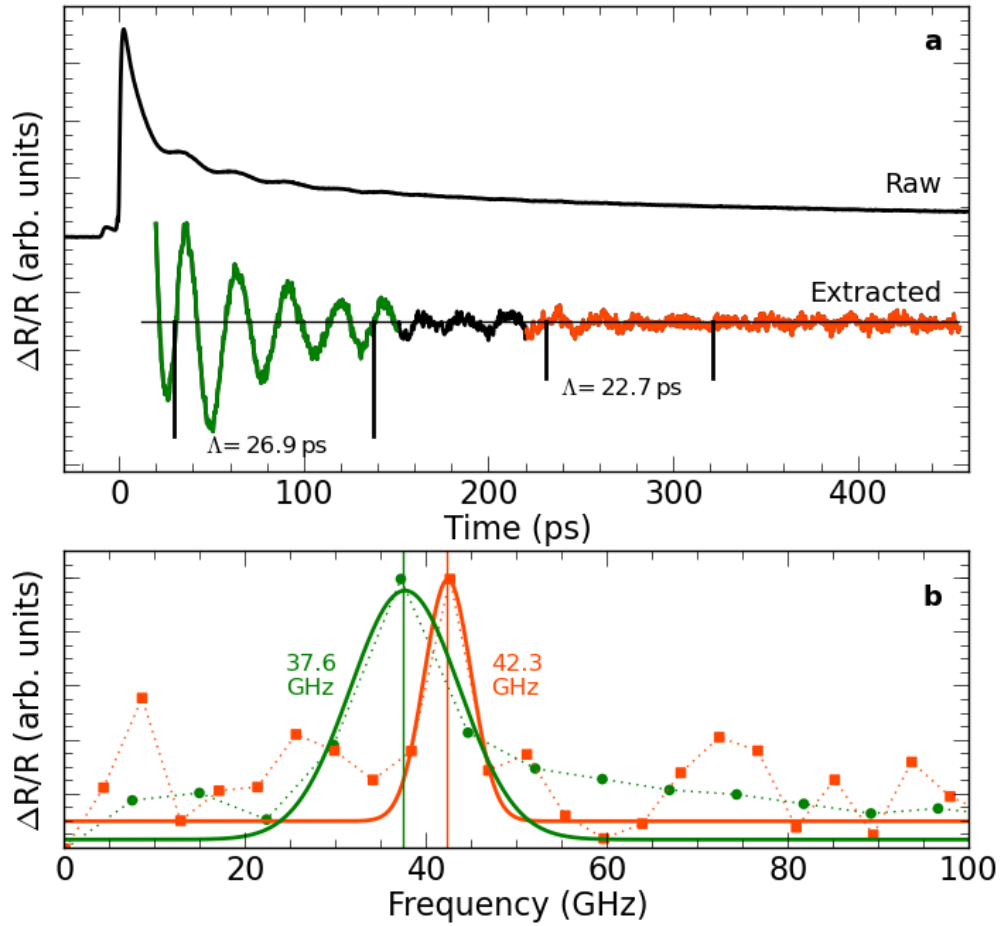


Figure 2.3: Transient reflectivity of 500 nm layer InAs on GaAs in the time (a) and frequency (b) domains. (a) Shows raw $\Delta R/R$ data (black) and data with the electronic component extracted below (scaling between the raw and extracted data is not the same). An early time window (15-150 ps, green) corresponding to when the phonon mode is in InAs and a late time window (220-445 ps, orange) corresponding to then the phonon mode it in GaAs are highlighted in the extracted data. The frequency domain data in (b) corresponds to these time windows. Data points (Circles/Squares connected by dotted lines) along with a Gaussian fit (solid lines) are shown.

for the oscillation in ΔR at a probe angle of incidence θ (Ref. [109]), where v is the longitudinal acoustic phonon speed and the refractive index n is evaluated at the probe wavelength λ . Oscillations in ΔR can therefore arise from periodic changes to the refractive index, as created by acoustic phonon modes.

In the case of thin films the strain pulse will propagate through the film and into the substrate. The film and substrate will have different refractive indices, n , and different acoustic phonon speeds, v , (arising from the lattice properties). This will result in changes to the amplitude and frequency of the oscillations in the time-resolved reflectivity. Furthermore it means that there will be a limited time-window from which information about the phonon mode in the film can be extracted. The size of this time window will depend on the speed of the mode propagation in the film and on the thickness of the film. This aspect of measuring acoustic phonons in thin films with transient reflectivity has previously been reported in semiconductors[105] and in multiferroics[96].

Example: Looking closely at Figure 2.3(a) it can be seen that there are periodic oscillations superimposed on the decay. In Figure 2.3(a), where the background electronic component has been extracted, these are clearer. These oscillations in the decay can be attributed to the propagation of a strain pulse in the sample. Figure 2.3(b) shows the time-windowed Fourier transform of these oscillations; 15-150 ps gives 37.6GHz while 220-455 ps gives 40 GHz. Analysis in the time domain over four oscillation periods (see Figure 2.3(a)) gives periods (and corresponding frequencies) of 26.9 ps (37.2 GHz) and 22.7 ps (44.1 GHz) for the InAs layer and GaAs substrate respectively. Although the extraction of the oscillation frequency from the frequency and time domain give slightly differing results, the direction of the shifts obtained are consistent. Given $n_{InAs}(800\text{ nm})=3.735$ and $n_{GaAs}(800\text{ nm})=3.683$ [128] from Equation 2.3 and this yields acoustic phonon speeds obtained from the frequency (*and time*) domain in InAs and GaAs of 4026 ms^{-1} (3983 ms^{-1}) and 4593 ms^{-1} (4788 ms^{-1})

respectively. This gives a time-window of 124 ps (*126 ps*) for the phonon mode being in the InAs film. This corresponds well with where the change in the oscillations appear to occur in the time-domain. Reported values put the longitudinal acoustic phonon speed in the [100] direction in InAs at $v_L[100]=3.8\times 10^3\text{ms}^{-1}$ and at $v_L[100]=4.73\times 10^3\text{ms}^{-1}$ in GaAs[129].

2.1.3 Magnons

Transient reflectivity can also couple to magnetic excitations in multiferroics. Photoexcitation of a magnetic ion can alter its spin-state. Magnons (coherent spin waves)[94] can modulate ΔR because the complex refractive index also couples to the magnetic permeability:

$$\tilde{n} = \sqrt{\epsilon\mu} \quad (2.4)$$

Here, ϵ and μ are the dielectric function and permeability. Coupling to a magnon with transient reflectivity has been reported for the hexaferrite $\text{Ba}_{0.5}\text{Sr}_{1.5}\text{Zn}_2\text{Fe}_{12}\text{O}_{22}$ [88].

Linear and Non-linear Optical Techniques

2.2 Ellipsometry

Ellipsometry allows the complex refractive index and thickness of thin films to be measured. The technique measures the change in the ratio of the s and p polarised light reflected from the sample, which is affected by the sample's properties. From this n and k can be extracted. The polarisation ratio is defined in terms of amplitude and phase components ($\tan(\psi)$ and Δ) given by;

$$\rho = \frac{r_p}{r_s} = \tan(\psi)e^{i\Delta} \quad (2.5)$$

where r_p and r_s are the amplitudes of the s and p components.

Figure 2.4 shows a schematic for how r_p and r_s are measured. Ellipsometry uses

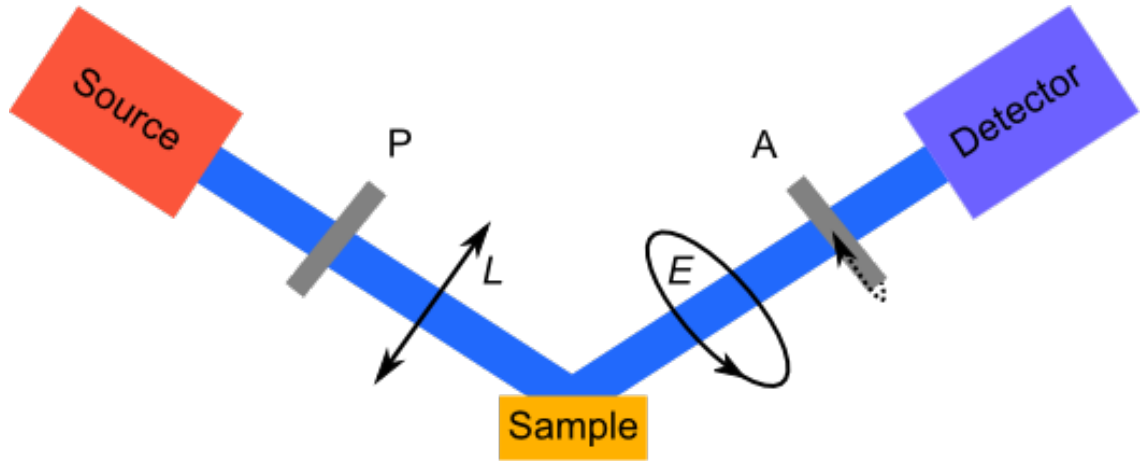


Figure 2.4: **Ellipsometry:** Schematic of a spectroscopic ellipsometer works. (*P*) Polariser. (*A*) Analyser (rotating). (*L*) Linearly polarised light. (*E*) Elliptically polarised light.

an unpolarised broadband source. The initial polarisation is set using a polariser. The light is reflected from the surface of the sample. Focusing optics can be used here to reduce the spot-size. Angles of incidence close to the Brewster angle allow for a maximum contrast in r_p and r_s . Measurements can also be taken at a number of incident angles to allow the fitting for extracting n and k to be carried out simultaneously over a number of known angles of incidence. The output polarisation is then recorded by means of a rotating analyser. CCD detectors can be used to simultaneously record the response across the entire spectrum.

n and k must be extracted from the measured ψ and Δ . To do this a layer model, considering the optical constants and thickness parameters of all individual layers of the sample must be used. A Tauc-Lorentz oscillator model[130] was used for the dielectric function, $\epsilon = \epsilon_1 + i\epsilon_2$ of the film. This model was varied through an iterative process where Ψ and Δ values were calculated from equation 2.5 calculated for a dielectric stack. The optical constants and thickness parameters are those that lead to the calculated Ψ and Δ values with the best fit to the experimental data.

2.2.1 Absorption Depth

The complex refractive index extracted from the ellipsometry results also allow the absorption depth to be calculated. Knowing this value at one of both or the pump/probe wavelengths is critical for a number of the techniques used in this work. The absorption depth is given by:

$$\delta = \frac{\lambda}{4\pi k} \quad (2.6)$$

where the k is the imaginary part of the complex refractive index which is related to the dielectric function by:

$$\tilde{n} = n + ik = \sqrt{\tilde{\epsilon}} = (\epsilon_1 + i\epsilon_2)^{1/2} \quad (2.7)$$

2.3 Second Harmonic Generation (SHG)

In this work SHG experiments have been used to examine the structural characteristics and to confirm whether the samples under investigation are polar. Given the correct phase-matching conditions and a suitably high radiation intensity the second harmonic of the input radiation will be produced by the sample. In this process the nonlinear medium converts the fundamental frequency ω to a frequency of 2ω through the creation of a nonlinear polarisation;

$$P_i^{2\omega} = d_{ijk} E_j^\omega E_k^\omega \quad (2.8)$$

where d_{ijk} is the nonlinear optical coefficient tensor defined as;

$$d_{ijk} = \epsilon_0 \chi_{ijk}^{(2)} \quad (2.9)$$

where ϵ_0 and $\chi_{ijk}^{(2)}$ are the permittivity of free space and the second order nonlinear susceptibility tensor[92, 116, 131, 132]. The SHG tensor components give rise to important geometry considerations depending on the space group symmetry of the sample under consideration. It is worth noting that the Kerr effect, where the refractive index has an electric field dependence and for which there is not a symmetry matching requirement, can also contribute to nonlinear responses. However, fluence required to produce the Kerr effect is much greater than those accessible using the techniques, as discussed in the next paragraph, used in this work.

The experimental setup used to achieve this is shown in Figure 2.5. A mode-locked Ti:sapphire laser oscillator (4 MHz, 650 nJ, 50 fs) provided the fundamental beam at 800 nm (1.55 eV) for SHG measurements. A half wave plate was used to rotate the linear input polarisation (the polariser). The fundamental was focused tightly onto the sample generating the high electric fields required to produce the second harmonic. Measurements were carried out in both transmission and reflection geometries. Figure 2.5 shows the layout for the reflection geometry. The beam was re-collimated and the fundamental filtered out with a dichroic mirror and two short pass filters (400 nm pass). The signal was mechanically chopped after the first filter to allow the signal to be amplified by a lock-in process. A polariser (the analyser) was used after the filters to set the detection polarisation. Either a photodiode or photomultiplier tube (PMT), placed after the analyser, were used to detect the second harmonic.

Vibrational Mode Techniques

2.4 THz Time-Domain Spectroscopy (THz-TDS)

The THz region covers the range 100 GHz-20 THz. Through electro optical sampling the technique allows for the full reconstruction of the THz electric field in the time-domain. By Fourier transformation the change in both the amplitude and phase of

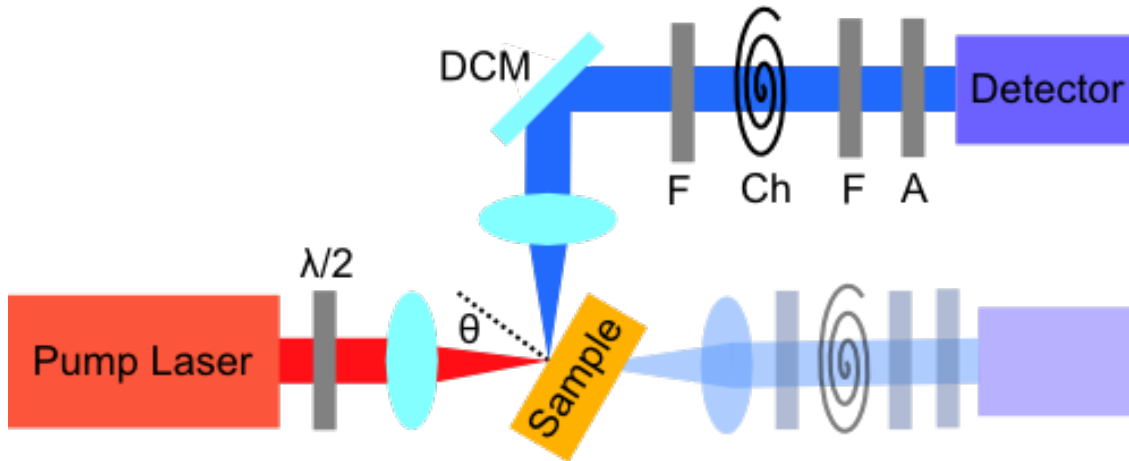


Figure 2.5: **SHG**: Schematic of experimental setup for the second harmonic experiment in reflection and transmission (faded). ($\lambda/2$) Half wave plate. (*DCM*) Dichroic mirror. (*F*) Filter (400 nm). (*Ch*) Chopper. (*A*) Analyser.

frequency components can be extracted. When the THz transmission of a sample is compared to a suitable reference (e.g a blank substrate) the complex dielectric function of the sample can be extracted directly[133].

A schematic of the experimental set up for THz-TDS is shown in Figure 2.6. Ultra short pulses were generated from a mode-locked Femtosource Scientific Pro Ti:Sapphire oscillator (20 fs , 74 MHz, 10nJ, $\lambda=800\text{nm}$). The beam was split into two parts; one to generate the THz and the other part to be used in the THz detection (*Gate*). Since there are some strong absorption lines from atmospheric water vapour in the THz region, the THz generation and detection is carried out under vacuum.

THz pulses were generated using a photoconductive switch (PCS)¹[136]. A PCS consists of a semiconducting material onto which surface contacts with a gap are deposited. Here a GaAs epilayer PCS with a $300\mu\text{m}$ strip gap was used. When a femtosecond pulse is focused onto the semiconductor photoexcited electron-hole pairs are generated. These are then accelerated by an electric field, achieved by applying a bias voltage across the gap. This moves the generated electrons and holes towards the

¹Other forms of THz generation include air Plasma generation[134] and nonlinear optical rectification[135]. Different generation techniques give different bandwidths and THz intensities. These difference can be critical in the selection of a suitable generation method.

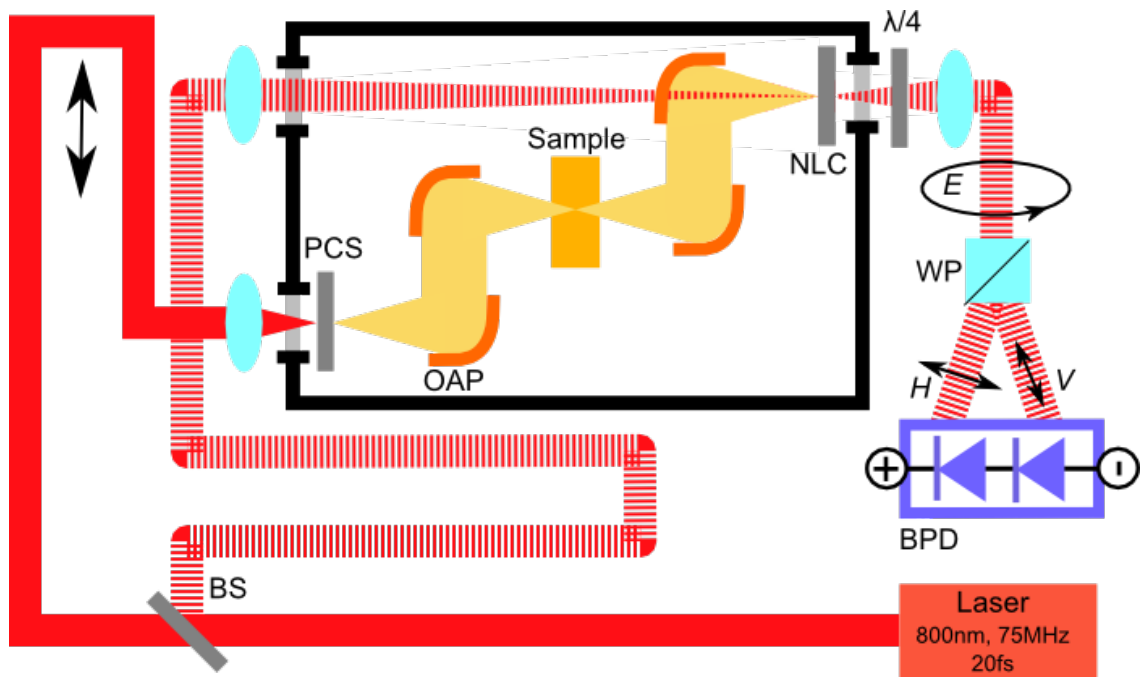


Figure 2.6: **THz-TDS:** Schematic of the experimental setup for the THz-TDS experiment. (*BS*) Beam splitter. (\updownarrow) Delay stage. (*PCS*) Photoconductive switch. (*OAP*) Off-axis parabolic mirrors. (*NCL*) Non-linear crystal. ($\lambda/4$) Quarter wave plate. (*WP*) Wollaston prism. (*E*) Elliptically polarised. (*H*) Horizontally polarised. (*V*) Vertically polarised. (*BPD*) Balanced photodiode detector. Black box: Vacuum chamber.

oppositely charged electrodes causing a transient electric dipole to be set up. This then radiates an electromagnetic pulse with THz frequencies[137]. Once generated the THz radiation is collimated and focused onto the sample using a pair of gold off-axis parabolic mirrors (OAPs). A second pair of OAPs is then used to re-collimate the THz radiation and focus it onto the detection crystal.

The THz radiation was detected using electro-optic sampling²[135]. Electro-optic sampling relies on the Pockels effect, where a birefringence is induced by an applied electric field. This effect occurs when the THz electric field is present in the detection crystal. When the linearly polarised gate beam is also present this will result in its polarisation being rotated. Subsequent to the detection crystal a $\lambda/4$ waveplate converts the rotated gate beam to an elliptical polarisation (see Figure 2.6). A Wollaston Prism then separates the elliptically polarised gate beam into linearly horizontal and vertical polarised components. These are then detected by two separate photodiodes. The voltage difference between the signals on the two photodiodes is then recorded (balanced photodiode circuit). As the probe beam is delayed with respect to the gate beam this traces out the amplitude and phase of the THz pulse in the time domain. The $\lambda/4$ waveplate is orientated such that in the absence of any THz radiation (and so no rotation of the gate beam's polarisation occurs) the output will be circularly, rather than elliptically polarised. This means that zero voltage difference on the balanced photodiode circuit corresponds to zero THz electric field. Amplification of the balanced photodiode signal was achieved with a lock-in amplifier. This amplifies a signal at a given modulation frequency. Here a modulation in the signal was achieved by applying a square wave modulation to the bias voltage on the PCS, which periodically flips the polarity of the THz radiation.

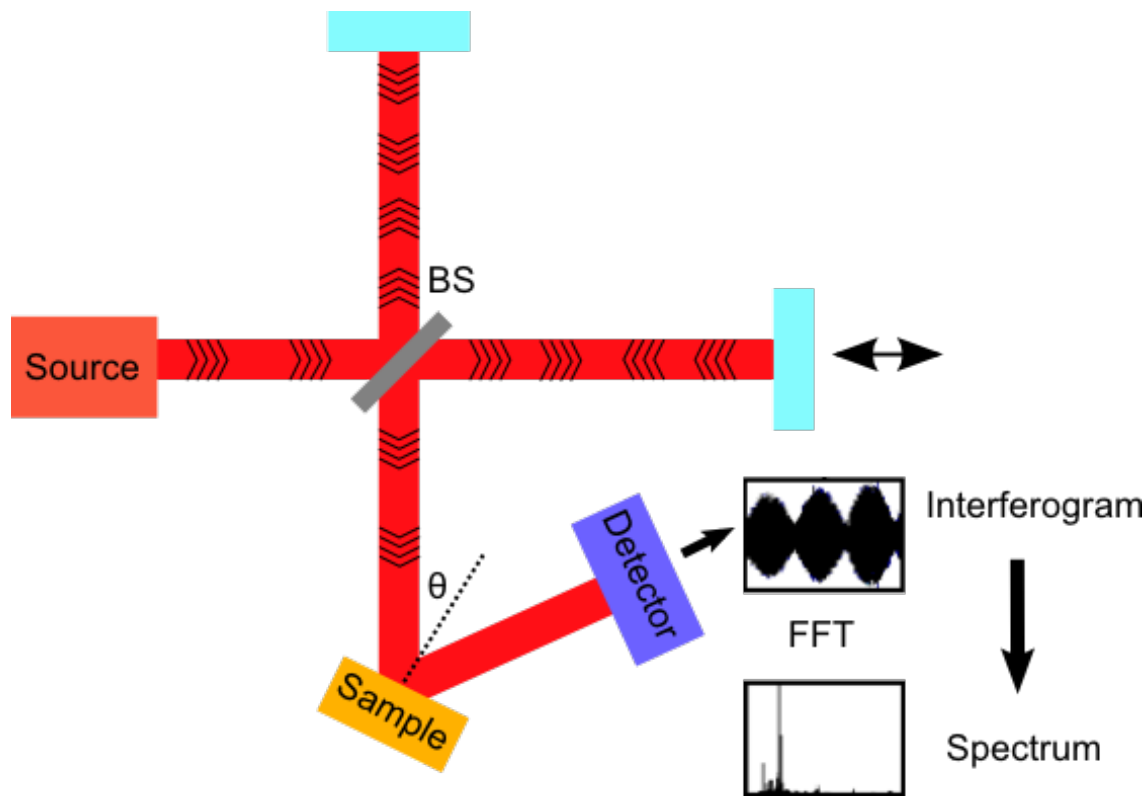


Figure 2.7: **FTIR:** Schematic of how FTIR spectroscopy works. (*BS*) Beam splitter. (\updownarrow) Moving mirror.

2.5 Fourier Transform IR Spectroscopy (FTIR)

Fourier transform infrared spectrometry (FTIR) allows modes above the energy of the THz range to be examined. A schematic of how this is achieved can be seen in Figure 2.7. A broadband source is used as the input to a Michelson interferometer. The interferometer produces an interferogram generated by splitting the source beam into two arms with a beamsplitter. Of these two arms one is of a fixed length and the other of a varying length. The beams on each of the arms are reflected back towards the beamsplitter where their amplitudes are re-combining interferometrically. The wavelengths involved in the interference are a function of the length of the moving arm. From this the spectrum of the source can be re-constructed by Fourier trans-

²Akin to the generation methods photoconductive antenna [136] and air-plasma detection [138] are alternative techniques.

formation. A sample can be placed in the output of the interferometer to obtain the reflectivity (or absorption) of the sample across the range of the source. The choice of source, beam splitter and detector determine the energy range over which the spectrum can be measured. In this work measurements taken were with a Bruker Vertex 70v spectrometer in the mid-IR (MIR) and far-IR (FIR), using a globar light source and the following beam splitters and detectors:

MIR: KBr beamsplitter and DLaTGS³ detector, (40-1000 meV)

FIR: Si beamsplitter and DTGS detector (10-90 meV)

2.6 Raman Spectroscopy

Raman spectroscopy yields complementary information to FTIR and can be used to probe low-energy modes such as molecular or lattice vibrations. Raman scattering is the inelastic scattering of light. Phonons mode are excited, which scatter light at the excitation energy shifted by the energy of the mode. As the scattered signal is small the technique requires an intense excitation source, i.e. a laser. The frequency shift for scattered phonons is quite small, so it is not only necessary to resolve this weak signal, but one which is close to the strong excitation wavelength.

Figure 2.8 shows a schematic of how this can be observed experimentally. A Renishaw inVia Reflex Raman microscope was used to take these measurements. Here the excitation laser was first expanded in the beam expander then focused onto the sample with a microscope lens, thus achieving a high excitation intensity. The scattered light along with the specularly reflected excitation beam was then collected in a backscattering geometry using the same microscope lens. To remove the fundamental laser frequency the beam was first passed through a holographic notch filter. A

³DTGS and DLaTGS are deuterated triglycene sulphate and deuterated L-alanine doped triglycene sulphate respectively.

diffraction grating monochromator allowed the Raman signal ν shift wavelength to be measured. This extraction method does not allow modes with energies very close to the fundamental (e.g. <20 meV) to be examined owing to the filter's cut off. To observe smaller shifts extraction of the fundamental can be done using a grating monochromator to remove the pump.

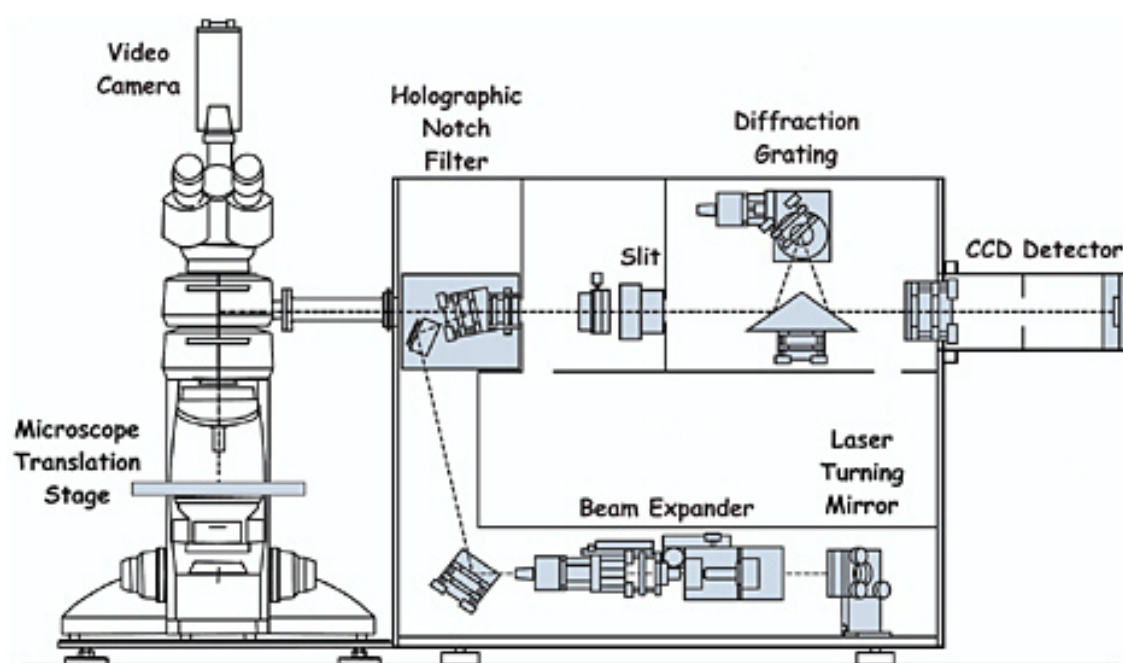


Figure 2.8: **Raman Spectroscopy:** Schematic diagram of a Raman microscope (Renishaw RM1000) [Image taken from "Scientific Examination of Art: Modern Techniques in Conservation and Analysis (2005) / Raman Microscopy in the Identification of Pigments on Manuscripts and Other Artwork" Robin J. H. Clark]

Chapter 3

Coherent magnon and acoustic phonon dynamics in tetragonal and rare-earth-doped BiFeO_3 multiferroic thin films

3.1 Introduction

This chapter reports a study of dynamic magnetoelectric coupling in BiFeO_3 (BFO) thin films. The influence of tetragonality and of lanthanide substitution (Dy and La; $\text{Bi}_{1-x-y}\text{Dy}_x\text{La}_y\text{FeO}_3$) on the perovskite A -site are examined. Coherent magnons and acoustic phonons were impulsively excited using femtosecond ultraviolet pulses and were tracked by a time-delayed infrared probe. Strain pulses carried by longitudinal acoustic phonons were utilized to obtain the films' elastic moduli, in conjunction with spectroscopic ellipsometry. Spectroscopic ellipsometry and DFT were used to discuss the complex refractive index and orbital hybridization. A weak ferromagnetic order, induced by either magnetisation in the growth direction or by tetragonality, created a magnon oscillation at 75 GHz, indicative of a Dzyaloshinskii-Moriya (DM) interaction energy of 0.31 meV.

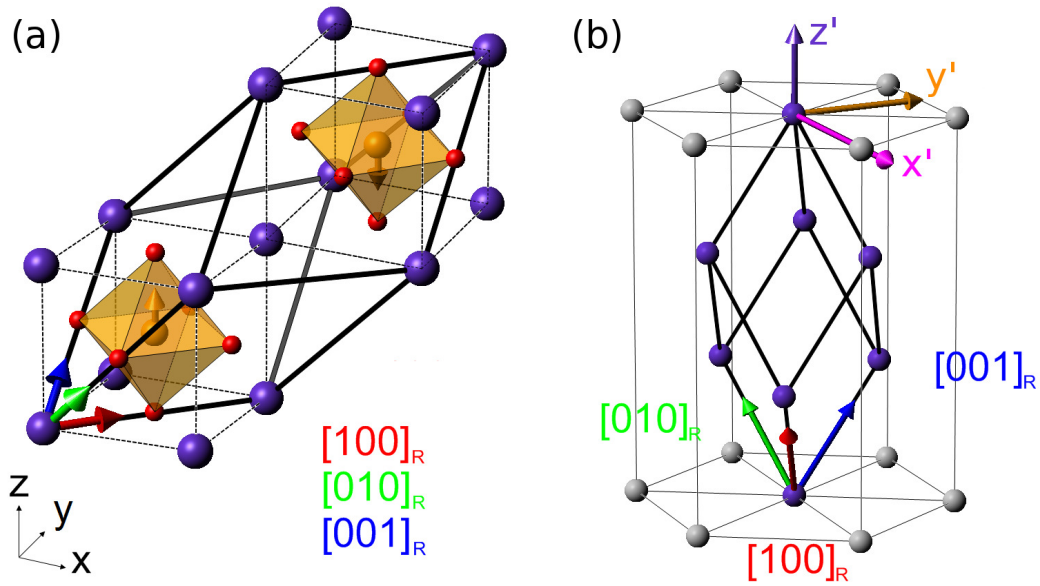


Figure 3.1: Crystal structure of different phases of BiFeO₃. (a) Relationship between pseudocubic perovskite structure (thin lines) and rhombohedral unit cell (thick lines). Bismuth, iron, and oxygen atoms are drawn in blue, orange and red, while orange arrows denote spins. The Cartesian axes x , y , z of the pseudocubic structure and the unit vectors of the rhombohedral cell are also shown. (b) The Cartesian axes x' , y' , z' used to describe the properties of the rhombohedral cell (blue spheres, thick lines) are shown along with the trigonal structure (gray spheres, thin lines), which is the standard setting used in theoretical works.

3.2 Sample characterization

3.2.1 Growth and X-ray Diffraction

Thin films of rhombohedral-like BiFeO₃ (R-BFO), tetragonal BiFeO₃ (T-BFO), Bi_{0.7}Dy_{0.3}FeO₃ (BDFO) and Bi_{0.6}La_{0.1}Dy_{0.3}FeO₃ (BLDFO) were grown on (001)-oriented LaAlO₃ and MgO substrates by pulsed laser deposition [27, 28]. The substrate used is indicated by the suffix /L or /M (e.g. BDFO/M). Film thicknesses were in the range from 290 nm to 450 nm (from ellipsometry, see Section 3.2.2), with a surface roughness of less than 20 nm (from AFM, see Figure 3.2). While monoclinic or tetragonal phases are stabilized by compressive strain on LaAlO₃ for thicknesses below 300 nm, thicker films exhibit strain relaxation towards the bulk rhombohedral phase [12].

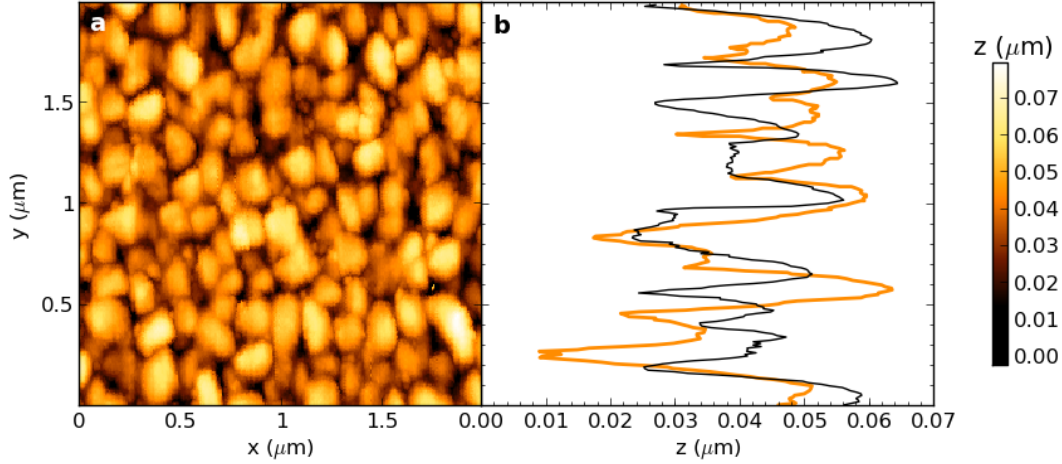


Figure 3.2: Atomic Force Microscopy (AFM) on BDFO/L. (a) 2D surface roughness colour plot. (b) Height profiles along two different lines.

High-resolution $\omega - 2\theta$ X-ray diffraction scans and reciprocal space maps were used to examine the crystal structure of the films, using a four-circle x-ray diffractometer (PANalytical X'pert Pro) with a Cu $K\alpha$ source and a monochromator. In Figure 3.3(c) the pseudocubic (002) peak of the LaAlO_3 substrate (space group $R\bar{3}m$, $a = 3.789 \text{ \AA}$, $\alpha = 90.12^\circ$) is visible at $2\theta = 48.0^\circ$. In contrast, the (002) cubic peak for MgO (space group $Fm\bar{3}m$, $a = 4.212 \text{ \AA}$) is at 42.9° . The weaker peaks around $2\theta = 46^\circ$ originate from a rhombohedral-like phase in the epitaxial films, while the peak at $2\theta = 38.5^\circ$ indicates the tetragonal-like phase [12]. Reciprocal space maps (RSM) of diffraction peaks close to the substrate's pseudocubic directions were utilized to obtain a component of the films' periodicity in the plane, as shown by the examples in Figure 3.3(a) and (b) close to the $(103)_c$ substrate peak for LaAlO_3 . For a 552 nm thick layer of BDFO/L the film can be seen to be predominantly relaxed towards a bulk-like phase, as the in-plane component q_x of the scattering vector does not match that of the substrate (Figure 3.3(a)). Conversely, RSMs for the tetragonal-like (T-like) films indicated that no in-plane relaxation occurred (q_x the same for epitaxial film and substrate), as shown in Figure 3.3(b).

A rhombohedral cell (space group $R3c$) provided a good fit for the BDFO and

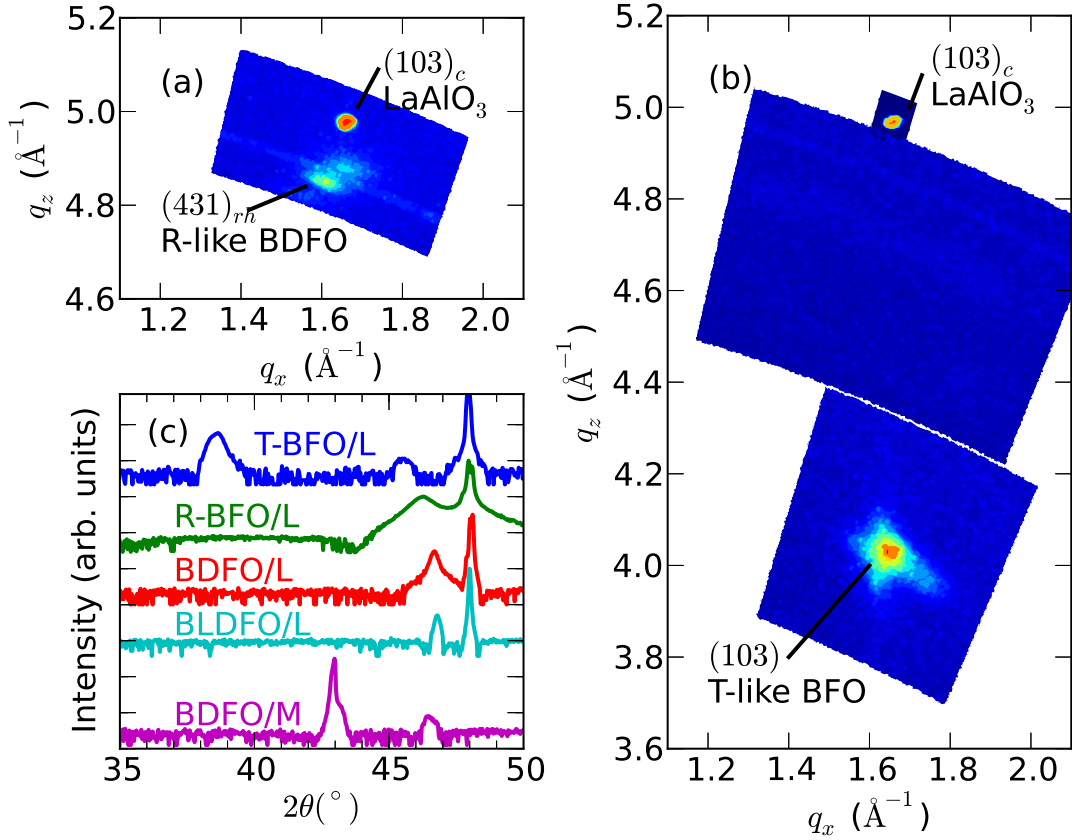


Figure 3.3: (a) Reciprocal space map (RSM) around the $(103)_c$ substrate peak for R-like BDFO/L. (b) RSM around the $(103)_c$ substrate peak for T-like BFO/L. (c) $\omega - 2\theta$ X-ray diffraction scans for (from top to bottom) T-like BiFeO₃ (300 nm), R-like BiFeO₃ (300 nm), Bi_{0.7}Dy_{0.3}FeO₃ (552 nm) and Bi_{0.6}La_{0.1}Dy_{0.3}FeO₃ (323 nm) on LaAlO₃, and Bi_{0.7}Dy_{0.3}FeO₃ (397 nm) on MgO. Note, although T-BFO/L and R-BFO/L are of similar thicknesses their PLD growth parameters differed, leading to the different structures observed.

BLDFO films, where the observed diffraction peaks lay close to the values for bulk BFO. Fits were obtained by calculating 2θ positions for various peaks (e.g. (110), (220), (330), (431), (442) in the rhombohedral setting) using the two free parameters (a and α), and finding the best fit to experiment graphically via a contour plot of the error. The unit cell parameters thus obtained were slightly smaller than bulk BFO [6], which has $a = 5.63\text{\AA}$, $\alpha = 59.4^\circ$, and are summarized in Table 3.1, Page 68. The tetragonal distortion to the pseudocubic cell was small for the rare-earth doped films, at $c/a < 1.01$ for BDFO and BLDFO. Two different undoped BFO films were

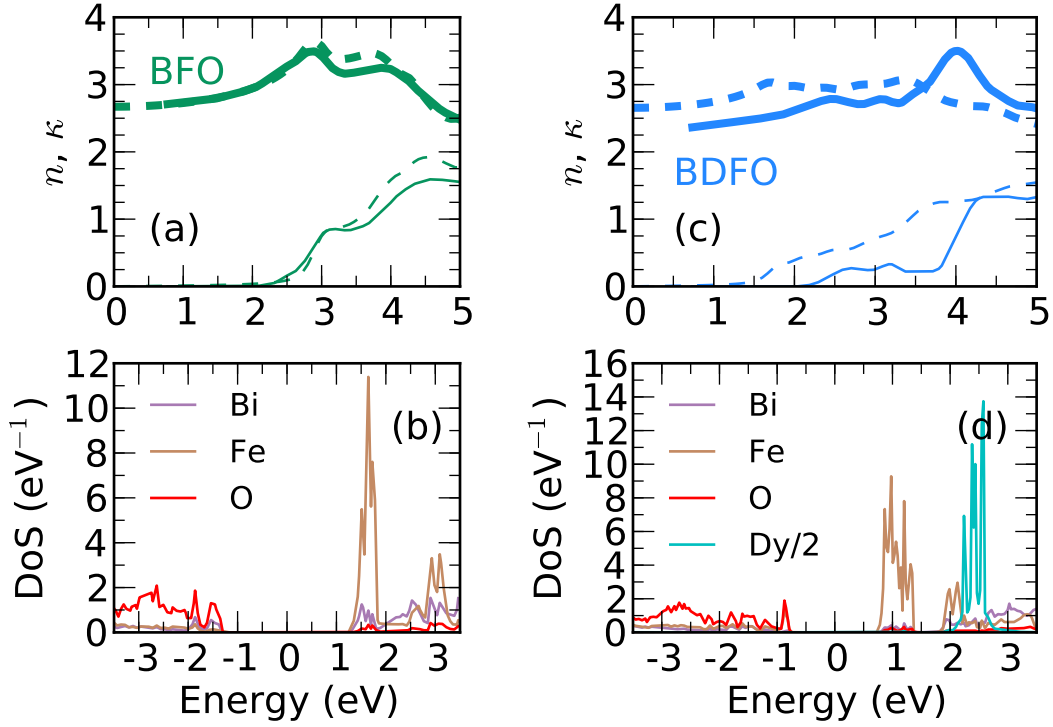


Figure 3.4: (a) The complex refractive index $\tilde{n} = n + i\kappa$ of R-BFO from ellipsometry (thick green line: n , thin green line: κ) is in close agreement with first-principles calculation (dashed lines, see text). (b) Atomic density of states (DoS) for R-BFO, from calculation. (c) and (d) show that n and κ for BDFO (blue lines, from ellipsometry) are suppressed in the range 0 – 5 eV in comparison to R-BFO. The density of states for Dy has been scaled down by a factor of 2.

explored: one with a weak tetragonal distortion $c/a = 1.03$ that was primarily rhombohedral (R-BFO, $a = 5.617\text{\AA}$, $\alpha = 58.7^\circ$), and a film with enhanced tetragonality $c/a = 1.23$ (T-BFO, $c = 4.68\text{\AA}$, $a = 3.789\text{\AA}$).

3.2.2 Ellipsometry and DFT

The complex refractive index $\tilde{n} = n + i\kappa$ of the films was characterized using variable-angle spectroscopic ellipsometry. The R-BFO and T-BFO films were found to have similar \tilde{n} to those previously reported [114], and were parameterised using a series of Tauc-Lorentz oscillators. \tilde{n} is reported in Figure 3.4(a) and (c) for R-BFO and BDFO. Substitution with Dy was found to reduce n in comparison to R-BFO, and

to decrease the band gap slightly.

First-principles calculations of \tilde{n} were performed for our experimental BFO cell dimensions using the LSDA+U approach and the Kubo-Greenwood formalism [139, 140]. A good match between simulation (dashed lines in Figure 3.4(b)) and experiment for BFO was obtained with a Hubbard $U = 6$ eV for Fe 3d electrons. The site-resolved density of states around the optical gap is shown in Figure 3.4(b), where the chemical potential is at zero energy. The highest valence band is a mixture of O 2p states and the Bi 6s lone pair responsible for ferroelectricity, while the lowest conduction band is predominantly Fe 3d in character, with some Bi 6p hybridization.

To attempt to model the optical properties of BDFO the experimental unit cell ($a = 5.535$ Å, $\alpha = 59.1^\circ$) was doubled in one dimension. One of the four Bi atoms was substituted by Dy, to allow a simulation of $\text{Bi}_{0.75}\text{Dy}_{0.25}\text{FeO}_3$, close to the experimental Dy doping level of 30 %. For dysprosium, a twenty electron valence orbital basis set was used ($5s^25p^64f^{10}6s^25d^0$), with $U = 6$ eV for the 4f electrons. While the simulated Dy magnetic moment in BDFO was $5.06 \mu_B$, in reasonable agreement with experiment ($5.87 \mu_B$ for DyFeO_3 , Ref. [141]), the optical properties are in much poorer accord with experimental data, as Figure 3.4(c) indicates. This may be in part due to spin-orbit interactions being neglected in the DFT calculations [139, 140], which are particularly important for Dy. The degree of convergence was also poorer than for a BFO supercell without Dy, as reported previously [142]. The simulated density of states for BDFO demonstrates a hybridization between the Fe 3d and Dy 4f orbitals, with a Fe 3d band appearing within the band gap of BFO that lowers the calculated bandgap. Experimentally this reduction is less pronounced, as evidenced by Figure 3.4(c).

3.2.3 Second Harmonic Generation

Second harmonic generation (SHG) can be used to examine the structural and polar properties of materials. A mode-locked Ti:sapphire laser oscillator (4 MHz, 650 nJ, 50 fs) provided the fundamental beam (800 nm or 1.55 eV) for SHG measurements in

transmission and reflection geometry. Either a photodiode or a photomultiplier tube (PMT), placed after an analyser and a set of short pass filters, were used to detect the second harmonic. Samples were mounted at $\theta = 45^\circ$ from normal incidence, and with the incident beam polarised at angle ϕ ($\phi = 0$ corresponding to p-polarisation), see Figure 3.5(a). For further details on SHG see Section 2.3 in Chapter 2.

In the transmission geometry, the SHG intensity varies with the angle of incidence θ of the pump beam. This is because the projection of the SHG nonlinear susceptibility tensor, d_{ijk} onto the polarisations of the pump beam varies as the incident angle is changed. For the p-in-p-out SHG polarisation geometry, as shown in Figure 3.5(a), the SHG intensity for a R-phase or T-phase of BFO (point groups $3m$ and $4mm$ respectively) is given by [132]:

$$I_{PP}(\theta) = I_0^2 t_p^2 (A f_x^2 \cos^2 \theta + B f_z^2 \sin^2 \theta + C f_x f_z \sin 2\theta)^2 \quad (3.1)$$

where:

θ = Angle of incidence

d_{ijk} = Nonlinear optical coefficients.

$f_{x,z}$ = Linear Fresnel coefficients.

$\tilde{f}_{x,z}$ = Nonlinear Fresnel coefficients.

t_p = Fresnel coefficients for transmission of p-polarised SHG at the substrate-air interface.

I_0 = Intensity of the fundamental light.

The A, B, C Coefficients are functions of d_{ijk} (d_{31} , d_{31} and d_{15}) and $\tilde{f}_{x,z}$. The space group of the material will determine which of the components of the susceptibility tensor, d_{ijk} , can be non-zero. As such the SHG intensity, $I_{PP}(\theta)$ will vary depending on the space group of the material. The dashed and dotted black curves in Figure 3.5(b) show theoretical predictions for the angular dependence of the SHG intensity for tetragonal and rhombohedral phases of BiFeO₃ reported by Kumar *et al.* [132]. Notably, the two phases can be distinguished as the expected SHG inten-

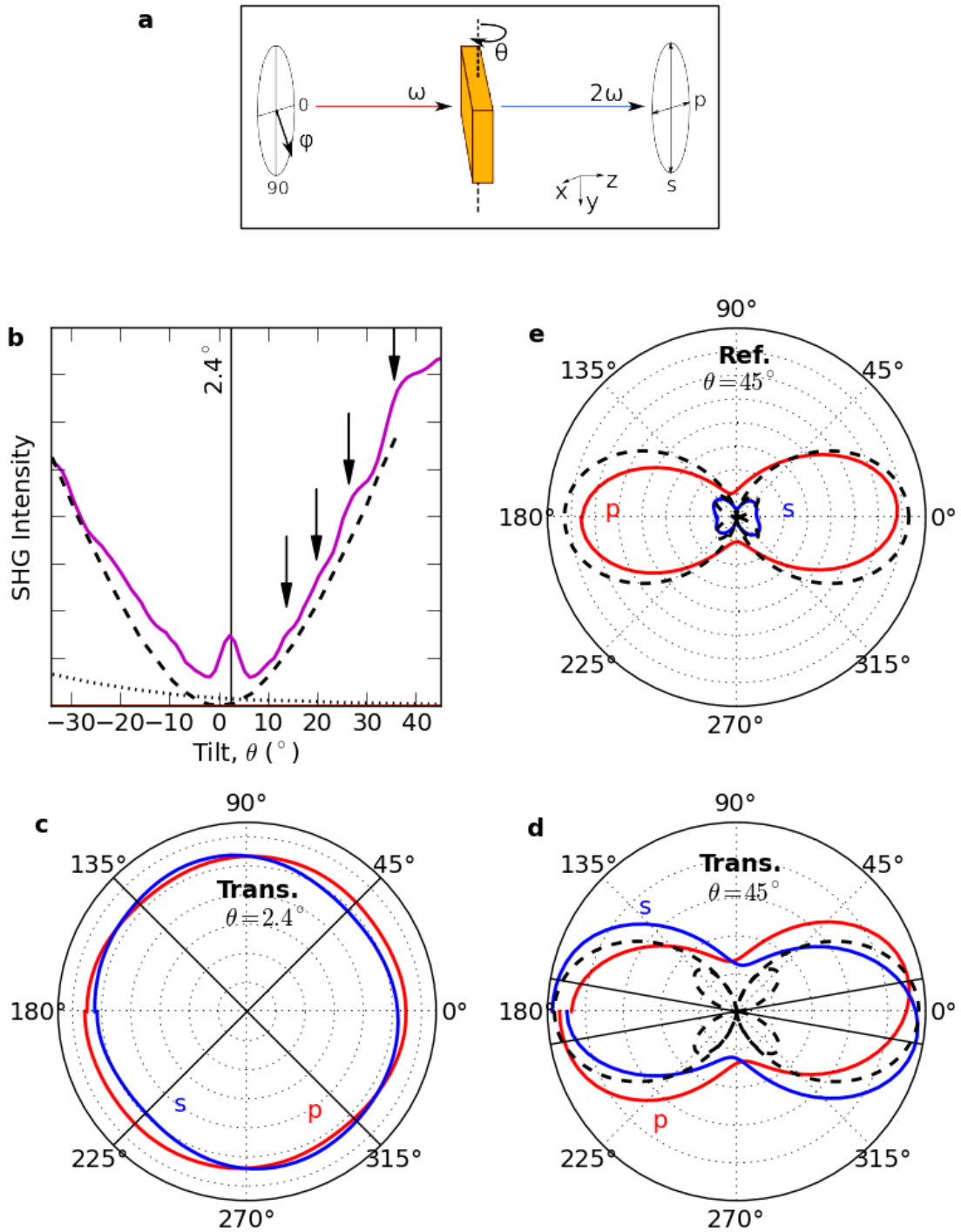


Figure 3.5: (a) Experimental setup (b) Purple: Angular tilt dependence of SHG signal obtained in p-in-p-out configuration. Black: Theoretical predictions for a R-phase (dotted) and a T-phase as described by Equation 3.1 [Taken from Kumar et al. [132]] (c) and (d) Transmission geometry ϕ dependence polar plots for $\theta \sim 0^\circ$ and $\theta=45^\circ$ respectively. (e) Reflection geometry ϕ dependence polar plot $\theta=45^\circ$ respectively. In (c-e) s and p indicate the detection polarisation. The dashed black lines in (d) and (e) show predicted intensities with respect to ϕ for s (4-lobes) and p (2-lobes) detection in the T- phase as given by Equations 3.4 and 3.3

sity at normal incidence ($\theta = 0$) is zero for the tetragonal film and non-zero for the rhombohedral film.

The purple curve in Figure 3.5(b) shows the measured SHG intensity dependence on the incident angle θ for a 300 nm T-BFO/L film. The curve resembles the theoretical angular dependence for the tetragonal phase but with the addition of an extra peak at $\theta \sim 0$. From the X-ray data (Figure 3.3) the film was seen to be predominantly tetragonal, with a weak rhombohedral component visible at $2\theta=46^\circ$. This means that the SHG should have both tetragonal and rhombohedral components. As such the presence of a peak in the SHG intensity at normal incidence could result from the rhombohedral component. An alternative explanation is that the peak originates from an interference effect. A periodic oscillatory feature (indicated by the arrows) was present in the measurement, which bears resemblance to the response observed for layered structures. There, interference fringes arose from the phase difference between the two SHG waves generated from opposite faces of the sample [143, 144, 145].

Figures 3.5(c) and (d) show polar plots of the SHG intensity as a function of the polarisation angle ϕ at tilt $\theta \sim 0^\circ$ (centre of peak, where a minimum would be expected for a pure T-phase) and $\theta=45^\circ$ respectively in transmission geometry. The polar SHG plots can be qualitatively understood as follows. Since the sample is rotated around the vertical axis by $\theta = 45^\circ$ there is a maximum component of the electric field of the incident beam along the c -axis for a p -polarised fundamental. This leads to maxima in the SHG intensity at $\phi = 0$ and $\phi = 180^\circ$. For the rhombohedral and tetragonal phases with point groups $3m$ and $4mm$ respectively, the ϕ -dependence of the detected SHG intensity is given by:

Rhombohedral:

$$I_{(110)}(\phi) = K_1(\cos^2 \phi + K_2 \sin^2 \phi) + K_3 \sin^2 2\phi + K_4 \sin 2\phi(\cos^2 \phi + K_2 \sin^2 \phi) \quad (3.2)$$

Tetragonal:

$$I_p(\phi) = (P \cos^2 \phi + Q \sin^2 \phi)^2 \quad (3.3)$$

$$I_s(\phi) = R \sin^2 2\phi \quad (3.4)$$

where the constants K_1, K_2, K_3, K_4, P, Q and R are linked to the SHG coefficients d_{31}, d_{31} and d_{15} , as described by Kumar *et al.*[132].

As was evident from the tilt dependence, an SHG signal is present at $\theta \sim 0^\circ$. There are similarities between this and the predicted intensity for a rhombohedral phase [132]. From the theoretical predictions for the tilt dependence for the T- and R- phases (Figure 3.5(a)) at $\theta=45^\circ$ it would be expected that, if present, the tetragonal phase would dominate the SHG signal. The expected intensity for a tetragonal phase showing a double-lobed (quadruple-lobed) pattern for p-polarised (s-polarised) detection [132] is shown by the dashed black lines in Figures 3.5(e). Clearly the response seen here for s-out does not correspond well to this. Reflection geometry data for the same film at $\theta=45^\circ$ is presented along with the predictions for a tetragonal phase in Figures 3.5(e). Here a PMT detector was used, however similar results were obtained using GaP photodiode detection. The expected tetragonal response for $I_s(\phi)$ can now be seen clearly.

Various factors could have led to the difference seen in the transmission geometry. Both the s and p detection polarisation results resemble the prediction for the p detection but tilted by $\pm 10^\circ$. This could arise from birefringence in the substrate or film leading to a different response along the fast and slow axes, resulting in a polarisation rotation. If the response arises from the film then it would be expected that the effect would be more pronounced in these films than in the mixed phase films previously studied by Kumar *et al.* This is because Kumar *et al.*'s films were 160 nm thick on LAO, while here the thickness here is 300 nm, also on LAO. The

greater thickness would result in an escalation of this effect. Alternatively, the effect could result from the substrate. LAO has birefringent twin domains [146], differences in these could potentially lead to differences in the SHG response. Furthermore, scattering from surface roughness could also lead to depolarisation resulting in the effects seen.

The presence of a clear SHG signal indicates a non-centrosymmetric crystal structure at room temperature for the films. Furthermore the responses have been seen to be consistent with the mixed T+R phase for the 300 nm BFO film and as shown in the X-ray.

3.3 Time-Resolved Reflectivity

The fundamental beam from a mode-locked Ti:sapphire laser oscillator (4 MHz, 650 nJ, 50 fs) was doubled in frequency to 400 nm (3.1 eV) to photoexcite the multi-ferroic films at a fluence of $60\mu\text{Jcm}^{-2}$. The transient optical reflectivity subsequent to excitation was detected using a time-delayed fraction of the fundamental beam (800 nm or 1.55 eV), which was incident on the sample at close to normal incidence (i.e. along [001] in the pseudocubic representation, see Figure 3.1). The absorption depth of the samples at the pump and probe wavelengths are $\delta(400\text{ nm}) = 40 - 100\text{ nm}$ and $\delta(800\text{ nm}) = 1.5\text{ }\mu\text{m}$ (as determined by Equation 2.6).

The time-resolved reflectivity of the R-BiFeO₃/LaAlO₃ film is shown in Figure 3.6(a), under photoexcitation at 3.1 eV. The sharp rise at zero time corresponds to the rapid transfer of electrons from the hybridized O 2*p*/Bi 6*s* valence band to the Fe 3*d*/Bi 6*p* conduction band (see Figure 3.4). A similar rapid rise and decay in reflectivity has been reported in recent studies of bulk BFO [98, 99] and thin films of BFO grown on SrTiO₃ [100, 101] and YSZ [100]. The non-exponential decay can be attributed to two timescales for electronic relaxation, initially via optical phonon emission as in III-V semiconductors [147]. The slower recovery could result from

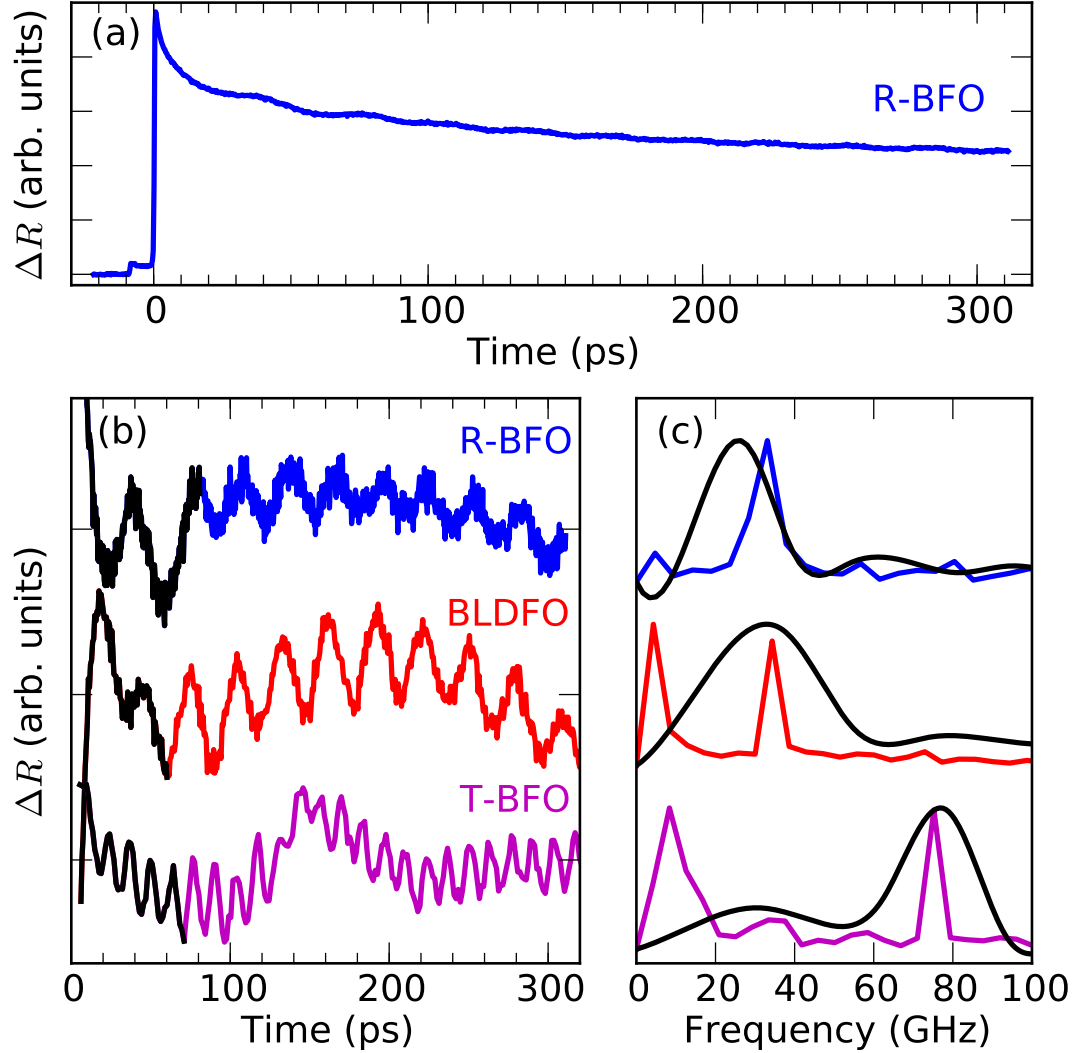


Figure 3.6: (a) Time-resolved reflectivity of R-BFO film on LaAlO_3 . Coherent oscillations in the reflectance are shown in the (b) time and (c) frequency domains after subtraction of the electronic response, for R-BFO (top, blue), BLDFO (middle, red) and T-BFO (bottom, purple) films on LaAlO_3 . Spectra are shown normalized to their maximum values. At early times (black) the acoustic phonon pulse is within the film, while at later times (coloured) the acoustic pulse propagates through the substrate (Section 3.4). The T-BFO films exhibit a strong oscillation at 75 GHz, attributed to a magnon (Section 3.5).

incoherent acoustic phonon emission, spin-lattice coupling [100] or radiative recombination [98].

A distinct oscillation can be seen superimposed on the reflectivity transient in Figure 3.6(a). The background quasi-static component was removed numerically in order to examine the oscillation, as shown in Figure 3.6(b) for R-BFO (top), BLDFO (middle) and T-BFO (bottom) in the time-domain. The corresponding frequency domain spectra (normalized) are given in Figure 3.6(c). While the R-BFO and BLDFO datasets are dominated by lower-frequency oscillations, the T-BFO data exhibits a higher frequency oscillation. Section 3.4 discuss the lower-frequency modes, which originate from acoustic phonons, and the higher frequency mode, which can be assigned to a magnon, is discussed in Section 3.5.

As discussed in Sections 2.1.2 and 2.1.3 transient reflectivity measurements can couple to both phonons and magnons through the relations given in Equations 2.3 and 2.4 respectively. Transient reflectivity has been seen to couple to phonons in BFO [99, 101] and LuMnO₃ [106, 107], while magnon modes can modulate ΔR , as reported for the hexaferrite Ba_{0.5}Sr_{1.5}Zn₂Fe₁₂O₂₂ [88]. Further discussion on coupling to phonons and magnons with transient reflectivity and other optical techniques can be found in Chapter 1, Section 1.4. The two mechanisms can be distinguished by their time dependence, the variation of the mode frequency with probe wavelength, and the influence of magnetic field and temperature.

3.4 Elastic Moduli and Acoustic Phonons

3.4.1 Acoustic Phonon Contribution to Reflectivity Change

Given that $f = 2nv/\lambda$ (Equation 2.3) and that the longitudinal acoustic phonon speed and the refractive index will change on entering the substrate, there should be a change in the measured mode frequency at the boundary (see discussion in Section 2.1.2). For the R-BFO film this change in period is evident at 80 ps in Figure 3.6(b). The

frequency domain analysis in Figure 3.6(c) has been time-windowed to take this into account, with black lines showing early times, where the mode is in the film, and coloured lines corresponding to later times, when the mode has propagated into the substrate. Time-domain fits (not shown) were also utilized to determine oscillation frequencies, particularly for early times.

3.4.2 Elastic Properties of Anisotropic BiFeO₃

In anisotropic media, Hooke's law is written;

$$X_{ij} = c_{ijkl}x_{kl} \quad (3.5)$$

where the stress X_{ij} and strain x_{ij} are second-rank tensors linked by the fourth-rank elastic modulus tensor c_{ijkl} . Symmetry and energy arguments [148, 149] permit the reduction of c_{ijkl} to a 6×6 matrix, \mathbf{c} , which can be linked to the acoustic wave speed v_{ij} and density ρ via $c_{ij} = \rho v_{ij}^2$ (Voigt notation). The elastic matrices are as follows for cubic (C), tetragonal (T) and rhombohedral/trigonal (R) phases:

$$\mathbf{c}^C = \begin{pmatrix} c_{11} & c_{12} & c_{12} & 0 & 0 & 0 \\ c_{12} & c_{11} & c_{12} & 0 & 0 & 0 \\ c_{12} & c_{12} & c_{11} & 0 & 0 & 0 \\ 0 & 0 & 0 & c_{44} & 0 & 0 \\ 0 & 0 & 0 & 0 & c_{44} & 0 \\ 0 & 0 & 0 & 0 & 0 & c_{44} \end{pmatrix} \quad (3.6)$$

$$\mathbf{c}^T = \begin{pmatrix} c_{11} & c_{12} & c_{13} & 0 & 0 & 0 \\ c_{12} & c_{11} & c_{13} & 0 & 0 & 0 \\ c_{13} & c_{13} & c_{33} & 0 & 0 & 0 \\ 0 & 0 & 0 & c_{44} & 0 & 0 \\ 0 & 0 & 0 & 0 & c_{44} & 0 \\ 0 & 0 & 0 & 0 & 0 & c_{66} \end{pmatrix} \quad (3.7)$$

$$\mathbf{c}^R = \begin{pmatrix} c_{11} & c_{12} & c_{13} & c_{14} & 0 & 0 \\ c_{12} & c_{11} & c_{13} & -c_{14} & 0 & 0 \\ c_{13} & c_{13} & c_{33} & 0 & 0 & 0 \\ c_{14} & -c_{14} & 0 & c_{44} & 0 & 0 \\ 0 & 0 & 0 & 0 & c_{44} & c_{14} \\ 0 & 0 & 0 & 0 & c_{14} & (c_{11} - c_{12})/2 \end{pmatrix} \quad (3.8)$$

where the point groups 3m and 4mm were assumed for the rhombohedral and tetragonal phases respectively. Here, the matrix subscripts are a shorthand notation for the tensor subscripts, defined as $1 \equiv 11$, $2 \equiv 22$, $3 \equiv 33$, $4 \equiv 23$, $5 \equiv 31$ and $6 \equiv 12$. A tetragonal distortion along [001] will alter c_{33} without changing $c_{11} = c_{22}$, and will tend to reduce the elastic constant such that $c_{33}^T < c_{11}^C$. Similarly, a rhombohedral expansion along [111] lowers the elastic constant in this direction, $c_{33}^R < c_{11}^C$.

Assuming a pseudocubic [001]-oriented crystal, the almost collinear photoexcitation and probe beams of the experimental geometry allow $c_{11}^C = c_{1111}^C$ to be determined, namely the elastic modulus for stress and strain along the pseudocubic [001] direction. For a tetragonal crystal the experiment probes c_{33}^T , along the direction of the tetragonal distortion (z axis). The case of a rhombohedral crystal is more complex: the elastic matrix as written in Equation 3.8 uses a Cartesian co-ordinate system x' , y' , z' defined with z' parallel to the [111] rhombohedral direction, y' parallel to a projection of a unit vector of the rhombohedral cell into the plane normal to z' ,

and x' completing the orthogonal set [150]. These co-ordinate systems are shown in Figure 3.1.

3.4.3 Results and Discussion

In order to separate the acoustic phonon contributions from the film and substrate ΔR datasets must be time-windowed, as discussed in Section 3.4.1 and illustrated in Figure 3.6(b). For R-BFO, the Fourier spectra of the time-windowed ΔR oscillation in Figure 3.6(c) revealed a frequency $f = 24$ GHz and $f = (33.7 \pm 0.5)$ GHz at early and late times respectively. The oscillation frequency in the LaAlO₃ substrate yields $v = (6740 \pm 100)$ ms⁻¹ using $n(800 \text{ nm}) = 2.0$, and thus $c_{11} = (296 \pm 6)$ GPa, corresponding well with $c_{11} = 290$ GPa for LA phonons propagating along [001] reported in Ref. [151]. An oscillation at the same frequency can be seen at late times in all samples on LaAlO₃, as the spectra in Figure 3.6(c) indicate. However, variations in the substrate's acoustic mode amplitude and/or frequency are discernible between different LaAlO₃ substrates (Figure 3.6(c)) and for the same substrate when varying magnetic field or temperature (Figures 3.7 and 3.8). A possible explanation is the existence of birefringent twin-domains [152] in LaAlO₃, which have an extent of 10-100 μm , comparable to the size of the focussed probe beam. Probing multiple or different twin domains, with varying orientation and refractive index, may alter the amplitude and/or frequency of the substrate mode. Lower frequency oscillations (< 20 GHz) discernible in these figures may indicate a contribution from substrate TA phonon modes (with lower elastic constants) to the time-resolved reflectivity [99], or may be artefacts from the finite length of the time-domain scans (around 300 ps).

The elastic moduli for the films were determined from the acoustic mode frequencies (> 20 GHz), and are summarized in Table 3.1 together with the structural parameters. The measured elastic constants range from 100-237 GPa, and depend on composition and crystal structure, as discussed below.

Time-resolved reflectivity has been used previously to determine the elastic con-

BiFeO₃

Material (label)	Unit cell	V_0 (Å ³)	\tilde{n} at 800 nm (400 nm)	f (GHz)	Propagation direction	Elastic modulus (GPa)	Reference
BiFeO ₃ on LaAlO ₃ (R-BFO/L)	rhombohedral, $a = 5.617\text{Å}$, $\alpha = 58.7^\circ$	12.16	2.80+0.02i (3.46+0.74i)	24	[001] c	100	This work
Bi _{0.7} Dy _{0.3} FeO ₃ (BDFO/L)	rhombohedral, $a = 5.515\text{Å}$, $\alpha = 59.6^\circ$	11.71	2.57+0.02i (2.85+0.32i)	34	[001] c	237	This work
Bi _{0.6} La _{0.1} Dy _{0.3} FeO ₃ (BLDFO/L)	rhombohedral, $a = 5.493\text{Å}$, $\alpha = 59.7^\circ$	11.65	2.48+0.00i (2.67+0.33i)	32	[001] c	222	This work
Bulk BiFeO ₃	rhombohedral, $a = 5.63\text{Å}$, $\alpha = 59.4^\circ$	12.46	2.8	36.0	[010] r	221	Ref. 99
BiFeO ₃ on SrTiO ₃	rhombohedral, $a = 5.63\text{Å}$, $\alpha = 59.4^\circ$	12.46	2.8	34.2	[010] r	200	Ref. 101
BiFeO ₃ , theory, U=0eV	rhombohedral	12.46	-	-	[010] r	137	Ref. 148
BiFeO ₃ , theory, U=0eV	rhombohedral	12.16	-	-	[001] c	161	Ref. 148
BiFeO ₃ , theory, U=0eV	rhombohedral	11.7	-	-	[001] c	180	Ref. 148
BiFeO ₃ on LaAlO ₃ (T-BFO/L)	tetragonal, $c/a = 1.23$ $c = 4.658\text{Å}$, $a = 3.789\text{Å}$	13.38	2.47	25	[001] r	127	This work
BiFeO ₃ , theory, U=4eV	tetragonal, $c/a = 1.28$ $c = 4.786\text{Å}$, $a = 3.739\text{Å}$	13.38	-	-	[001] r	100	Ref. 153

Table 3.1: Summary of the structural parameters and elastic moduli of BiFeO₃. Here V_0 denotes the volume per atom, the complex refractive index is \tilde{n} , and the acoustic phonon frequency is f . Subscripts R , T and C refer to the rhombohedral, tetragonal and cubic unit vectors.

stants of bulk single crystal BFO and bulk-like BiFeO₃ on SrTiO₃ the along [101]-oriented crystals (rhombohedral [010] direction) [99, 101], and these results are also included in Table 3.1. Conventional ultrasound measurements yielded 127 GPa for polycrystalline BFO [154], substantially lower because of averaging over all crystallographic directions.

First principles calculations of \mathbf{c}^R using DFT (within the GGA+U approach, with various values of the Hubbard constant $U = 0 - 6$ eV) have been reported in Ref. 148, while Ref. 153 discussed similar calculations for \mathbf{c}^T . To compare the theoretical values of \mathbf{c}^R with experiment a conversion was made from the Cartesian coordinate system used in the first-principles calculations [148], which has z' oriented along the three-fold [111] axis, to the experimental geometry with z along the pseudocubic [001] direction. This was achieved using the transformation matrix $\boldsymbol{\alpha}$ and the expression

$$\mathbf{c} = \boldsymbol{\alpha}^{-1} \mathbf{c}' \boldsymbol{\alpha}_T^{-1} \quad (3.9)$$

which is derived in textbooks describing the elastic properties of anisotropic media, e.g. Ref. 149. A similar transformation was performed to allow the elastic constant in the [010]_R direction, as reported in Refs. 99, 101, to be compared to the values of \mathbf{c}^R derived from DFT. Since \mathbf{c}^R and \mathbf{c}^T are functions of the unit cell volume, and larger cells exhibit lower diagonal components c_{ii} in the elastic modulus tensor, the theoretical predictions taken at the same unit cell volume as the determined experiment cell volume were adopted.

Several trends are apparent in the data reported in Table 3.1. Within the rhombohedral phase, smaller unit cell volumes correspond to higher elastic constants. In the experimental tetragonal phase ($c/a = 1.23$) $c_{33} = 160$ GPa is reduced in comparison to the majority of rhombohedral phase results. This is in reasonable accord with DFT calculations [153], which predict a smaller value of $c_{33} = 100$ GPa for a larger $c/a = 1.28$.

3.5 Magnon Resonance

In the pristine rhombohedral phase samples (R-BFO, BDFO, BLDFO) only acoustic modes (below 50 GHz) can be observed, as evidenced by Figure 3.6(b). In contrast, the tetragonal phase sample (T-BFO) exhibits an additional oscillation at a higher frequency, 75 GHz. In this Section this mode is discussed in detail with respect to its structural, magnetic field and temperature dependence. These findings allow the mode to be identified as a magnon originating from the coherent oscillation of weak ferromagnetic order in the multiferroic film. Following the experimental results a discussion of the origin of the magnon mode is given in Sec. 3.5.6.

3.5.1 Magnetic Field Dependence

A static magnetic field $B \leq 0.5$ T was applied in the growth direction. This is sufficient to saturate the weak ferromagnetic magnetisation of these films. For an example of this see Figure 1.3(a) where a magnetic field of ~ 7 kOe was able to saturate the magnetisation of a BDFO film[52]. For both rhombohedral BDFO and BLDFO a mode emerged upon magnetisation similar to that observed for pristine tetragonal BFO, as demonstrated for BLDFO in Figure 3.7. The onset of the magnon mode appears to correlate with the field required to saturate the magnetisation. For a pristine sample of BDFO (i.e. one not previously exposed to a magnetic field) the 75 GHz mode appeared at $B > 0.45$ T, while for BLDFO, $B > 0.3$ T was sufficient to produce this mode. This is in agreement with the slightly lower saturation field of BLDFO (~ 0.36 T) compared to BDFO (~ 0.64 T) [47]. The mode can be identified as originating from a weak permanent magnetic moment, as after the removal of the magnetic field the mode remains present (bottom curve in Figure 3.7), and appears to persist indefinitely.

For a magnon in a simple antiferromagnet or ferromagnet an increase in frequency with applied magnetic field would be expected [155]. No shift in the frequency of the

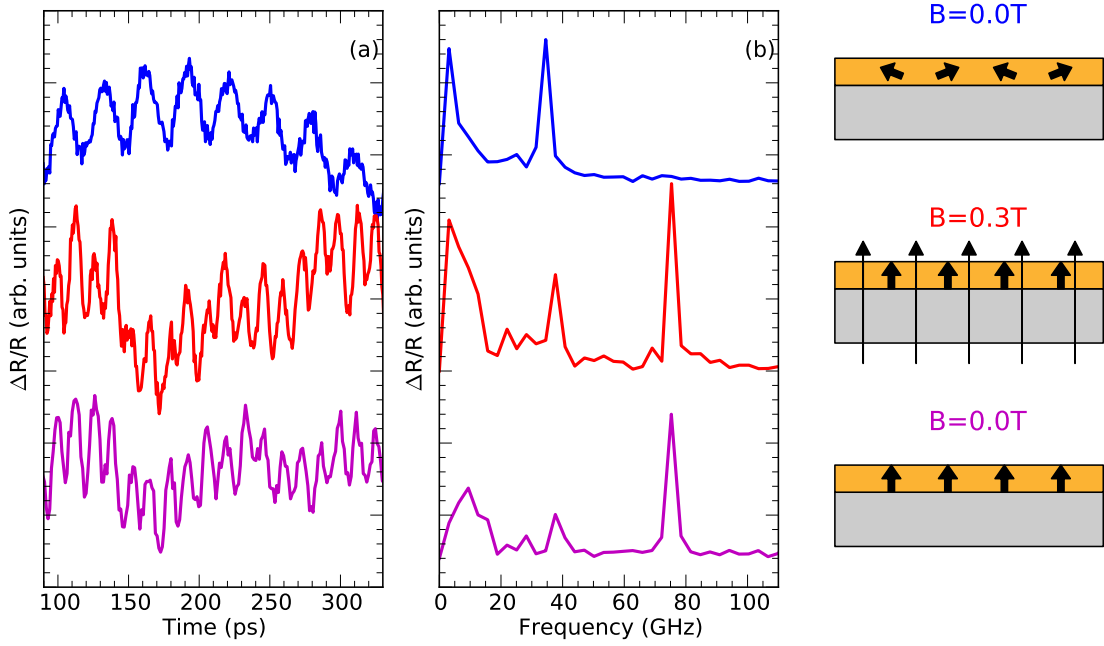


Figure 3.7: Influence of a magnetic field on ΔR spectra for BLDFO (323 nm thick) on LaAlO_3 in the (a) time and (b) frequency domains. Here, the time-domain data was taken over the range from 15-332 ps, during which the acoustic pulse entered the film first and then the substrate. For a pristine sample (top/blue line), not previously exposed to a magnetic field, only acoustic phonon oscillations are evident. Under a magnetic field $B = 0.3$ T in the growth direction an additional oscillation at 75 GHz can be witnessed (middle/red line), which is assigned to a magnon mode. After the removal of the magnetic field (bottom/purple line) the magnon resonance remains. The diagrams (right) indicate the magnetic domain structure at each stage.

magnon mode was observed with magnetic field in the range examined ($B \leq 0.5$ T). This may be a consequence of the relatively weak magnetic field applied in comparison to the large values (20 T) required to suppress the spin cycloid of BFO [26]. Coherent magnons in the multiferroic $\text{Ba}_{0.6}\text{Sr}_{1.4}\text{Zn}_2\text{Fe}_{12}\text{O}_{22}$ also do not change in frequency under similar applied fields [88].

3.5.2 Temperature Dependence

The temperature dependence of the 75 GHz magnon mode was also examined. Figure 3.8 presents the time-resolved reflectivity spectra for the T-BFO phase (where the

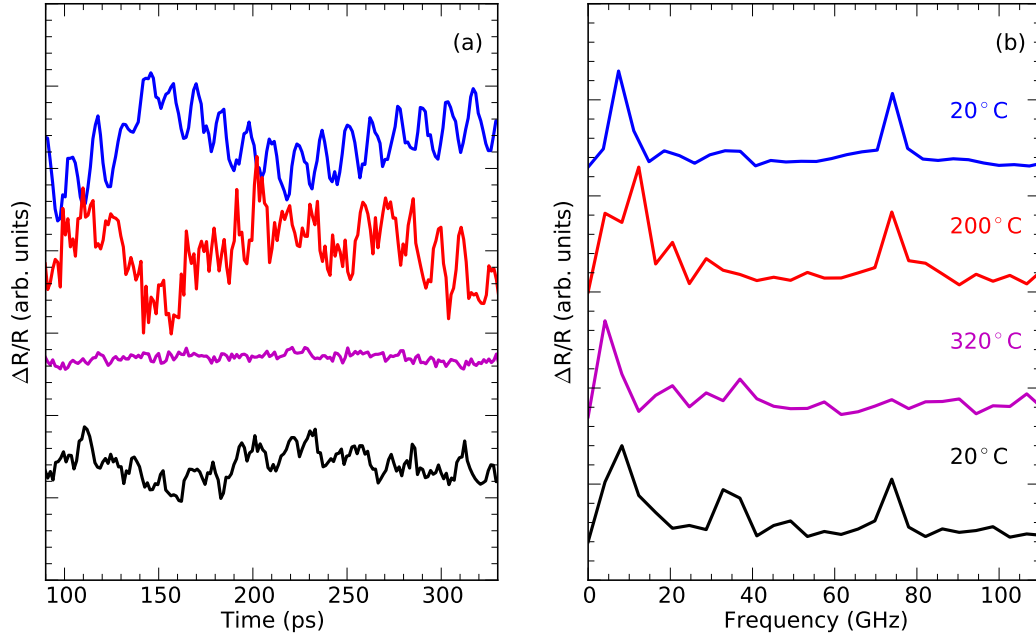


Figure 3.8: ΔR spectra in the (a) time and (b) frequency domains for T-BFO at sample temperatures (from top to bottom) of 20°C (blue), 200°C (red), 320°C (purple), and on subsequent cooling to 20°C (black). The 75 GHz mode disappears as the temperature approaches the Néel temperature, and reappears upon cooling. The time-domain data were windowed from 90-340 ps (acoustic pulse in substrate).

75 GHz mode is intrinsic) for 20°C, 200°C, 320°C and after being returned to 20°C. Both the amplitude and the frequency of the magnon modes of simple ferromagnets and antiferromagnets are highly temperature dependent, with the intensity of the mode being expected to drop to zero as the Néel temperature (T_N) is approached. By 200°C the magnitude of the 75 GHz mode has reduced in comparison to that at 20°C, while at 320°C the mode is no longer discernible. This latter temperature is 50°C below the $T_N=643\text{ K}$ (370°C) for bulk BiFeO_3 , indicating that the magnon is linked to the antiferromagnetic sub-lattice order, from which the weak ferromagnetic component arises via the DM interaction.

3.5.3 Wavelength Dependence

As discussed in Section 3.4.1, the observed frequency for a phonon mode measured by time-resolved reflectivity would be expected to display a $1/\lambda$ dependence as given by Equation 2.3. The wavelength dependence of the modes were therefore investigated using spectrally narrowed probe beams around 810 nm and 785 nm (spectra shown in the inset of Figure 3.9). Over this probe range n and does not vary significantly (see Figure 3.4). As such, considering that $2nv \sim \text{constant}$, the expected fractional change in the frequency of a phonon mode is given by:

$$\frac{\Delta f}{f} \sim \frac{\Delta \lambda}{\lambda} \quad (3.10)$$

This results in an expected a shift of $\sim 3\%$, corresponding to $\Delta f \sim 1.1$ GHz for a phonon mode at 37.5 GHz and $\Delta f \sim 2.25$ GHz for modes at 75 GHz.

Figure 3.9 shows the frequency spectra for magnetised BLDFO/L with probe beam wavelengths of 810 nm and 785 nm. The time-window for the data is 323 ps which results in a resolution in the frequency domain of ~ 3 GHz. The mode peaks are approximately twice as wide as this. As such a dual-gaussian fit of the form;

$$\frac{\Delta R}{R} = a \exp\left(\frac{-(f - b)^2}{2c^2}\right) + A \exp\left(\frac{-(f - B)^2}{2C^2}\right) + d \quad (3.11)$$

was used to extract a better value for the central frequencies of the modes. The fits are the solid lines in Figure 3.9. For the lower frequency mode this yields $f(810\text{nm})=37.3$ GHz and $f(785\text{nm})=37.8$ GHz, which is a shift of $\Delta f=0.5$ GHz in the expected direction for the substrate acoustic mode. No shift in the high frequency mode can be observed. These observations hold with the differing assignments of a phonon mode for the lower energy mode and a magnon for the higher energy mode.

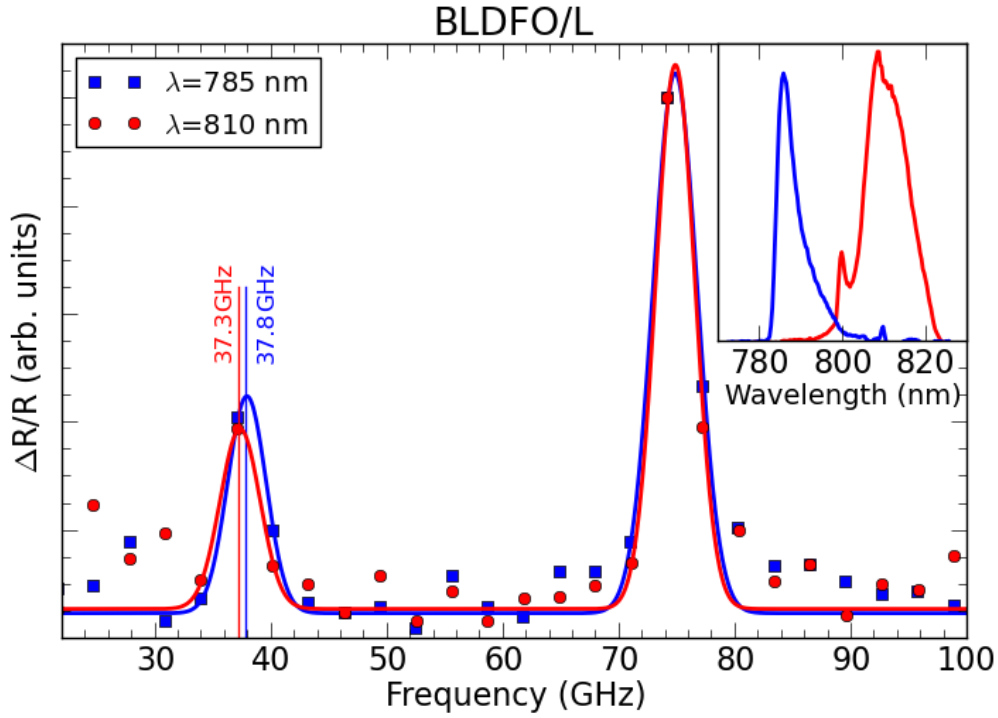


Figure 3.9: Probe wavelength dependence: Frequency domain spectrum for 10-111ps time window on magnetised BLDFO/L for probe wavelengths of $\lambda=785$ nm (Blue squares) and $\lambda=810$ nm (Red circles). Solid lines show bi-gaussian fits to the data points. The inset shows the spectra of the probes.

3.5.4 Influence of Substrate

Pump probe reflectivity measurements were carried out on samples on MgO substrates as well as on LaAlO_3 . The extracted time domain oscillations for magnetised BDFO/L and BDFO/M can be seen in Figure 3.10. Again the frequency domain analysis has been split into early and late times where the acoustic phonon would be expected to be in the film or to have propagated into the substrate respectively. Both samples share an early time mode at similar frequencies to those observed for the same films on LaAlO_3 substrates (See Section 3.4.1, Table 3.1 and Figure 3.6). This is unsurprising as the phonon mode frequency will be dominated by the film properties rather than the substrate mismatch. In contrast the higher frequency mode present at late times

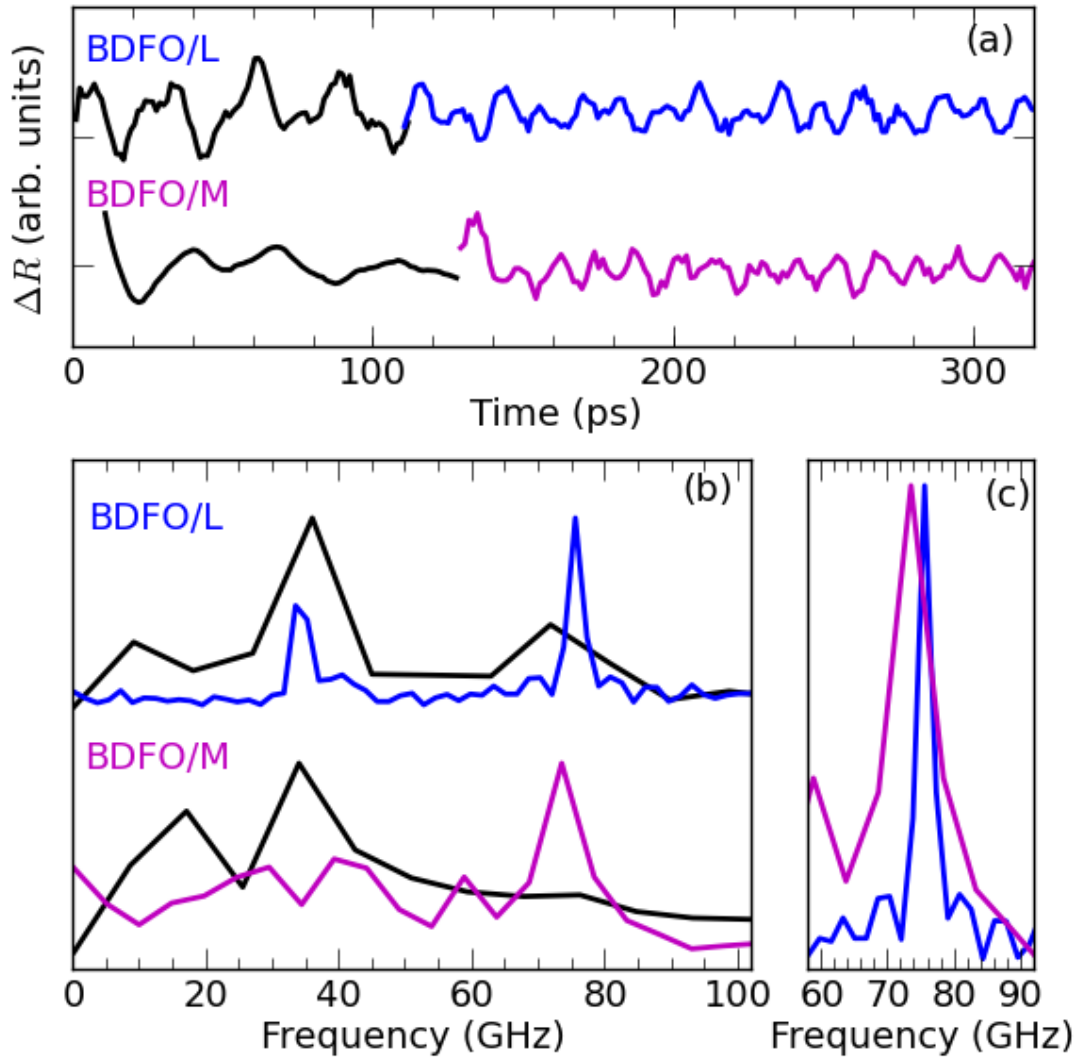


Figure 3.10: Coherent oscillations in the time-resolved reflectivity of BDFO on LaAlO_3 (BDFO/L, blue) and MgO (BDFO/M, purple) are shown in the (a) time and (b/c) frequency domains. Spectra are shown normalized to their maximum values. At early times (black) the acoustic phonon pulse is within the film. (c) highlights the frequency shift for the higher energy mode.

show a shift between the LaAlO_3 and MgO substrate. Measurements of BLDFO/M (not shown) also showed a shift of the peak to the same position as for BDFO/M. LaAlO_3 and MgO have different in-plane lattice constants ($a=3.789\text{\AA}$ and $a=4.212\text{\AA}$ respectively, see Section 3.2.1) and thus will have different Fe-Fe spacings. As the Fe sites are responsible for the magnetic moment it is probable that the magnon energy is dependent on this spacing.

3.5.5 Magnon Mode Evolution and Pump Fluence

For the 75 GHz mode, a slight time-dependence of the central frequency was observed. A small shift in frequency between times shortly after excitation and later times appears to be present. An example of this phenomenon can be seen in figures 3.11(a) and (b) for magnetised BLDFO/L. Two 90 ps time-windows (i) shortly after photoexcitation (red) and (ii) at a later time (blue) are compared. Analysis over four oscillation periods in the time domain and Gaussian fits in the frequency domain show a small blue-shift for the later-time compared to early time oscillations. As the pump-probe data was only acquired up to ~ 300 ps, and increasing the time window would lead to prohibitively long data acquisition times, investigation into whether the mode has a time evolution was limited. An attempt to better resolve this was carried out using asynchronous optical sampling (ASOPS) measurements, where rapid acquisition of time delays of up to 1 ns is possible, were carried out at the University of Konstanz.

For the ASOPS study, the fundamental beam (800 nm or 1.55 eV) of two 50 fs laser oscillators with repetition rates of 800 MHz and $(800+\Delta)$ MHz, with $\Delta=5$ kHz were used to pump and probe the transient reflectivity over a time-window of ~ 1 ns. The pump beam was frequency doubled to 400 nm (3.1 eV) using a $500\ \mu\text{m}$ BIBO (BiB_3O_6 , optimised for 200 fs, which is closer to the pulse duration at the sample due to dispersion in the optics) to photoexcite the multiferroic films at a fluence of $8.5\ \text{nJcm}^{-2}$. The probe was incident on the sample at normal incidence (i.e. along [001] in the pseudocubic representation, see Figure 3.1). The absorption depth of

the samples at the pump and probe wavelengths are $\delta(400\text{ nm}) = 40 - 100\text{ nm}$ and $\delta(800\text{ nm}) = 1.5\text{ }\mu\text{m}$. The ratio of the pump to probe power at the sample was 30 mW to 7.4 mW. For further details on ASOPS see Section 2.1.1 in Chapter 2.

Figures 3.11(c) and (d) show the results of an ASOPS measurement in the time and frequency domain on BDFO/L. This clearly shows the phonon mode in the LAO substrate at 33 GHz; there is however no evidence of the higher frequency mode at $\sim 75\text{ GHz}$. This was also the case for ASOPS measurements of BFO-T. The most apparent difference between this and the previous transient reflectivity measurements is the in the magnitude of the pump fluence. For the previous measurement, where the $\sim 75\text{ GHz}$ mode was observed, the pump fluence was $\sim 60\text{ }\mu\text{Jcm}^{-2}$ while for the ASOPS measurements a significantly reduced fluence of $\sim 8.5\text{ nJcm}^{-2}$ was used. This difference arises primarily from the $200\times$ difference in the laser repetition rates; 4 MHz for the previous pump-probe studies and 800 MHz for ASOPS. The absence of the $\sim 75\text{ GHz}$ mode suggests that the pump fluence is critical in order for it to be excited. Unfortunately, given the absence of the mode in the ASOPS studies, no further clarification was reached on any possible time-dependent behaviour, of the mode. Another notable feature of the $\sim 75\text{ GHz}$ mode is its presence throughout the entire time-windows examined. This persistence rules out an acoustic mode, as discussed in Section 3.4.

3.5.6 Magnon Resonance: Discussion

The coherent magnon mode was observed for both tetragonal phase BFO and Dy-doped BFO, and cannot therefore arise from the precession of Dy moments. Rather, the Fe sites must provide the relevant magnetic sub-lattices. A possible microscopic mechanism for the observed ultrafast stimulation of the magnetic permeability μ is as follows: UV photoexcitation transfers an electron from an oxygen $2p$ orbital to an iron $3d$ state (Figure 3.4), altering the electronic configuration from high-spin $3d^5$ (Fe^{3+}) to the low-spin $3d^6$ (Fe^{2+}) state. This transient change in μ then alters the

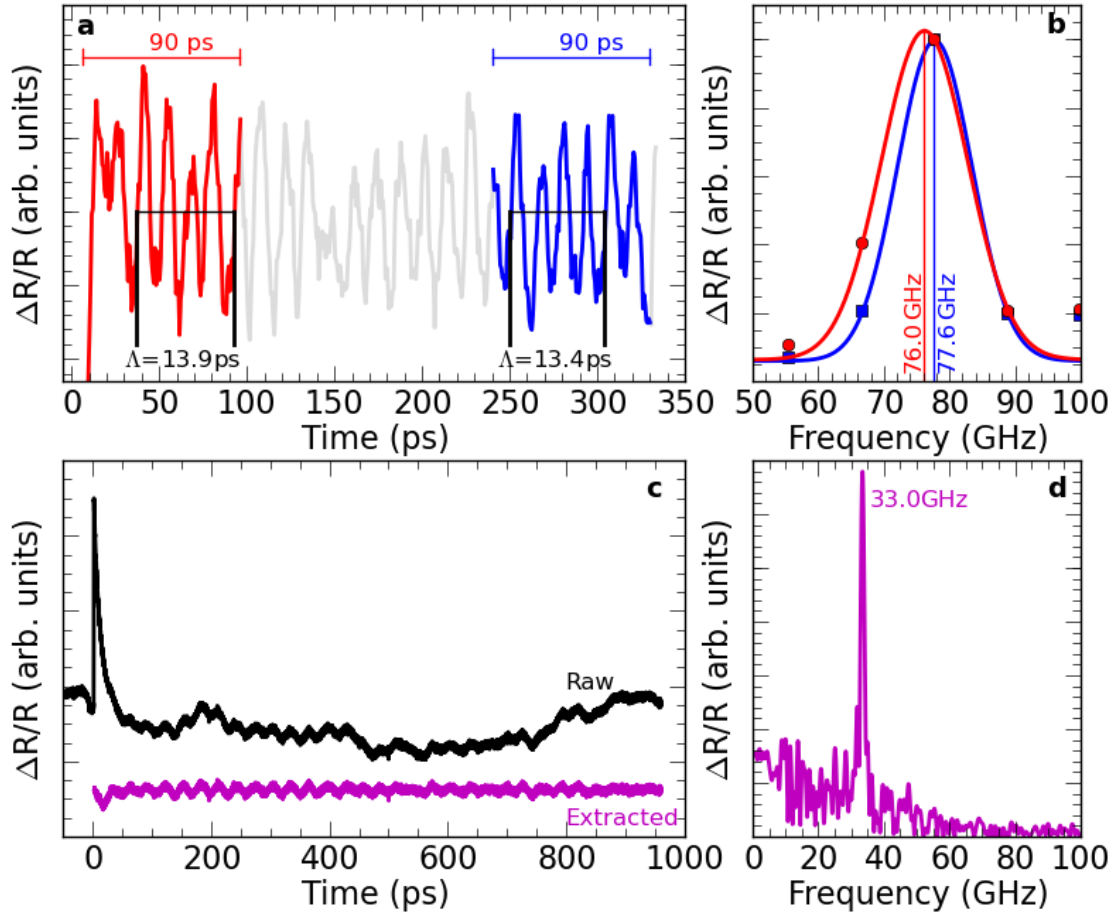


Figure 3.11: (a) Coherent oscillations in the time-resolved reflectivity of magnetised BLDFO/L are shown in the time domain data (circles/squares) and gaussian fits (solid lines). The red and blue section highlight 90 ps windows soon after excitation and at later time respectively. (b) Shows the frequency domain for these windows. (c) ASOPS on magnetised BDFO/L in the time domain, showing the raw data (black) and extracted oscillations (black). (d) Shows the frequency domain for the extracted oscillations.

reflectivity.

Interestingly, while the magnon is present intrinsically in the tetragonal phase sample, magnetisation was required to create the mode in the rhombohedral phase rare-earth doped films. This suggests that the break in symmetry along the growth direction introduced by the tetragonal distortion produces a similar effect as the application of a low magnetic field. The magnon frequency is comparable for both T-BFO and rare earth doped R-BFO, which may be a result of their similar in-plane lattice constants, and indicates a similar magnetic structure. Furthermore, the substrate used appears to have an influence on the magnon frequency. A study of the magnetic domains of the weak ferromagnetic moment, for instance using magnetic force microscopy, is necessary to further investigate whether the tetragonal distortion can result in a spontaneous local moment. The size of the magnetic domains is also highly relevant: to observe a coherent magnon signal the domain size must be larger than the spot size of the infrared probe ($\sim 10 \mu\text{m}$).

In contrast to the single magnon mode reported herein, a sequence of magnon modes separated by 7.5 cm^{-1} (225 GHz) is seen in inelastic (Raman) scattering on bulk BFO [87]. No magnons have been reported in unmagnetised bulk R-BFO and thin film R-BFO with time-resolved reflectivity spectroscopy [99, 101]. Note that a magnon at 46 GHz reported previously [156] in thin film BFO actually corresponds to the acoustic phonon mode of the SrTiO_3 substrate.¹ In comparison to the magnon-induced ΔR oscillations in a hexaferrite [88] at 40 GHz (0.17 meV), the magnons reported herein for T-BFO and BLDFO are long lived (lifetime above 1 ns), and are observed above room temperature.

In thin film rhombohedral BFO, the magnon response was investigated theoretically by solving the Landau-Lifshitz equations for two antiferromagnetic sublattices coupled by the DM interaction [157]. For thin film BFO two modes at ~ 1.3 GHz and

¹The LA-phonon speed of 7900 ms^{-1} reported in Brivio et al. [127], and a refractive index $n = 2.34$ at 800 nm results in a acoustic phonon frequency of 46 GHz, as reported in Chen et al. [156]

8 GHz were predicted, with the high frequency mode (where sublattices oscillate out of phase) corresponding to the DM interaction strength D_{ij} [157]. While these modes are below our experimental resolution, an enhanced DM interaction may increase the frequency of these magnon modes, creating the 75 GHz magnon-induced ΔR oscillation. The predicted anisotropy of the magnon dispersion may be used to discriminate between the two predicted modes [157]. The low frequency mode is more anisotropic, whereas no change in the frequency of the magnon in T-BFO or BDFO was seen on rotating the sample about the surface normal. This suggests that the magnon reported here corresponds to the more isotropic out-of-phase mode [157]. The observed mode at 75 GHz corresponds to a DM interaction strength $D_{ij} = 0.31$ meV. This is enhanced in comparison to the value of $D_{ij} = 0.16$ meV recently reported for bulk rhombohedral BFO [158].

3.6 Conclusions

In conclusion, the dynamics of coherent magnons and acoustic phonons in multiferroic thin films of tetragonal and rare-earth doped BiFeO₃ were investigated using time-resolved reflectivity. Oscillations in the reflectivity were attributed to dynamic modulations of the refractive index by acoustic phonons and magnons. The creation of a magnon mode after magnetisation or using tetragonal BiFeO₃ provide promising routes to create a magnetoelectric multiferroic with a tailored magnonic response. Based on the temperature and magnetic field dependence the magnon resonance was assigned to a ferromagnetic moment linked to antiferromagnetic order by the Dzyaloshinskii-Moriya interaction. In addition, it was demonstrated that the ultra-fast photoacoustic technique utilized in this work allows direct experimental access to the elastic moduli of ferroic thin films, which are often hard to characterize using traditional transducer-based methods.

Chapter 4

Structural, optical and vibrational properties of self-assembled $\text{Pb}_{n+1}(\text{Ti}_{1-x}\text{Fe}_x)_n\text{O}_{3n+1}$ Ruddlesden-Popper superstructures

4.1 Introduction

In this chapter a study of the structural, optical and vibrational properties of compressively strained thin films of the Ruddlesden-Popper phase $\text{Pb}_{n+1}(\text{Ti}_{0.67}\text{Fe}_{0.33})_n\text{O}_{3n+1-\delta}$ grown on LaAlO_3 substrates is reported. A structural characterization via X-ray diffraction and transmission electron microscopy (TEM) demonstrate the spontaneous formation of a Ruddlesden-Popper superstructure where the number of repeating ABO_3 layers is $n \simeq 8$, with a modulated density in the growth direction. X-ray photoelectron spectroscopy (XPS) was used to determine the films' stoichiometry and chemical environments. Simultaneous Raman and infrared activity of phonon modes, along with the observation of second harmonic generation identify a polar point group compatible with ferroelectricity. The dielectric function in the range from the far-infrared to the UV was extracted using THz time-domain spectroscopy, Fourier transform infrared (FTIR) spectroscopy and UV-visible ellipsometry.

Oxides with the ABO_3 perovskite structure are remarkably capable at accommo-

dating defects, owing to their high dielectric constants and structural stability. While a small deviation from the 1:1:3 stoichiometric ratio produces point defects, larger deviations can lead to extended (planar) defect formation. Non-conservative crystallographic shear planes can account for oxygen deficiency[159, 160] in $A_nB_nO_{3n-2}$, while the Ruddlesden-Popper (RP) homologous series $A_{n+1}B_nO_{3n+1}$ has extra AO planes[161]. Along the z -direction the unit cell of the RP phase consists of n ABO_3 layers, then a planar stacking fault $[a/2, b/2, d]$ (where $d \simeq c/2$), followed another n ABO_3 layers and a second stacking fault, as illustrated in Figure 4.1. The epitaxial growth of strained RP phases can result in novel phases where n can be used to tune functional properties. For instance, ferroelectricity in the RP series $Sr_{n+1}Ti_nO_{3n+1}$, of which the end member (STO) is an incipient ferroelectric, has been reported to occur only if $n \geq 4$ and under tensile biaxial strain[162].

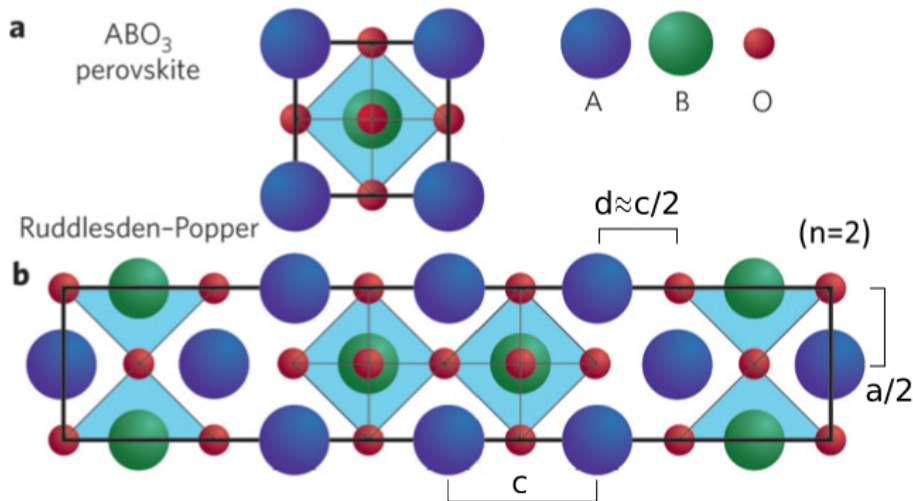


Figure 4.1: (a) ABO_3 Perovskite structure. (b) Ruddlesden-Popper structure for $n=2$. The planar stacking fault looks locally like half a rock-salt unit cell. [Adapted from [163]]

4.2 Structure and composition

4.2.1 Sample Growth

Thin films of PTFO with nominal thicknesses of 100 nm, 200 nm and 300 nm (labelled as PTFO-100, -200 and -300) were deposited on (001) $LaAlO_3$ (LAO) by pulsed laser

deposition by V.R. Palkar’s group at the Tata Institute of Fundamental Research, Mumbai. Target compositions were $\text{PbTi}_{1-x}\text{Fe}_x\text{O}_3$ with $x = 0.5$. A laser fluence and frequency of 2 J/cm^2 and 10 Hz , an oxygen pressure of 0.5 mbar , a substrate temperature of $625\text{ }^\circ\text{C}$, and a substrate-target distance of 5 cm were employed. The deposition time was varied to obtain films with different thickness.

4.2.2 Transmission Electron Microscopy

Conventional transmission electron microscopy (TEM) and annular dark-field scanning transmission electron microscopy (ADF-STEM) images of the atomic structure of the PTFO-100 film can be seen in Figure 4.2. Aberration-corrected TEM was performed using a JEOL 2000FX system equipped with energy-dispersive X-ray (EDX) and electron energy loss spectroscopy (EELS) capabilities.

Figure 4.2(a) shows a low-magnification conventional TEM image of PTFO-100. This reveals a dark and bright wave-like layer structure with a periodicity of 4 nm in the growth direction. The ADF images, Figures 4.2 (b) and (c), show the Pb atomic columns; the Ti atoms give weaker contrast. It can be seen that the ‘waves’ arise from two differently ordered regions; one that looks like a perovskite-like structure (regions 1 and 1’) and a second that looks like a rock-salt-like structure (region 2). For region 1 the solid vertical white lines mark the perovskite A-site (Pb atoms) while the dashed white lines mark the B-site (Ti atoms). It can be seen that for region 1’ the Pb atoms are instead found along the dashed vertical white lines. On either side of the rock-salt-like region 2 the A- and B- cation sites are switched. EELS spectra taken in areas 1, 2 and 1’ showed no difference in elemental composition, implying that the different regions have similar stoichiometry.

Figure 4.3(c) shows Fe edge EELS spectra for regions 1, 1’ and 2. There is no clear shift in the peak positions across the interface between the perovskite-like and rock-salt-like areas; furthermore the ratio of the peaks is constant. EDX analysis of the different regions also did not show a clear difference in composition although

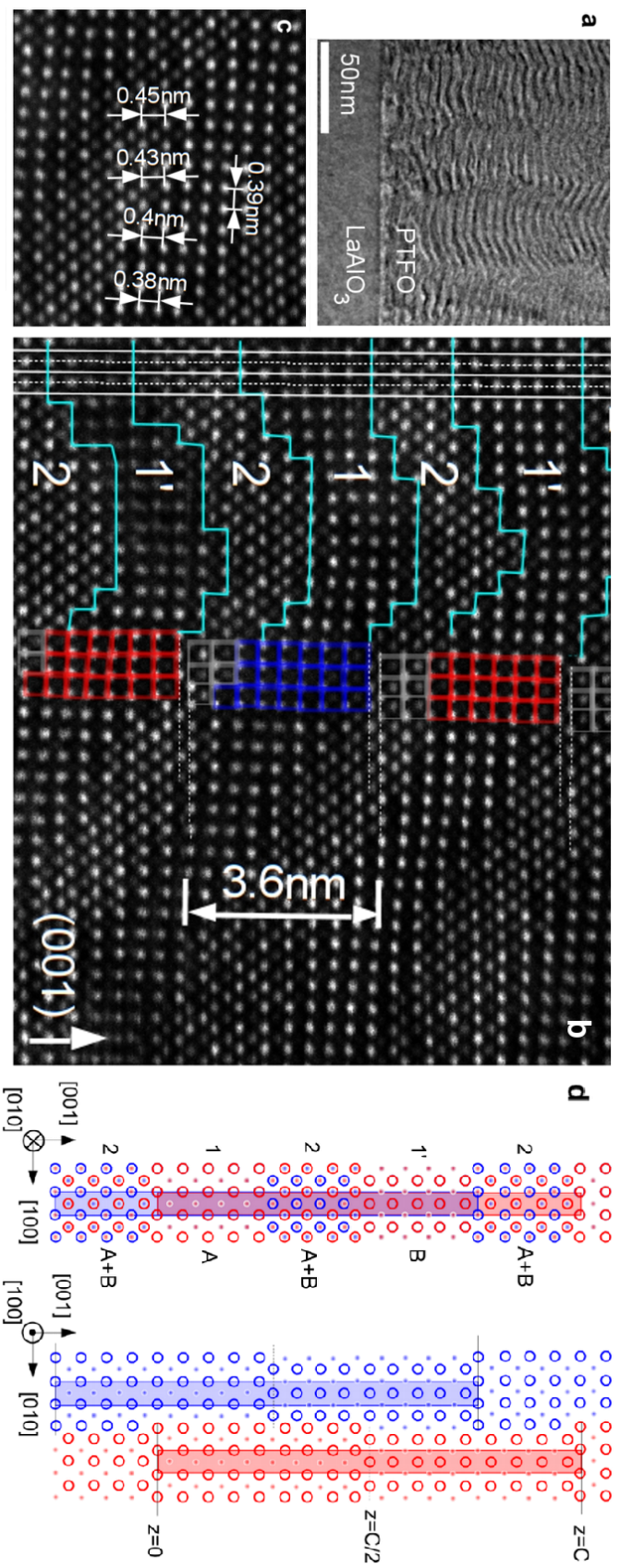


Figure 4.2: Transmission electron microscopy of 100 nm PTFO film. (a) Conventional TEM showing ‘wave’ patterns. (b) ADF-STEM image showing that ‘waves’ consist of perovskite-like areas (labelled 1 and 1’, blue and red squares) and a rock-salt-like areas (labelled 2, grey squares). Cyan lines mark the boundaries between these regions. The vertical white solid lines run through the perovskite A site in area 1, becoming the B site in area 1’. The horizontal white dashed lines show atomic planes separated by a stacking fault with $d \simeq 0.2$ nm. (c) ADF-STEM image showing a change in region 1 and 1’. (d) Schematic of structure in (010) plane (left, corresponding to plane of TEM image) and (100) plane (right). A Ruddlesden-Popper unit cell for $n = 8$ is shaded in blue, while another, offset by an antiphase boundary (see text), is shaded in red. Projection of the right-hand cartoon along [010] yields the left-hand schematic, creating areas where Pb ions appear to be on both the A and B sites. [J.J.P. Peters R. Beauland and A.M. Sanchez undertook the TEM study.]

some islands were observed near the interface with the substrate. Figure 4.3(a) shows analysis of one of these islands. The EDX maps show a deficiency in the Pb and an increase in the Fe in these areas. This can be seen clearly from the EDX line profile for Fe and Pb in Figure 4.3(b).

The structure can be understood as consisting of a Ruddlesden-Popper phase with $n \simeq 8$ in the [001] growth direction. The schematic in Figure 4.2(d) can be used to better understand this. The two schematics show different projections of the Pb ion positions; the left hand diagram corresponds to the sample in the (010) plane of the TEM images and the right hand diagram corresponds to the (100) plane. The blue and red boxes show two unit cells with dimensions a, a, C where the red atoms are off-set from the blue by $C/2$ in the [001] direction. In the (010) TEM imaging plane it can be seen that this structure leads to Pb ions appearing to be present on both the A- and B-sites. This gives the appearance of a rock-salt-like structure as observed in the TEM images. Since these images are a projection of the three-dimensional structure it is not possible to distinguish between (a) a sharp rock-salt-like planar fault, lying on a plane inclined to the electron beam and (b) a diffuse fault with an extended rock-salt structure.

4.2.3 XPS

An Omicron XM1000 monochromated Al K_{α} x-ray source was used to illuminate the sample, with photoelectrons collected in an Omicron SPHERA analyser using an estimated sampling radius of 1.1 mm. Due to the insulating nature of the samples, an Omicron CN10 charge neutraliser was used to prevent surface charging. All binding energies were referenced to the C 1s peak from atmospheric contamination at 284.6 eV. All data were analysed using the CasaXPS package, with compositional analysis facilitated via determination of the analyser transmission function, calculated using polycrystalline Ag, Au and Cu foils.

X-ray photoelectron spectroscopy (XPS) analysis on the PTFO films found two

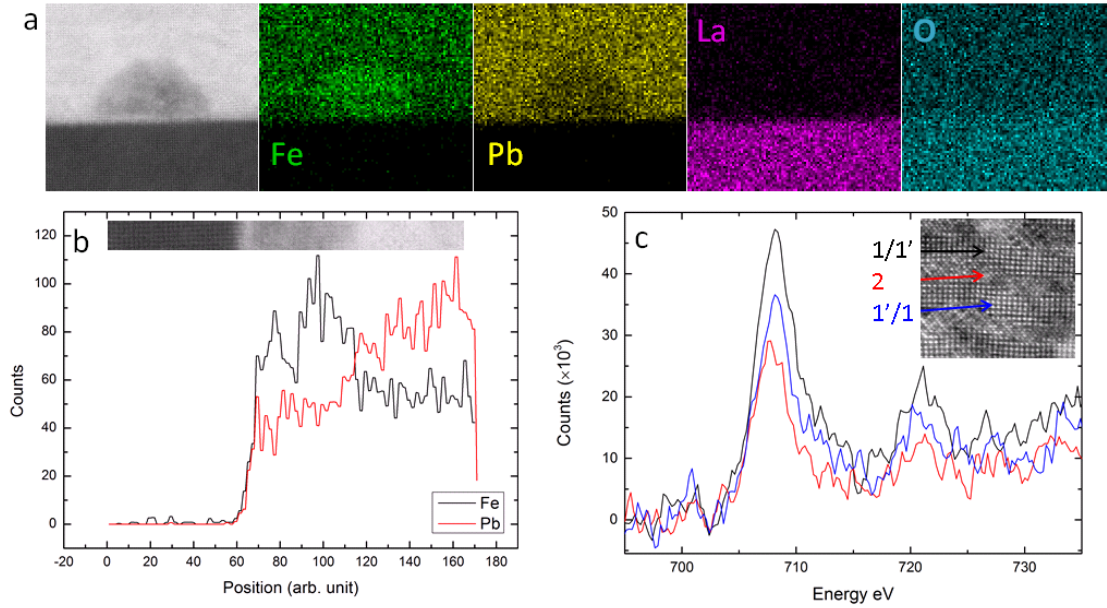


Figure 4.3: EDX and EELS for PTFO-300: (a) EDX analysis for different components. (b) EDX line profile through feature at substrate-film interface. (c) EELS spectra taken at areas 1, 1' and 2 of the sample. [EDX and EELS measurements were performed by J.J.P. Peters, R.Beanland & A. Sanchez]

contributions to the Pb $4f$ peaks. One component had a binding energy consistent with PbTiO_3 , and another (0.5 eV lower binding energy) indicated a Pb-O local environment. This latter contribution may arise from one or more of the following: the extra PbO layer in the RP structure, out-of-phase boundaries, and possible surface oxides. The Ti $2p$ spectra exhibited a single binding energy comparable to that of PbTiO_3 . The B-site occupancy was obtained from XPS intensities for the Ti $2p$ and Fe $2p$ peaks, which were in a 2:1 ratio, corresponding to $x = 0.33$. At and above this level the tetragonal unit cell of bulk PTFO may distort due to FeO_6 octahedral tilts,[68] and the tetragonality c/a is reduced. The XPS and EELS spectra were consistent with Fe^{+2} ions. In pure PbTiO_3 rather than Ti^{+4} and O^{-2} the ionic valences are Pb^{+2} , $\text{Ti}^{+2.89}$ and $\text{O}^{-1.63}$ owing to Ti-O hybridisation. [67] This reduction in the B-site valence may explain the observation of +2 valence Fe ions (rather than +3) in the XPS and EELS analysis.

The A:B:O ratio from XPS was approximately 1:1:3, when the contributions to Pb 4f from the Pb-O environment and from surface oxygen were discluded. This is consistent with the RP phase in the limit of large n , when the RP phase tends to the ABO_3 perovskite structure. Local EDX spectra yielded a different A:B:O ratio of 7:4:14. In contrast to the XPS analysis, the two Pb environments (see above) were not resolved in EDX, and a surface oxygen contamination was not considered. These factors lead to an excess of Pb and O in the EDX A:B:O ratio. Assuming ionic valences[67] of Pb^{2+} , $\text{Ti}^{2.89+}$ and $\text{O}^{-1.63}$ and taking the XPS atomic ratios (for the reasons outlined above), charge balance requires $\delta = 1$ when $n = 8$ for $\text{Pb}_{n+1}(\text{Ti}_{0.67}\text{Fe}_{0.33})_n\text{O}_{3n+1-\delta}$. Oxygen vacancies and/or non-conservative out-of-plane boundaries both create an oxygen deficiency.

[J.J.P.Peters R.Beanland and A.M.Sanchez undertook the TEM study. M.Walker and C.F.McConville performed and analysed the XPS results.]

4.2.4 X-Ray

A four-circle x-ray diffractometer (PANalytical Xpert Pro MRD) with a Cu source and a 4-bounce hybrid monochromator was used to give pure $\text{K}\alpha_1$ radiation ($\lambda=1.540598 \text{ \AA}$). A Pixcel detector was used in scanning mode to collect the $2\theta - \omega$ diffraction scans. Reciprocal space maps were also collected in scanning mode as a collection of $2\theta - \omega$ scans, which were then converted into reciprocal space.

$2\theta - \omega$ X-ray Diffraction

High-resolution $2\theta - \omega$ X-ray diffraction scans were taken to examine the crystal structure of the films. In Figure 4.4(a) the pseudocubic (002) peak of the LAO substrate (space group $\text{R}\bar{3}\text{c}$, $a=3.789 \text{ \AA}$, $\alpha=90.12^\circ$)[152] is visible at $2\theta=48^\circ$. For each film a sequence of diffraction peaks at lower 2θ (larger c) than the substrate peak is evident. The wider range $2\theta - \omega$ scan in Figure 4.4(b) indicates diffraction peaks up to the substrate's (004) peak for the PTFO-100 sample. While the (002) peaks

of the film are at lower 2θ than the (002) peak of LAO, those for (001) straddle the substrate peak (23.5°) with one of the four at a higher angle. The data resemble the diffraction pattern of a superlattice owing to their regular spacing in 2θ .

The position of each film's diffraction peaks can be assigned to the Bragg and superstructure peaks as follows. The * symbols in Figure 4.4(b) denote the calculated Bragg angles for the PTFO-100 film assuming the perovskite cell has $c = 4.437 \text{ \AA}$. The adjacent satellite peaks are at angles consistent with a superlattice period $\Lambda = 35.8 \text{ \AA}$ as determined using[164]:

$$\Lambda = \frac{(m - n)\lambda}{2(\sin \theta_m + \sin \theta_n)} \quad (4.1)$$

where $\lambda = 1.540598 \text{ \AA}$ is the X-ray wavelength and θ_m and θ_n are the angular positions of adjacent satellite peaks, with orders m and n [165]. Table 4.1 lists c and Λ for the PTFO films assuming that $m - n = 1$. This results in $\Lambda \simeq 36 \text{ \AA}$, which is half the c unit cell dimension of the RP phase observed in TEM. The dashed line in Figure 4.4(a) is a model calculation of the X-ray diffraction pattern of an RP phase on LAO (including Pb and La atoms only), assuming that $n = 8$, $c = 4.43 \text{ \AA}$ and that the stacking fault had $d = 0.12 \text{ \AA}$. The model does not include disorder (such as variations in c or n), and hence has narrower diffraction peaks than observed experimentally.

For PTFO powder samples a single perovskite phase is retained only for Fe fractions $x \leq 0.3$, while $x > 0.3$ exhibits secondary phases visible as additional XRD peaks, and consisting mainly of $\text{PbFe}_{12}\text{O}_{19}$ [68]. For the samples studied here, the extra peaks visible in the XRD $\omega - 2\theta$ scans arise from the RP superstructure, and no evidence of such secondary phases was observed via XRD or TEM.

To examine whether epitaxial strain or the oxygen-rich growth conditions are responsible for the formation of the RP phase it would be desirable to examine films grown on different substrates. The deposition rate and substrate temperature can have a strong influence on the superlattice period, as reported for RP phases of barium stannate[166]. Crystallographic shear planes that lower oxygen content exhibit wave-

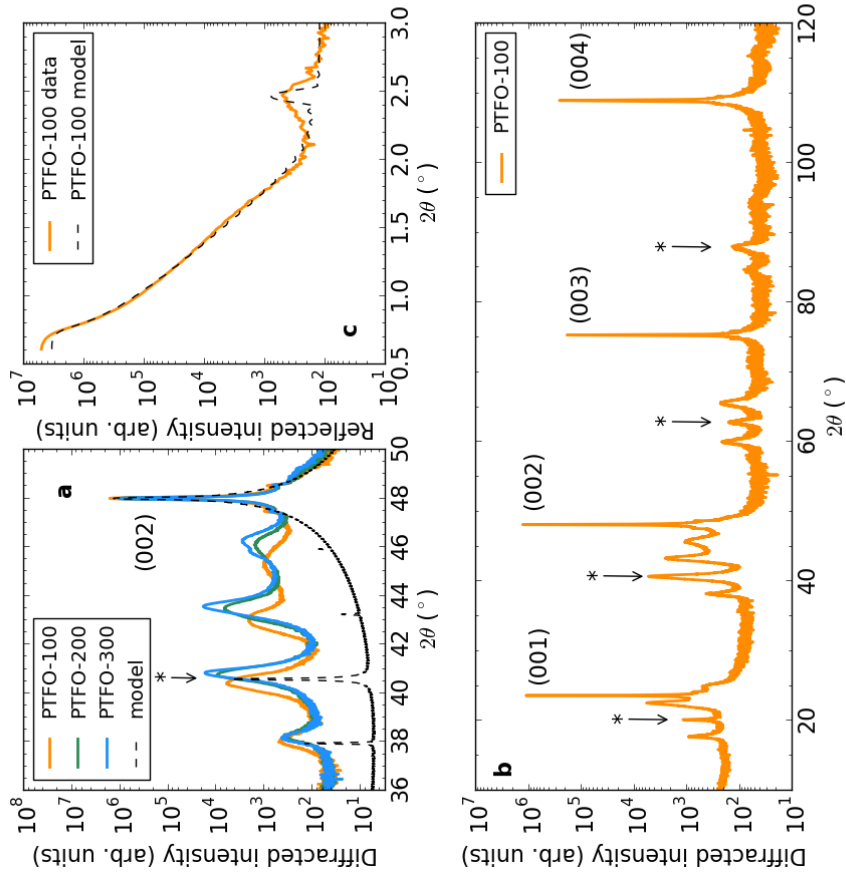


Figure 4.4: X-ray characterisation of $\text{Pb}_{n+1}(\text{Ti}_{0.67}\text{Fe}_{0.33})_n\text{O}_{3n+1-\delta}$ films: (a) 2θ scans around (002) substrate peak for PTFO-100, -200 and -300 films (solid lines). The asterisk marks the Bragg peak for $c \simeq 4.4 \text{ \AA}$. The dashed line is the model described in the text. (b) Wide angle 2θ scan for PTFO-100. (c) Shallow angle x-ray reflectivity for PTFO-100 from experiment (solid line) and simulation (dashed line). (d) A symmetric $2\theta - \omega$ scan for PTFO-100 around the (003) substrate peak, at $\phi = 0$. (e) and (f) are reciprocal space maps for PTFO-100 around the (103) and (113) LAO substrate peaks (indicated by the dashed lines), respectively. q_x , q_{\parallel} and q_z denote the scattering wavevectors in the [100], [110] and [001] directions of the substrate. [*J. Lloyd-Hughes took the shallow angle X-ray data (b), reciprocal space maps (c) and produced the model in (a) and (b).*]

XRD			
	a (Å)	c (Å)	Λ (Å)
PTFO-100	3.90±0.02	4.437±0.009	35.8±1.4
PTFO-200	3.90±0.02	4.425±0.005	36.1±0.8
PTFO-300	3.90±0.02	4.414±0.005	35.6±0.8

Table 4.1: Summary of crystal structure of $\text{Pb}_{n+1}(\text{Ti}_{0.67}\text{Fe}_{0.33})_n\text{O}_{3n+1-\delta}$ thin films from XRD.

like features and kinks in $\text{Pb}_2\text{Sr}_2\text{Bi}_2\text{Fe}_6\text{O}_{16}$ crystals[160], while 2D and 3D RP stacking faults have been witnessed in $\text{LaNiO}_3/\text{LaAlO}_3$ superlattices[167] and $\text{Sr}_{n+1}\text{Ti}_n\text{O}_{3n+1}$ ferroelectric films[162].

Reciprocal Space Maps

Figure 4.4(d) is a symmetric $2\theta - \omega$ scan for the PTFO-100 film around (003) at $\phi = 0$, while panels (e) and (f) are reciprocal space maps around the (103) and (113) LAO substrate peaks respectively (indicated by the dashed lines). The RSMs show that the film's $a = 3.90 \text{ \AA}$ lattice constant is slightly larger than that of the LAO substrate ($a = 3.789 \text{ \AA}$), and that there is negligible polycrystalline texture.

Shallow-Angle X-ray

The ADF-STEM image of Figure 4.2(c) indicates that areas of the perovskite-like layers 1 and 1' have a reduced tetragonal distortion c/a . This changes the atomic density in these layers, creating a periodic modulation in the refractive index that can be seen in shallow-angle X-ray reflectivity scans [solid line in Figure 4.4(c)]. The experimental data for the PTFO-100 sample exhibits a weak peak at $2\theta = 2.45^\circ$ indicative of a superlattice with period $\Lambda = 37.6 \text{ \AA}$ and consistent with the superlattice period calculated directly from the diffraction peaks (Table 4.1). The dashed line shows a model for the shallow-angle reflectivity data modelled by the Genx software[168] assuming the sample comprised a superlattice with two layers, one 2.2 nm layer (with

$c = 4.68 \text{ \AA}$), and another 1.56 nm layer ($c = 3.91 \text{ \AA}$), with superlattice period 37.6 \AA . The density in each bilayer was set by c .

4.2.5 Magnetization Measurement

In-plane and out-of-plane magnetisation measurements using a SQUID magnetometer (Quantum Design MPMS-5S) from 5 K to 300 K in a magnetic field of up to $B = 5 \text{ T}$ on the PTFO-300 film showed little evidence of ferromagnetic order. A weak diamagnetic contribution and a small paramagnetic contribution (rare-earth impurities) from the LAO substrate were seen. The lack of macroscopic ferromagnetic order contrasts with bulk PTFO and thin-films on alternative substrates, and may be a consequence of the spontaneous RP phase of these films, or the disorder introduced by the variations in c throughout the film.

Figure 4.5(a) Shows M - H loops at 5 K for the PTFO-300 film and for a bare LAO substrate with H in plane. The out of plane measurements (not shown) look similar. Figure 4.5(b-i) shows the data presented in (a) once a diamagnetic contribution correction has been carried out. The diamagnetic contribution is indicated by the straight lines in Figure 4.5(a) and was determined such that the data with the diamagnetic contribution removed has a flat saturation regime. Figure 4.5(b-ii) shows a magnification of the M - H loop in (b-i) around zero field. From this it can be seen that there is a very small, but non-zero coercivity in the film. This could be a result of a very weak ferromagnetic component in the film. Figure 4.5(c) shows the temperature dependence of the magnetisation. This shows that at higher temperatures both film and substrate are diamagnetic with a paramagnetic contribution at lower temperatures. Figure 4.5(d) shows the susceptibility, $\chi = \frac{\vec{M}}{H}$, for the increasing temperature sweep. Both the LAO substrate and film are paramagnetic as both have susceptibilities that are linear with $1/T$ and thus follow the Curie law, $\chi = \frac{C}{T}$, with Curie constant, $C \approx 1.05 \times 10^{-4} \text{ K}$. This contribution is likely to arise from rare-earth impurities in the substrate, which are common in LAO. The Curie constant is given

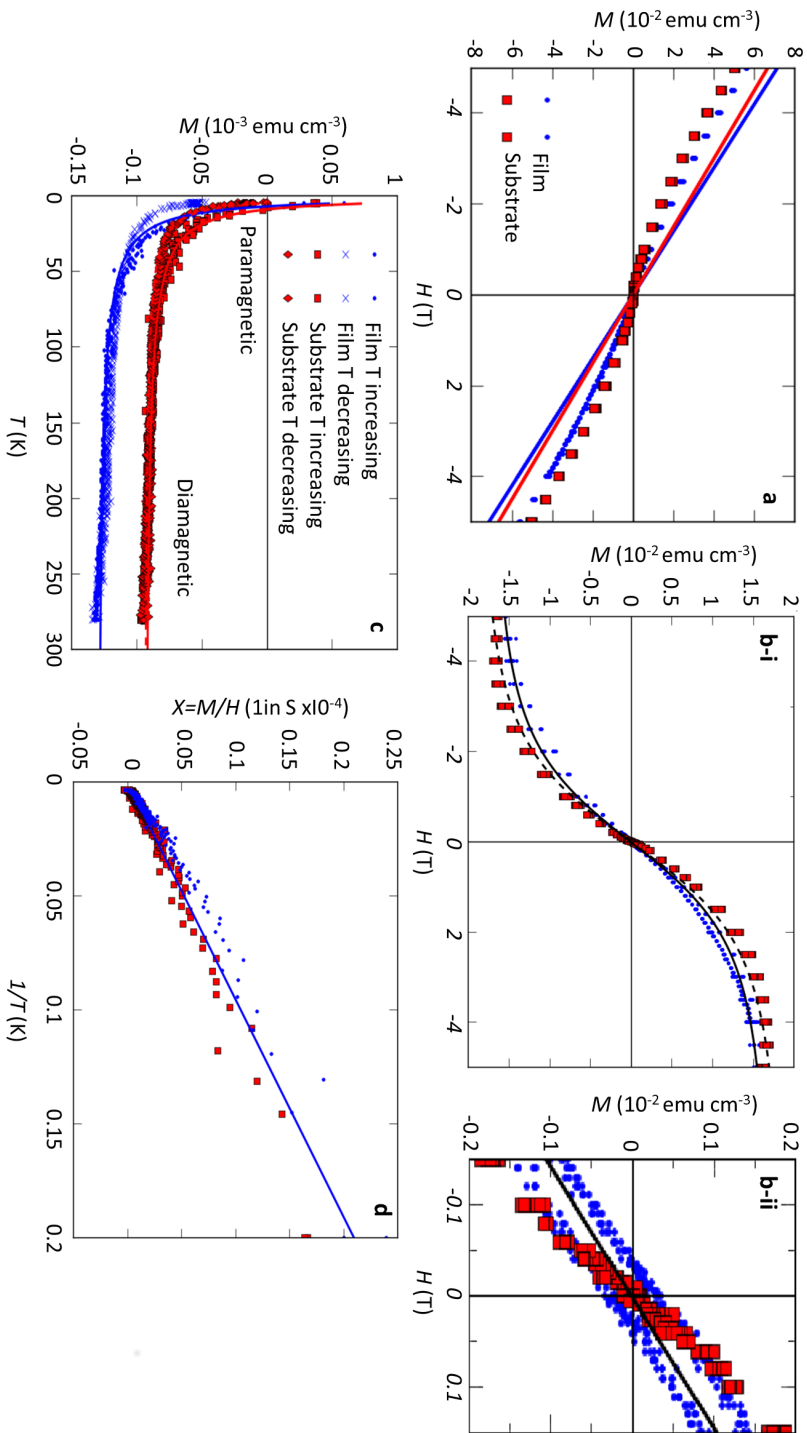


Figure 4.5: Magnetisation measurements for PTFEO-300 and LAO substrate: (a) $M - H$ loops (b-i) $M - H$ with diamagnetic contribution correction. (b-ii) Shows a magnified section from (b-i) around zero field. (c) Temperature dependence of Magnetisation (d) Susceptibility χ vs $1/T$ Temperature. [Magnetization measurements performed by M. R. Lees]

by [94]

$$C = \frac{N\mu_0\mu_B^2g^2J(J+1)}{3K_B} \quad (4.2)$$

where:

N = Magnetic ion density

μ_0 = Magnetic permability of free space ($4\pi \times 10^{-7} \text{ Hm}^{-1}$)

μ_B = Bohr magneton

g = g-factor

J = Total angular momentum quantum number

K_B = Boltzmann's constant ($1.3807 \times 10^{-23} \text{ JK}^{-1}$)

With $g \approx 2$ and assuming $J \approx 3.5$ for a rare earth ion the magnetic density is approximately $6.6 \times 10^{22} \text{ m}^{-3}$. This equates to 0.003% of LAO unit cells having 1 rare earth ion.

4.3 Linear and non-linear optics in the visible-UV

4.3.1 UV-Vis

The UV-visible absorption coefficient α at normal incidence and room temperature is reported in Figure 4.6(a). Room temperature transmittance spectra T were taken in the range 1 to 5 eV using a Perkin-Elmer LAMBDA 1050 UV/Vis/NIR Spectrophotometer at normal incidence.

The absorption coefficient, $\alpha = -\ln(T/d)$, was determined, where d is the film thickness from ellipsometry (see Table 4.2). The absorption coefficient varies with the film thickness, and an increase in the absorption edge ($\sim 2.5 \text{ eV}$) is evident with reduced film thickness. The shift is most pronounced for the PTFO-100 film, and coincides with the increased tetragonal distortion for thinner films [Figure 4.4(a) and Table 4.1]. In the region below the band gap, before the film begins to absorb strongly,

the reported absorption coefficient exhibits oscillations that are artefacts caused by thin film interference.

4.3.2 Ellipsometry

Ellipsometry spectra (Δ , Ψ) for 3 angles of incidence ($\theta=60^\circ$, 65° and 70°) were taken in the range 1-5.5 eV using a Horiba Scientific UVISSEL Ellipsometer, at the University of Birmingham. The experimental spectra in Δ and Ψ were then fitted using a Tauc-Lorentz oscillator model[130] to extract the dielectric function, $\epsilon = \epsilon_1 + i\epsilon_2$. The Tauc-Lorentz model is made up of oscillators that share a common Tauc gap, E_g . The real part of the dielectric function, ϵ_1 was calculated from the imaginary part, ϵ_2 using the Kramers-Kronig relations. For further details on Ellipsometry see Section 2.2 in Chapter 2.

The real and the imaginary part of the dielectric function ($\epsilon = \epsilon_1 + i\epsilon_2$) for PTFO-100, -200 and -300 extracted from ellipsometry measurements are shown in Figure 4.6(b). The imaginary part was calculated using the Tauc-Lorentz model[130], which has previously been applied to amorphous semiconductors[130] and to the multiferroic BiFeO₃[114]. The Tauc-Lorentz model accounts for a finite density of states below the bandgap, making it sensitive to the trap levels that play an important role in the bulk photovoltaic effect in ferroelectrics[17, 169, 170].

Two Tauc-Lorentz oscillators with a common energy gap E_g were used for each film. The determined film thicknesses were in good agreement with their nominal values, as summarised in Table 4.2, which also gives the parameters for the Tauc-Lorentz oscillators. Oscillators are represented graphically in Figure 4.6(b) by the shaded curves. As the film thickness is increased the central energy of the individual oscillators is blue-shifted.

The dashed data in Figure 4.6(a) is the absorption coefficient as determined from ellipsometry. Note that unlike α from UV-visible spectroscopy there is no oscillatory artifact in the absorption present below the band gap in the ellipsometry results. This

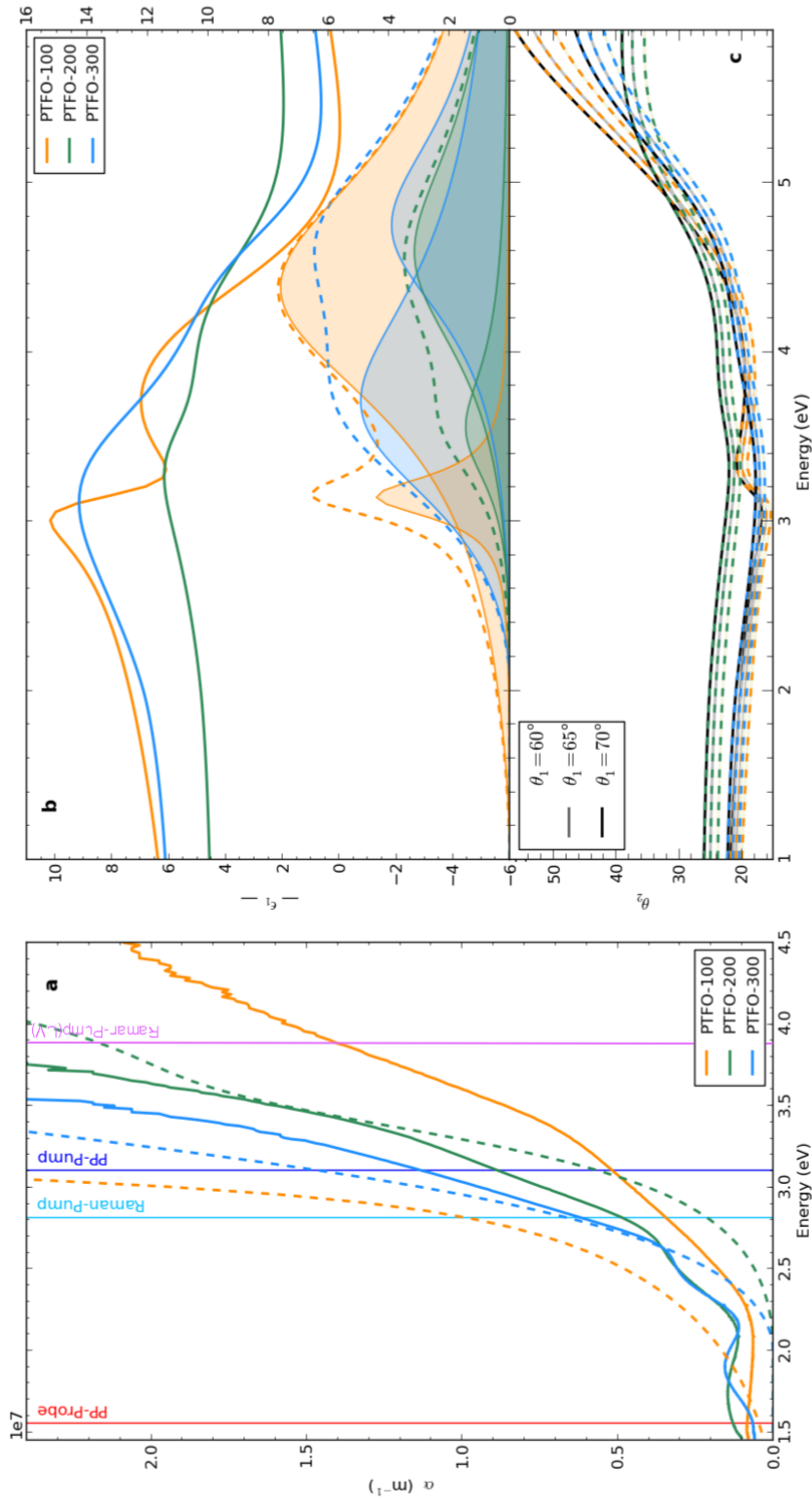


Figure 4.6: Linear optics of PTFO films: (a) UV-visible absorption coefficient α from transmission at normal incidence (solid lines), and from ellipsometry (dashed lines). Vertical lines indicate pump and probe energies used for ultrafast Pump-Probe (PP) spectroscopy and pump energy for Raman. (b) Real (ϵ_1 , solid lines) and imaginary (ϵ_2 , dashed) parts of complex dielectric function in the UV-visible range, as determined from ellipsometry. Shaded areas show the contribution of each mode to ϵ_2 . (c) Internal angle for Ellipsometry measurements.

because the analysis of ellipsometry data explicitly accounts for thin-film interference.

There are clear differences between the UV-visible transmission results (obtained at normal incidence) and the ellipsometry findings (at large angles) above the absorption edge. These may arise from the film's optical anisotropy in the growth (z) direction. The tetragonal phase will have a dielectric tensor with $\epsilon_{xx} = \epsilon_{yy} \neq \epsilon_{zz}$, which means that the optical response in the c direction will differ to that in the $a-b$ plane. This is not taken into account in the analysis of the ellipsometry data. Figure 4.6(c) shows the spread of internal angles (θ_2) for the three incident angles (θ_1) of the ellipsometry measurements. The internal angle of the beam from the normal is wavelength dependent, as the refractive index in the film, n_2 , is wavelength dependent. This can be determined from the refractive index in the film given by the ellipsometry measurements using Snell's Law:

$$\theta_2 = \arcsin\left(\frac{n_1}{n_2} \sin \theta_1\right) \quad (4.3)$$

where, as the measurements were carried out in air, n_1 is the refractive index of air. This gives maximum and minimum internal angles of 15° and 57° .

The direct optical absorption edge of the PTFO films, at about 2.5 eV, is comparable to that of rhombohedral BFO (2.7 eV) and below that of tetragonal BFO (3.1 eV)[114]. The onset of absorption, parameterised by the Tauc bandgap E_g , is lower for PTFO (< 2 eV) than BFO (2.14 eV and 2.30 eV for rhombohedral and tetragonal phase films)[114]. A detailed comparison between the UV-visible and ellipsometry results on PTFO reveals that there is a redshift in the absorption edge from UV-visible transmission for increasing film thickness (lower c), while the individual oscillator energies from ellipsometry blue shift. This can be understood as a consequence of the changes to oscillator widths Γ and amplitudes A : a slight increase in oscillator energies is swamped by a marked increase in Γ and A of the lowest mode. The increase in Γ could occur due to a larger variation in c throughout the thicker

Ellipsometry						
	E_i (eV)	A_i (eV)	Γ_i (eV)	ϵ_∞ (UV)	E_g (eV)	d (nm)
PTFO-100	3.14	2.82	0.31	3.07	0.95	107
	4.42	22.76	1.85			
PTFO-200	3.51	6.65	0.88	3.3	1.97	225
	4.55	16.00	1.63			
PTFO-300	3.58	39.12	1.64	3.3	1.97	326
	4.72	16.73	1.45			

Table 4.2: Optical properties of PbTiFeO₃ thin films, from ellipsometry. It is worth nothing that the values for E_g presented here are the Tauc band gaps arising from the ellipsometry models. The band gaps of the films can also be extracted from the UV-Vis data presented in Figure 4.6(a). Using this approach the exact values for band gaps would depend on the model used. However, looking at Figure 4.6(a) a rough evaluation by graphically extrapolating the absorption coefficient to zero suggests that the bandgaps could in fact be fairly similar, between 2.0-2.3 eV.

films.

4.3.3 Second Harmonic Generation

A mode-locked Ti:sapphire laser oscillator (4 MHz, 650 nJ, 50 fs) provided the fundamental beam (800 nm or 1.55 eV) for second harmonic generation (SHG) measurements. A PMT placed after an analyser and short pass filters was used to detect the second harmonic. Samples were at $\theta = 45^\circ$ from their surface normal, and with the incident beam polarised at angle ϕ ($\phi = 0$ corresponding to p-polarisation). For further details on SHG see Section 2.3 in Chapter 2.

The second harmonic generation (SHG) intensity $I_{p,s}(\phi)$ was obtained as a function of the polarisation angle ϕ of the incident 800 nm pump pulse, for p -polarised and s -polarised detection, as reported in Figures 4.7(a)-(e) for the PTFO-100, -200 and -300 films. The clear SHG signal may arise from either (i) a non-centrosymmetric crystal structure at room temperature for the films, or (ii) an interfacial contribution

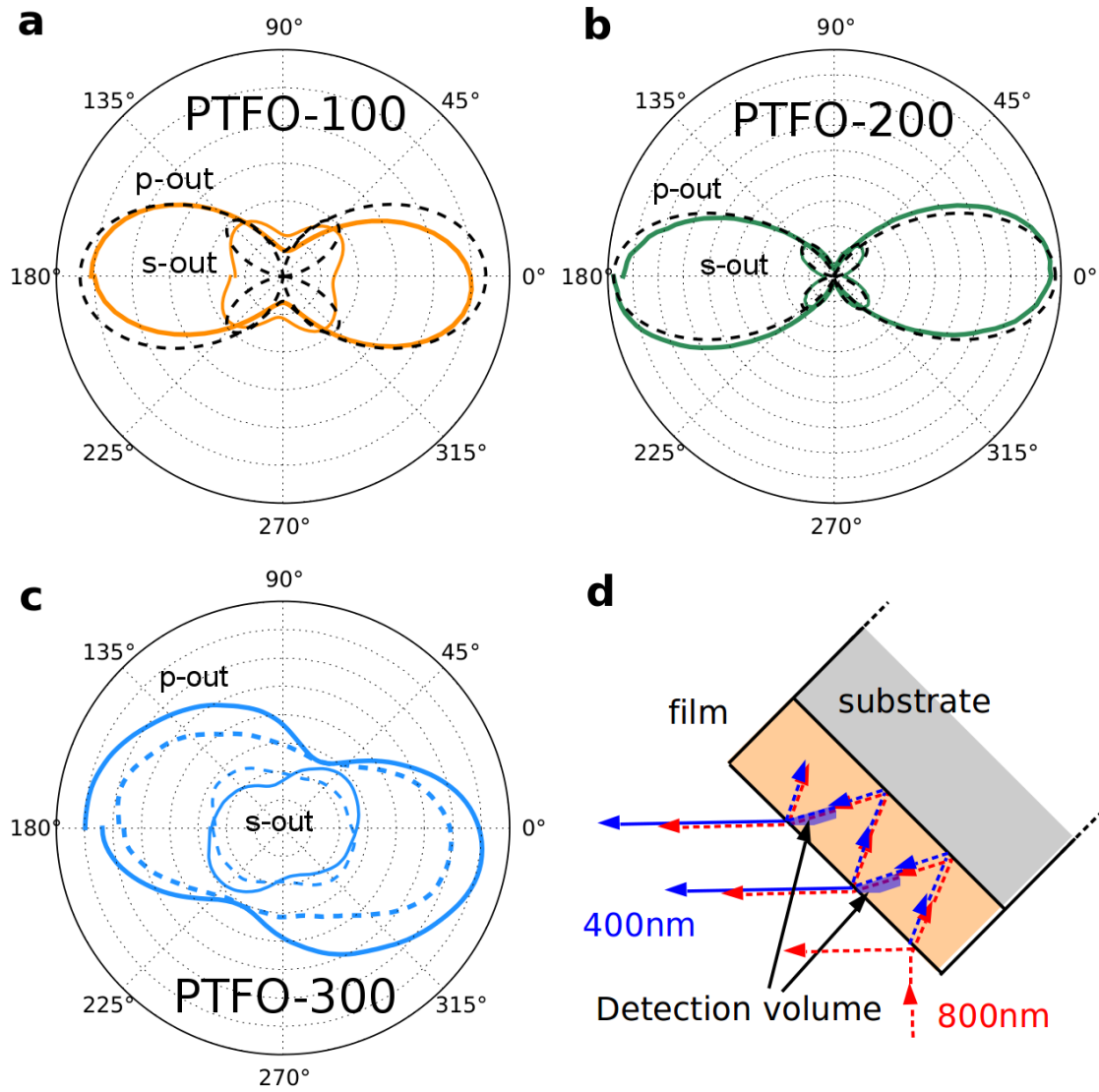


Figure 4.7: Second harmonic generation of PTFO films: (a), (b) and (c) show the SHG radiation patterns for PTFO-100, -200 and -300 respectively, as a function of sample azimuthal angle ϕ ($\phi = 0$ corresponding to p-polarised input) for $\theta = 45^\circ$. Data are shown for *p*-polarised (“*p*-out”) and *s*-polarised (“*s*-out”) detection. In (a) and (b) the dashed black lines show the SHG intensities expected for a tetragonal phase from the model described in the text. In (c) the dashed and solid lines correspond to SHG from two different spots on the sample surface. (d) SHG (blue) can only be detected from the “detection volumes” (blue shaded areas) defined by the film’s finite absorption depth at the second harmonic.

due to the break in translational symmetry (surface SHG). The peak SHG intensity $I_p(\phi)$ was found to be in the ratio 1.0:8.0:0.7 for the PTFO-100, -200 and -300 films. The strong increase in SHG intensity between the PTFO-100 and PTFO-200 film indicates that any contribution from surface SHG is negligible in comparison to the SHG signal from the polar film, as a surface SHG contribution should not vary with film thickness. The observed intensity ratio can be qualitatively understood with reference to Figure 4.7(d). The second harmonic (blue dashed lines) is generated throughout the film by the fundamental (red dashed lines) as the absorption coefficient at 800 nm is negligible. While the SHG intensity should increase with the length squared for a transparent medium, absorption in the films at 3.1 eV (400 nm) means that not all of the generated SHG is detected. Rather, the detected second harmonic comes from the region close to the film/air interface and for beams propagating in the correct direction, labelled the “detection volume” in Figure 4.7(d). The depth of the detection volume can therefore be limited to the absorption depth, which is $1/\alpha=200$ nm, 111 nm and 91 nm for the PTFO-100, -200 and -300 films [from Figure 4.7(a)]. Thus, for the PTFO-100 film the SHG signal can come from the whole film thickness, while for the PTFO-300 film only the top 91 nm contributes. Since the thickest film exhibits smaller tetragonality c/a and strain relaxation in the detection volume (as evidenced by the XRD results), the SHG intensity is therefore reduced for PTFO-300.

The SHG ϕ -plots can be qualitatively understood as follows. Since the sample is rotated around the vertical axis by $\theta = 45^\circ$ there is a maximum component of the electric field of the incident beam along the c -axis (ferroelectric polarisation direction) for a p -polarised fundamental, leading to maxima in the SHG intensity at $\phi = 0$ and $\phi = 180^\circ$, and a double-lobed shape. Quantitatively, for a tetragonal phase with point group 4mm, the ϕ -dependence of the detected SHG intensity is $I_p(\phi) = (A \cos^2 \phi + B \sin^2 \phi)^2$ and $I_s(\phi) = C \sin^2 2\phi$, where the constants A , B and C are linked to the SHG coefficients d_{31} and d_{15} , as described by Kumar *et al.* [132]

for tetragonal-phase BiFeO₃. The black dashed lines in Figures 4.7(a)-(b) show such fits, which are in good agreement with experiment for the two thinner films. For the PTFO-300 $I_{p,s}(\phi)$ varied somewhat between different spots on the sample [solid and dashed lines in Figure 4.7(c)], and the maximum intensity was away from p -polarised incident light for p -polarised detection. The distortion of the crystal structure due to strain relaxation near the surface (in the detection volume), such that the ferroelectric polarisation is no longer along [001], may explain shape of the $I_{p,s}(\phi)$ for the PTFO-300 film. Similar results were obtained on polydomain 4mm (Ba,Sr)TiO₃ films with a deviation in ferroelectric polarisation from the c -axis[171]. Alternatively, anisotropy of the dielectric function at the second harmonic's wavelength may modify the polarisation state detected experimentally from the predicted pattern.

4.4 Ultrafast Optical Reflectivity

A mode-locked Ti:sapphire laser oscillator (4 MHz, 650 nJ, 50 fs) provided the fundamental beam (800 nm or 1.55 eV) for time-resolved reflectivity experiments. The fundamental was doubled in frequency to 400nm (3.1 eV) to photoexcite the multi-ferroic films at a fluence of $60 \mu\text{Jcm}^{-2}$. The transient optical reflectivity subsequent to excitation was detected using a time-delayed fraction of fundamental beam, which was incident on the sample at close to normal incidence. The absorption depth of the samples for the pump and probe are 65-355 nm at $\lambda = 400$ nm and greater than $1.5 \mu\text{m}$ at $\lambda = 800$ nm. For further details on time-resolved pump-probe reflectivity see Section 2.1 in Chapter 2.

4.4.1 Electronic Component

Photoinduced changes in reflectivity ΔR result from a modified refractive index Δn (at the probe wavelength) caused by changes in the occupancy of electronic states. Time-resolved reflectivity thus permits electronic generation and relaxation processes

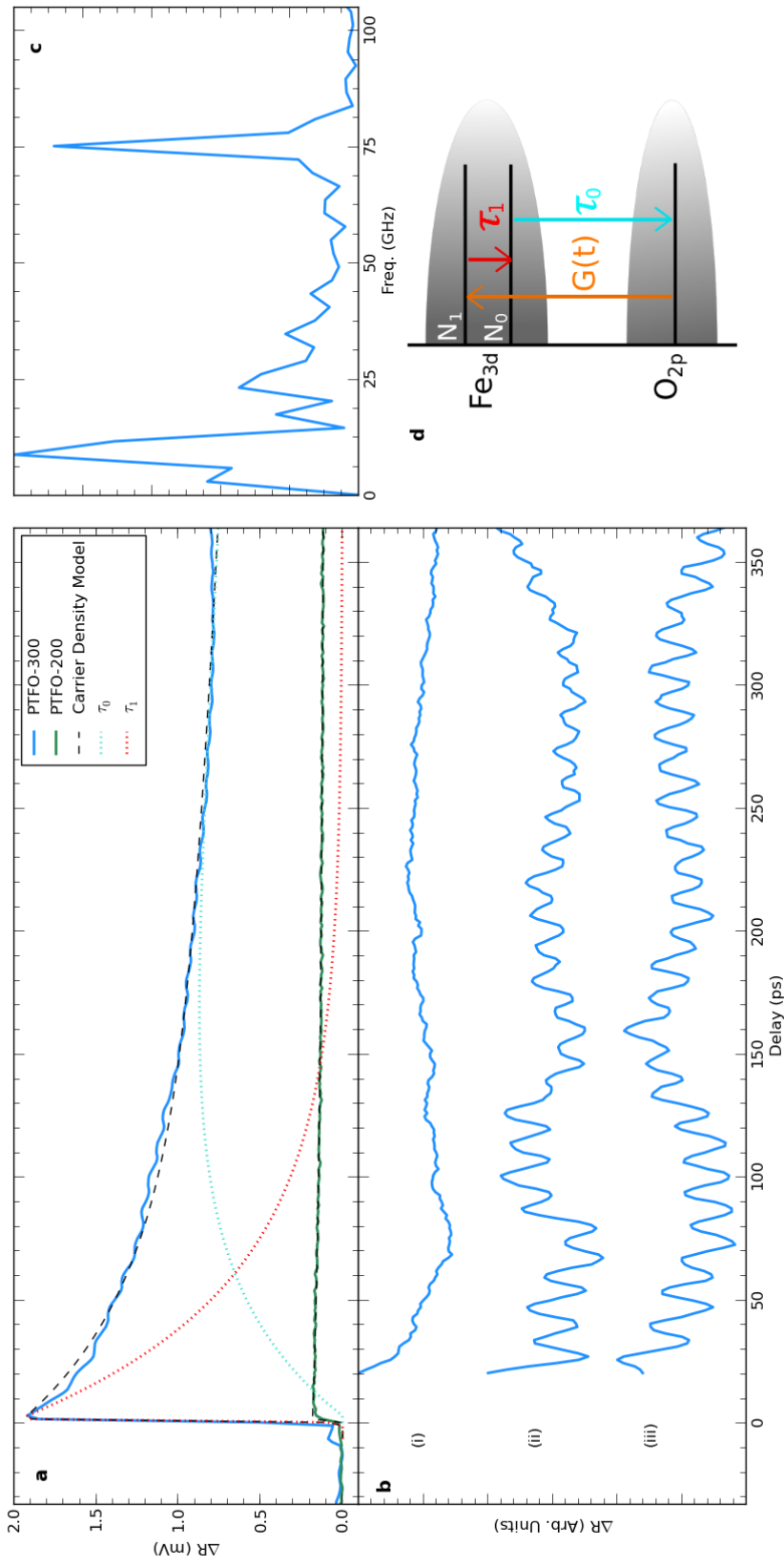


Figure 4.8: Pump probe spectroscopy of PTFO films: (a) Pump probe for PTFO-300 (blue) and PTFO-200 (green) with carrier density model fits (black dashed). The density of the 'hot' and 'cold' carriers (red and blue dotted curves respectively) (b) Extracted signal for different regions of the PTFO-300 film which showed with (i) no oscillations, (ii) oscillations, and (iii) 180° phase shifted oscillations. (c) FFT of oscillation in b(ii). (d) Schematic diagram of carrier density model.

to be examined. Further, coherent oscillations in ΔR can result from phonons[109, 127] and in multiferroics also magnons[88, 102]. The observed transients for the PTFO films (Figure 4.8(a)) comprise an electronic component with a sharp rise and a non-exponential decay for both films.

Similar ultrafast reflectivity transients (with a rapid rise and a non-exponential decay) have been reported in recent studies of bulk BFO[98, 99] and thin films grown on a variety of substrates[100, 100, 101, 102]. The rapid rise in reflectivity after excitation is attributed to the transfer of electrons between states. In BFO this is $O_{2p} \rightarrow Fe_{3d}$ [97]; similar transitions to Fe_{3d} or Ti_{3d} are expected here. The electronic response for the PTFO-200 film is reduced in comparison to that of the PTFO-300 sample because of its reduced absorption at the pump energy [Figure 4.6(a)].

The subsequent electronic decay can be approximated by the sum of two exponentials, $\Delta R = Ae^{-t/\tau_1} + Be^{-t/\tau_0}$, with lifetimes $\tau_1 = 113$ ps and $\tau_1 = 78$ ps for PTFO-200 and -300 respectively, and $\tau_0 > 1$ ns. However, such a biexponential model would signify that two independent photoexcited electron populations contribute to ΔR .

Carrier Density Model

A model that includes carrier cooling between two levels[172] can be used as a more physical alternative to a biexponential model. In this approach electrons are photoexcited with density N_1 into an upper level 1, and relax with rate N_1/τ_1 (corresponding to the cooling rate of ‘hot’ electrons) to lower level 0, as illustrated in the schematic in Figure 4.8(d). The change to the reflectivity is proportional to the carrier density, N ;

$$\Delta R \propto N \tag{4.4}$$

where the carrier density is given by the total occupancy of the excited ‘hot’ and

‘cold’ states;

$$N = N_0\Gamma_{cool} + N_1 \quad (4.5)$$

where N_0 and N_1 are the density of ‘cold’ and ‘hot’ carriers respectively. Γ_{cool} is a scale factor between the ‘hot’ and ‘cold’ carrier densities. This takes into consideration that the ‘hot’ and ‘cold’ carriers can affect the change in the reflectivity, dR , differently. For $\Gamma_{cool} < 1$ the ‘cold’ carriers produce a smaller change to the reflectivity, R , than the ‘hot’ carriers. In this case if some of the ‘hot’ states (N_1) are filled then the change to ϵ_2 (or α) is larger than filling the same number of ‘cool’ states (N_0). As $\Gamma_{cool} \rightarrow 1$ the contribution of the ‘hot’ and ‘cold’ carriers start to be more similar. This is what would be expected as the energies of states move closer together. The rates of change of carrier density for each of the states is given by;

$$\frac{dN_1}{dt} = G(t) - \frac{N_1}{\tau_1} \quad (4.6)$$

$$\frac{dN_0}{dt} = \frac{N_1}{\tau_1} - \frac{N_0}{\tau_0} \quad (4.7)$$

where τ_1 is the relaxation time of ‘hot’ carriers, τ_0 is the band-to-band recombination time for ‘cold’ carriers and $G(t)$ is the ‘hot’ carrier generation rate.

The fits obtained by this method are shown as black dashed lines along with the raw data in Figure 4.8(a). The red and blue dotted curves presented along with the PTFO-300 fit and data are the density of ‘hot’ (N_1) and ‘cold’ (N_0) carriers respectively.

This approach gave $\tau_1 = 89$ ps, $\tau_0 = 2150$ ps and $\Gamma = 0.7$ for PTFO-200, and $\tau_1 = 63$ ps, $\tau_0 = 1350$ ps and $\Gamma = 0.5$ for PTFO-300. The greater lifetime of the fast component for PTFO-200 can be explained by the closer proximity of the pump energy to the band edge, where cooling rates are lower. The $\tau_0 > 1$ ns lifetime for photocarrier recombination makes PTFO potentially useful in optoelectronic applications that

require slow population decay, such as ferroelectric photovoltaics.

The comparable cooling scales of 0.7 for the PTFO-300 film and to 0.5 for PTFO-200 film means that the relative strength of the ‘hot’ carrier’s contribution is similar for the two films.

4.4.2 Oscillatory Component

After numerical removal of the electronic contribution to ΔR a distinct oscillatory component superimposed on the reflectivity transient is observed for PTFO-300, as reported in Figure 4.8(b), at a frequency of around 75 GHz [See FFT, Figure 4.8(c)]. The different curves (i)-(iii) correspond to different locations on the sample. While in the majority of positions ΔR exhibited a very similar behaviour to that shown in curve (ii), in a smaller number of cases either no oscillations [curve (i)] or oscillations with a 180° phase shift [curve (iii)] were observed. Acoustic phonons can contribute to ΔR for oxide thin films[102]. The corresponding oscillation frequency depends on the acoustic phonon velocity, and thus changes when the acoustic pulse propagates from the film to the substrate. Acoustic phonons in the substrate may be responsible for the peaks at low frequency (and from long time delays) in Figure 4.8(c). However, the high frequency (75 GHz) feature cannot result from the acoustic phonon mechanism, as the oscillation is present at all time delays and does not correspond to the acoustic phonon mode frequencies expected for LAO[102, 151]. In the study of magnons in BiFeO₃ thin films (discusses in Chapter 3) a mode at a comparable frequency was found to disappear above the Néel temperature. Both the PTFO films reported here and the BiFeO₃ films of Ref. 102 had LAO substrates, and therefore have comparable in-plane lattice constants and Fe-Fe distances (assuming that there are regions of the PTFO samples with Fe ions in adjacent cells). It is thus plausible that the oscillation here is also a magnon. To confirm this, demonstrating that it disappears above the Néel temperature is desirable and will be the subject of further study. The occasional absence of the magnon and the 180° phase shift could be attributed to ferromagnetic

domains or sample inhomogeneity.

4.5 IR active phonons

4.5.1 FTIR

FTIR reflectivity spectra were taken using a Bruker Vertex 70v spectrometer at an angle of incidence of 11° . A global light source was used, along with a KBr beamsplitter/DLaTGS detector for the mid-IR range (50–1000 meV), and a Si beamsplitter/DTGS detector for the far-IR range (15–48 meV). For further details on FTIR spectroscopy see Section 2.5 in Chapter 2.

FTIR reflectivity spectra are presented in Figure 4.9 (solid lines). The substrate data (black line) displays three Reststrahlen bands. For the PTFO films the reflectivity lowers substantially in the areas marked by the arrows in Figure 4.9(c), and this reduction is more pronounced as the film thickness increases. This is a consequence of phonon modes in the film within the Reststrahlen bands of the substrate.

This was verified by modelling the reflectivity spectra of thin-film PTFO on LAO with the RefFit[173] software (dashed lines). The films were modelled using just the layer stack (*i.e.* substrate and film, Figure 4.9(a)) and with adding oscillators into the film (Figures 4.9(b) and (c) with 1 and 2 oscillators respectively). RefFit models the reflectivity of a multilayer sample following the approach of Harbecke[174]. A Drude-Lorentz dielectric function was used, of the form:

$$\epsilon(\omega) = \epsilon_\infty + \sum_i \frac{A_i}{\omega^2 + \omega_i^2 + i\omega\Gamma_i} \quad (4.8)$$

where $A_i = \omega_i^2(\epsilon_{s,i} - \epsilon_{\infty,i})$ for each mode i .

The LaAlO₃ substrate was modelled with a 6-phonon model similar to results reported elsewhere[175, 176] (Black dashed curved in Figure 4.9). The substrate fit is discussed in more detail in section 4.5.4. The films were modelled assuming a fixed thickness, as determined from ellipsometry. In Figure 4.9(a) no oscillators are

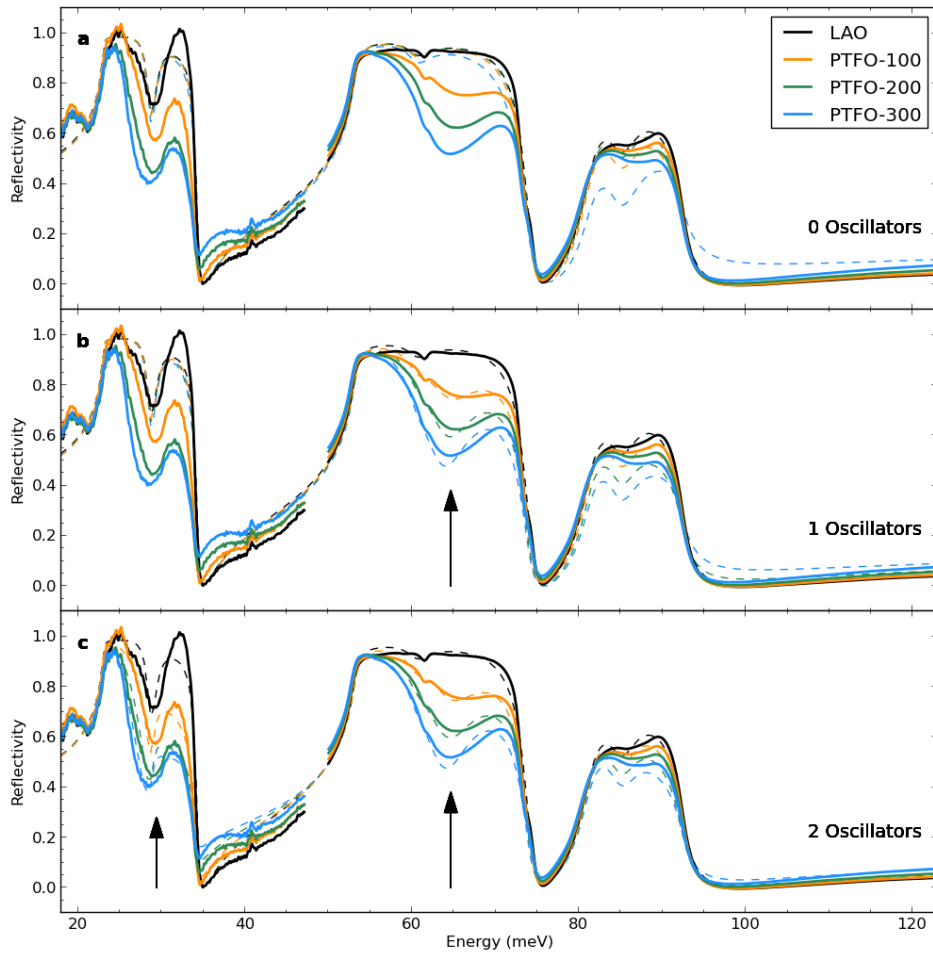


Figure 4.9: Reflectivity from FTIR spectroscopy (solid lines). Models (dashed lines) with (a) thickness only (b) 1 oscillator and (c) 2 oscillators as described in the text.

FTIR, THz*				
	E_i (meV)	A_i (meV)	Γ_i (meV)	ϵ_∞ (NIR)
PTFO-100	29.25	108.89	8.19	4.62
	64.83	63.70	6.81	
PTFO-200	29.75	102.38	7.57	4.98
	64.64	60.70	6.91	
PTFO-300	9.1*	33.2	3.3	5.22
	29.63	101.83	7.89	
	64.58	58.29	6.56	

Raman			
	E (meV)	A (arb. units)	Γ (meV)
PTFO-200	29.0	0.1	4
	38.5	0.14	5
	49.0	0.085	5
	64.0	0.05	5
	88.6	0.1	10
	99.8	0.055	4
	113.0	0.045	5

Table 4.3: Optical properties of PbTiFeO₃ thin films, FTIR spectroscopy/THz-TDS (top) and Raman (bottom). Oscillator parameters are given in units of meV.

included; the film is assumed to have $\epsilon(\omega) = \epsilon_\infty$, as in Table 4.3. It can be seen that the thin film effect alone does not account for the reductions in the reflectivity around the areas marked by the arrows in Figure 4.9(c). Figure 4.9(b) and (c) successively add in oscillators at 29.5 meV and 64.7 meV. It can be seen that adding oscillators into the dielectric function of the film substantially improves the fit. There is little shift in the mode frequencies with thickness, as demonstrated by the values in Table 4.3.

4.5.2 THz Time-Domain Spectroscopy

Terahertz time-domain spectroscopy[177, 178] was used to examine the dielectric function in the range of 1-13 meV, from amplitude and phase resolved transmission mea-

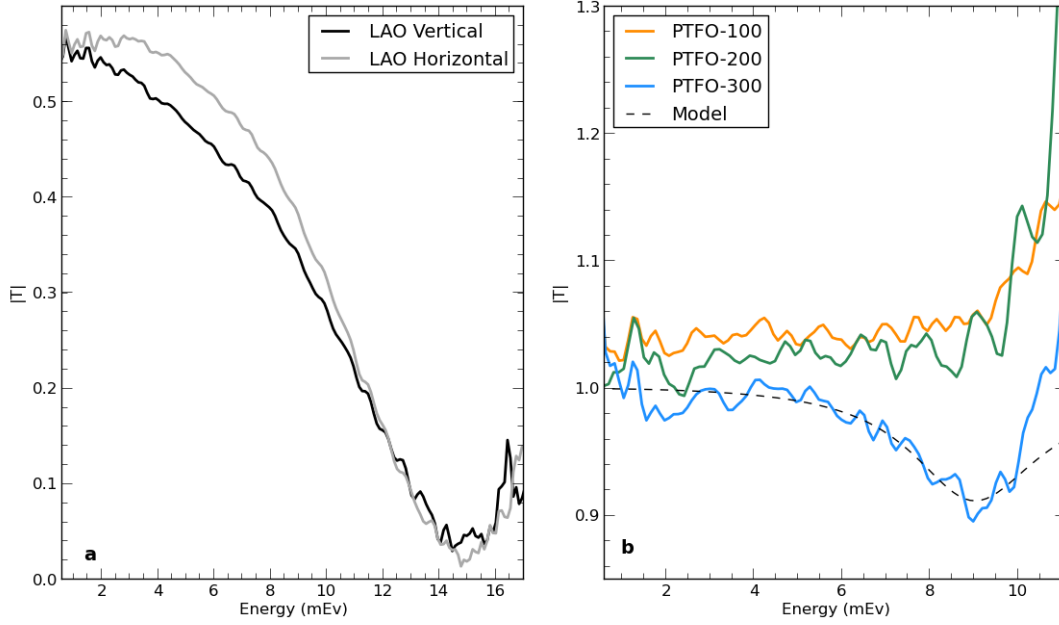


Figure 4.10: (a) Transmission in the far-infrared (from THz-TDS, see Methods) through vertically (black) and horizontally (grey) oriented LAO relative to vacuum. (b) Transmission in the far-infrared through PTFO relative to that through a bare LAO substrate.

measurements. The THz pulse was generated by a 800 nm, 20 fs pulse from a Ti:sapphire laser focused onto a GaAs photoconductive switch and detected by electro-optic sampling. For further details on THz time-domain spectroscopy see Section 2.4 in Chapter 2.

The spectral transmission was calculated from the FFT of the time-domain data, using blank LaAlO_3 as the reference. Data were averaged over four possible orientations of the PTFO samples and a blank substrate (VV , VH , HV , HH , where H/V represent horizontal or vertical orientation of the sample and reference substrate respectively). This removes the influence of substrate anisotropy[146]. Evidence of this anisotropy can be seen in Figure 4.10(a). It can be seen that there is a slight difference in the THz transmission, and thus the refractive index, for the V and H orientations of LAO. It is possible that the domain microstructure of the substrate is contributing to this effect[146].

The THz spectral transmission of the PTFO films is reported in Figure 4.10(b), and is flat and featureless for the PTFO-100 and PTFO-200 samples in the range below 10 meV. Above 10 meV all samples exhibit a sharp rise in transmission. This is an artifact which arises from the LaAlO_3 substrate, which acts as a half wave plate at these frequencies[146]. The response for the PTFO-300 film displays a prominent reduction in transmission around 9 meV in Figure 4.10(b). The dashed line indicates the transmission calculated for a thin film of PTFO on LAO, assuming that the dielectric function of the film includes a phonon at 9.1 meV (2.2 THz) as described by Equation 4.8 with linewidth $\Gamma = 3.3$ meV, $\epsilon_s = 31.1$ and $\epsilon_\infty = 17.8$. Here, ϵ_∞ was chosen to match ϵ_s from the FTIR results.

Large dielectric constants ϵ_s (reported here in the THz range) are often observed in ferroelectrics[179] and incipient ferroelectrics. The extra mode seen in THz-TDS for PTFO-300 is not visible for the 100 nm or 200 nm samples. This may be a consequence of the experimental sensitivity, as thinner films produce smaller transmission changes, or be a feature of PTFO films above a certain thickness.

4.5.3 Raman active phonons

Raman spectra were taken using a Renishaw inVia Reflex Raman microscope with an excitation wavelength of 442 nm (2.81 eV) and focused with a 20 \times objective. UV-Raman spectra were taken under excitation at 325 nm (3.82 eV) and with a 40 \times objective. The Raman filters used for the 442 nm and 325 nm lasers cut out all signal below 10 meV and 52 meV, respectively, limiting the spectral range at low energies. For further details on Raman spectroscopy see Section 2.6 in Chapter 2.

Raw Raman spectra for the PTFO samples and a (001)-oriented LaAlO_3 reference sample obtained under 442 nm (2.81 eV) excitation are presented in Fig. 4.11(a). As the films are not strongly absorbing at this wavelength (see Figure 4.6(a)), there is a strong component from the LaAlO_3 substrate (black line). In contrast, using 325 nm (3.82 eV) excitation, where the film absorbs strongly, yields a dominant Raman signal

from the PTFO films (coloured lines in Figure 4.11(b)), but over a more limited spectral range. For the data obtained at 442 nm the subtraction of the substrate's contribution[180] permits the Raman spectra of the PTFO films to be seen (coloured lines in Figure 4.11(c)). The narrow gaps correspond to the sharp Raman active modes $A_{1g} + 4E_g$ of the substrate, as set out in Table 4.4. For further discussion of the substrate's modes see section 4.5.4.

The Raman modes of the films are broader than those previously seen for bulk PTFO (with $x = 0.05$ and $x = 0.1$),[79] which are reproduced by the solid thin black lines in Fig. 4.11(c) along with their mode assignments. Furthermore, the Raman active modes of $\text{Pb}_{n+1}(\text{Ti}_{0.67}\text{Fe}_{0.33})_n\text{O}_{3n+1-\delta}$ are shifted in energy in comparison to those at lower x [79]. The large changes in c evidenced by TEM will also alter the phonon eigenfrequencies, and this disorder will broaden the Raman resonances. As a does not vary substantially, eigenmodes that are IR-active in the plane may not be broadened as significantly. The PTFO-200 data was modelled by a series of Lorentzians (black dashed lines in panels b and c), where the arrows in Fig. 4.11(c) indicate the position and strength of the individual oscillators for the fits to the substrate-subtracted 442 nm data. For the fit in Fig. 4.11(b) (325 nm excitation, PTFO-200 film) only two Lorentzians were used, to better highlight the peaks at 65 meV and 97 meV.

Importantly, for ferroelectric media without an inversion centre vibrational modes can be both Raman and infrared active, as for PbTiO_3 . [181] For the two IR-active modes observed for $\text{Pb}_{n+1}(\text{Ti}_{0.67}\text{Fe}_{0.33})_n\text{O}_{3n+1-\delta}$ at 29.5 meV and 64.7 meV in the FTIR results there are corresponding Raman active modes at 29 and 65 meV visible in the 442 nm Raman data (Figure 4.11(c)), and at 65 meV in the 325 nm Raman data (Figure 4.11(c)). This discludes a centrosymmetric crystal structure for the $\text{Pb}_{n+1}(\text{Ti}_{0.67}\text{Fe}_{0.33})_n\text{O}_{3n+1-\delta}$ films, as in a material possessing a center of symmetry no mode can be both infrared and Raman active by the rule of mutual exclusion.

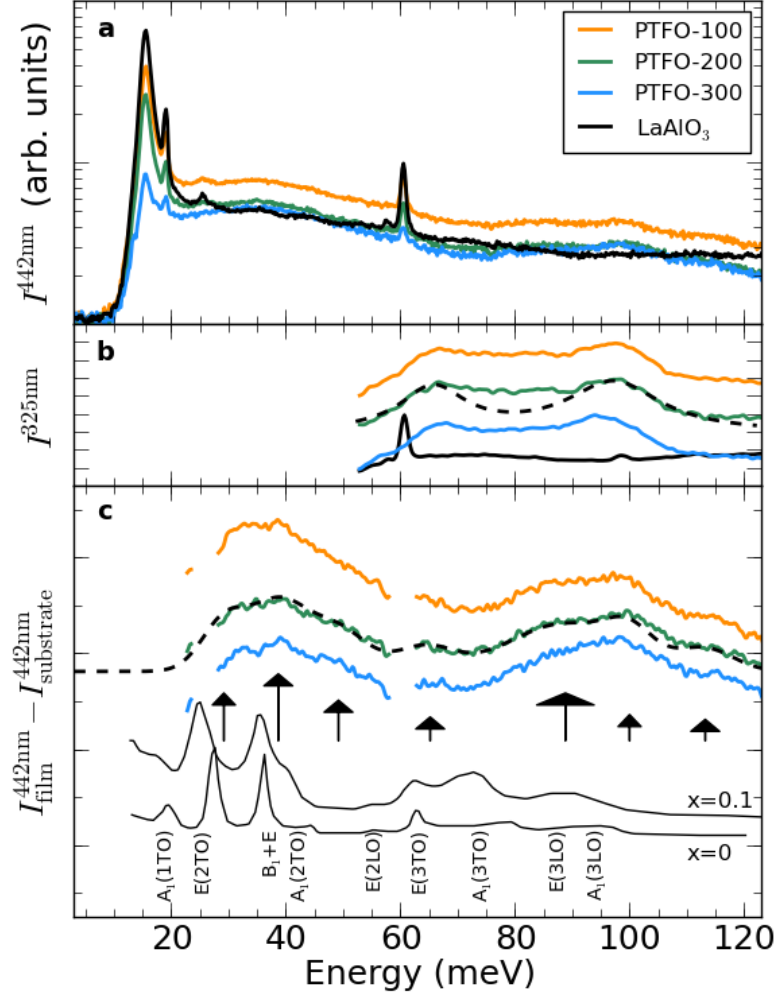


Figure 4.11: Raman spectra of PTFO films and LAO substrate: (a) Raman intensity I under 442 nm excitation. (b) I for 325 nm excitation. The dashed black line indicates a two-Lorentzian fit to the PTFO-200 spectra. (c) Raman intensity under 442 nm excitation after subtracting the substrate's contribution. The dashed black line is the model for PTFO-200 as described in the text and Table 4.3, where black arrows indicate individual oscillators. The lengths of the arrows represent the oscillator strengths, while the widths of the arrow heads denote the widths Γ . The thin back lines (bottom) are the data of Sun *et al.* [79] for $x = 0$ and $x = 0.1$.

4.5.4 Vibrational Modes in LaAlO₃ Substrate

The FTIR data for the LAO substrate was fitted using a Drude-Lorentz dielectric function as described earlier (see section 4.5.1) with 6-phonon oscillator model (see Table 4.4 and black dashed lines in Figure 4.9). For LAO there are 8 IR active modes: $3A_{2u} + 5E_u$ [175, 182]. The modes observed here are compared to those previously predicted from DFT[183] and observed experimentally[175, 176] in Table 4.4. The modes observed at 29.1 meV and 85.4 meV however, do not match up with the IR active modes predicted by DFT, although modes near 85.4 meV have previously been observed experimentally[175] in LAO.

Modes in addition to those predicted by group theory are also present in the Raman spectrum of LAO. The narrow gaps in Figure 4.11 correspond to the sharp Raman active modes $A_{1g} + 4E_g$ of the substrate. These occur at 15.3 meV, 18.9 meV, 25.4 meV, 57.5 meV and 60.3 meV, and correspond well with those previously reported from experiment[184, 185] and theory[183], except for the 25.4 meV mode, as outlined in Table 4.4. The 15.3 meV mode corresponds to an assignment of A_{1g} and the 18.9 meV, 57.5 meV and 60.3 meV modes correspond to an assignment of E_g . This leaves the mode at 25.4 meV in addition to those expected from group theory (assuming that the lowest E_g mode is present but not resolved owing to experimental resolution).

There are a number of reasons why additional IR active and Raman modes can be observed compared to those predicted from group theory. Both techniques should only couple to phonons with close to zero wavevector phonons, q . However, two phonon processes can result in extra modes[186, 187]. This process occurs when there is a high density of phonon states, which can occur at points of high symmetry in the Brillouin zone. Additional modes can also result either from the presence of impurity phases or from oxygen vacancies, which alter the rotational motion.

LaAlO₃ -IR						
Delugas[183]		Calvani[175]		Shimada[176]	This Work	
E (meV)		E (meV)		E (meV)	A (meV)	Γ (meV)
A_{2u}	20.8					
E_u	22.2	E_u	22.6	22.7	23.0	0.16
					29.1	1.26
E_u	36.8					
A_{2u}	50.7			52.9		
E_u	51.0	E_u	53.2	53.4	53.3	0.68
E_u	59.3	E_u	62.2		60.7	3.32
A_{2u}	77.8					
E_u	79.0	E_u	81.5	80.3	80.9	2.64
		E_u	86.2		85.4	4.15
Calvani: $3A_{2u} + 5E_u$						
Shimada: $A_{1u} + 4A_{2u} + 5E_u$.					$\epsilon_\infty = 3.83$	

LaAlO₃ -Raman				
Delugas[183]		Scott[184]	Abrashev[185]	This Work
E (meV)		E (meV)	E (meV)	E (meV)
E_g	4.1	4.1	4.2	
A_{1g}	16.0	15.1	16.4	15.3
E_g	18.1	18.9		18.9
				25.4
E_g	56.3		58.3	57.5
E_g	57.9	60.4		60.3
Scott and Abrashev: $A_{1g} + 4E_g$				

Table 4.4: Comparison of IR and Raman mode energies with those previously obtained from group theory and experiment for LaAlO₃. All mode energies/parameters are given in meV.

4.6 Conclusions

Bulk crystals and thin films of $\text{PbTi}_{1-x}\text{Fe}_x\text{O}_3$ (PTFO) are multiferroic, exhibiting ferroelectricity and ferromagnetism at room temperature. It has been seen that a Ruddlesden-Popper phase $\text{Pb}_{n+1}(\text{Ti}_{1-x}\text{Fe}_x)_n\text{O}_{3n+1-\delta}$ forms spontaneously during pulsed laser deposition of PbTiFeO_3 on LaAlO_3 substrates. High-resolution transmission electron microscopy, x-ray diffraction and x-ray photoemission spectroscopy were utilised to perform a structural and compositional analysis, demonstrating that the number of repeating ABO_3 layers is $n \simeq 8$ and the Fe fraction, $x \simeq 0.33$. The complex dielectric function of the films was determined from far-infrared to ultraviolet energies using a combination of terahertz time-domain spectroscopy, Fourier transform spectroscopy, and spectroscopic ellipsometry. The simultaneous Raman and infrared activity of phonon modes, and the observation of second harmonic generation, establishes a non-centrosymmetric point group for PbTiFeO_3 consistent with ferroelectricity. No evidence of macroscopic ferromagnetism was found in SQUID magnetometry. The ultrafast optical response exhibited coherent magnon oscillations compatible with local magnetic order, and additionally was used to study photocarrier cooling on picosecond timescales. An optical gap smaller than that of BiFeO_3 and long photocarrier lifetimes may make this system interesting as a ferroelectric photovoltaic.

Chapter 5

Conclusions

Time resolved and continuous wave optical techniques have been used to study the properties of multiferroic thin films. It has been seen that transient reflectivity can couple to acoustic phonon and magnon excitations, giving insight into the the lattice dynamics and the magnetic order energy scales associated with the weak ferromagnetic moment in BFO. It as also been seen that a multi-technique approach is beneficial in order to gain a full understanding the differing properties as a result of strain, processing temperature, geometry and composition.

Time-resolved reflectivity has been used to study the dynamics of coherent magnons and acoustic phonons in multiferroic thin films of tetragonal and rare-earth doped BiFeO_3 . The elastic moduli of ferroic thin films are often hard to characterize using traditional transducer-based methods, however this approach allows for direct experimental access to these. These were extracted from the frequency of oscillations in the reflectivity arising from dynamic modulations of the refractive index by acoustic phonons. It was also demonstrated that the ultrafast photoacoustic technique couples to magnons. The creation of a magnon mode was observed to be dependent on either magnetisation or the presence of a tetragonal crystal structure. This observation provides a promising route to creating a magnetoelectric multiferroic with a tailored magnonic response.

High-resolution transmission electron microscopy, x-ray diffraction and x-ray pho-

to emission spectroscopy $\text{PbTi}_{1-x}\text{Fe}_x\text{O}_3$ (PTFO) films grown by on pulsed laser deposition have shown that a Ruddlesden-Popper (RP) phase forms spontaneously in pulsed laser deposition of PTFO. It was demonstrated that the number of repeating ABO_3 layers is $n \simeq 8$ and the Fe fraction, $x \simeq 0.33$. Epitaxial strain or the oxygen-rich growth conditions are both possible candidates for the formation of the RP phase. To establish whether either of these mechanisms have a contributing factor it would be desirable to examine films grown on different substrates.

The complex dielectric function of the films was determined from far-infrared to ultraviolet energies using a combination of terahertz time-domain spectroscopy, Fourier transform spectroscopy, and spectroscopic ellipsometry. From optical spectroscopy techniques there is evidence that the Ruddlesden Popper (RP) phase of PTFO exhibits ferroelectricity. A non-centrosymmetric point group was established from observation of second harmonic generation and from the simultaneous presence of Raman and infrared activity of phonon modes.

The static and ultrafast optical response of PFTO have been seen to be similar to that of BiFeO_3 . PFTO, however has long photocarrier lifetimes and an optical gap that is smaller than that of BiFeO_3 . These aspects may make this system interesting as a ferroelectric photovoltaic, which is currently an area of interest for BiFeO_3 .

No evidence of macroscopic ferromagnetism was found in SQUID magnetometry. This contrasts with previous studies of bulk crystals and thin films of PTFO which have been seen to be multiferroic, exhibiting ferroelectricity and ferromagnetism at room temperature. Although there is no macroscopic ferromagnetism in the RP PTFO phase, magnon oscillations (local magnetic order) have been observed to persist.

Bibliography

- [1] Spaldin, N. A. & Fiebig, M.: Materials science. The renaissance of magneto-electric multiferroics. *Science* **309**, 391–2 (2005).
- [2] Eerenstein, W., Mathur, N. D. & Scott, J. F.: Multiferroic and magnetoelectric materials. *Nature* **442**, 759–65 (2006).
- [3] Hill, N. A.: Why Are There so Few Magnetic Ferroelectrics? *J. Phys. Chem. B* **104**, 6694–6709 (2000).
- [4] Van Aken, B. B., Rivera, J.-P. P., Schmid, H. & Fiebig, M.: Observation of ferrotoroidic domains. *Nature* **449**, 702–705 (2007).
- [5] Kimura, T., Goto, T., Shintani, H., Ishizaka, K., Arima, T. & Tokura, Y.: Magnetic control of ferroelectric polarization. *Nature* **426**, 55–58 (2003).
- [6] Wang, J., Neaton, J. B., Zheng, H., Nagarajan, V., Ogale, S. B., Liu, B., Viehland, D., Vaithyanathan, V., Schlom, D. G., Waghmare, U. V., Spaldin, N. A., Rabe, K. M., Wuttig, M. & Ramesh, R.: Epitaxial BiFeO₃ multiferroic thin film heterostructures. *Science* **299**, 1719–1722 (2003).
- [7] Ramesh, R. & Spaldin, N. A.: Multiferroics: progress and prospects in thin films. *Nat. Mater.* **6**, 21–9 (2007).
- [8] Khomskii, D.: Classifying multiferroics: Mechanisms and effects. *Phys* **2**, 1 (2009).
- [9] Sharan, A., Lettieri, J., Jia, Y. F., Tian, W., Pan, X. Q., Schlom, D. G. & Gopalan, V.: Bismuth manganite: a multiferroic with a large nonlinear optical response. *Phys. Rev. B* **69**, 214109 (2004).
- [10] Dzyaloshinskii, I. E.: On the magnetoelectric effect in antiferromagnets. *J. Exp. Theoret. Phys. (USSR)* **38**, 881–882 (1951).

- [11] Astrov, D. N.: Magnetolectric effect in chromium oxide. *Soviet physics, JETP* **13**, 729–733 (1961).
- [12] Christen, H. M., Nam, J. H., Kim, H. S., Hatt, a. J. & Spaldin, N. a.: Stress-induced $R - M_A - M_C - T$ symmetry changes in BiFeO₃ films. *Phys. Rev. B* **83**, 144107 (2011).
- [13] Dong, S. X., Cheng, J. R., Li, J. F. & Viehland, D.: Enhanced magnetolectric effects in laminate composites of terfenol-D/Pb(Zr,Ti)O₃ under resonant drive. *Appl. Phys. Lett.* **83**, 4812–4814 (2003).
- [14] Bibes, M. & Barthélémy, A.: Multiferroics: towards a magnetolectric memory. *Nat. Mater.* **7**, 425–6 (2008).
- [15] Gajek, M., Bibes, M., Fusil, S., Bouzheouane, K., Fontcuberta, J., Barthelemy, A. E., Fert, A. & Barthélémy, A.: Tunnel junctions with multiferroic barriers. *Nat. Mater.* **6**, 296–302 (2007).
- [16] Scott, J. F.: Applications of modern ferroelectrics. *Science (New York, N.Y.)* **315**, 954–9 (2007).
- [17] Bhatnagar, A., Roy Chaudhuri, A., Heon Kim, Y., Hesse, D. & Alexe, M.: Role of domain walls in the abnormal photovoltaic effect in BiFeO₃. *Nature communications* **4**, 2835 (2013).
- [18] Catalan, G. & Scott, J. F.: Physics and Applications of Bismuth Ferrite. *Adv. Mater.* **21**, 2463–2485 (2009).
- [19] Ederer, C. & Spaldin, N. A.: Weak ferromagnetism and magnetolectric coupling in bismuth ferrite. *Phys. Rev. B* **71**, 60401 (2005).
- [20] Sosnowska, I., Peterlinneumaier, T. & Steichele, E.: Spiral magnetic-ordering in bismuth ferrite. *J. Phys. C: Solid State Phys.* **15**, 4835–4846 (1982).
- [21] Dzyaloshinsky, I.: A thermodynamic theory of weak ferromagnetism of antiferromagnetics. *Journal of Physics and Chemistry of Solids* **4**, 241 – 255 (1958).
- [22] Moriya, T.: New mechanism of anisotropic superexchange interaction. *Phys. Rev. Lett.* **4**, 228–230 (1960).
- [23] Ding, H.-C. C. & Duan, C.-G. G.: Electric-field control of magnetic ordering in the tetragonal-like BiFeO₃. *EPL* **97**, 57007 (2012).

- [24] Lebeugle, D., Colson, D., Forget, A., Viret, M., Bataille, A. M. & Gukasov, A.: Electric-Field-Induced Spin Flop in BiFeO₃ Single Crystals at Room Temperature. *Phys. Rev. Lett.* **100**, 227602 (2008).
- [25] Wang, Y. P., Zhou, L., Zhang, M. F., Chen, X. Y., Liu, J.-M. & Liu, Z. G.: Room-temperature saturated ferroelectric polarization in BiFeO₃ ceramics synthesized by rapid liquid phase sintering. *Appl. Phys. Lett.* **84**, 1731 (2004).
- [26] Popov, Y. F., Kadomtseva, A. M., Krotov, S. S., Belov, D. V., Vorob'ev, G. P., Makhov, P. N. & Zvezdin, A. K.: Features of the magnetoelectric properties of BiFeO₃ in high magnetic fields. *Low Temp. Phys.* **27**, 478–479 (2001).
- [27] Palkar, V. R., Purandare, S. C., Gohil, S., John, J. & Bhattacharya, S.: Scanning probe imaging of coexistent ferromagnetism and ferroelectricity at room temperature. *Appl. Phys. Lett.* **90**, 172901 (2007).
- [28] Petrov, P. K., Palkar, V. R., Tagantsev, A. K., Chien, H.-I., Prashanthi, K., Axelsson, A.-K., Bhattacharya, S. & Alford, N. M.: Dielectric properties characterization of La- and Dy-doped BiFeO₃ thin films. *J. Mater. Res.* **22**, 2179–2184 (2007).
- [29] Béa, H., Bibes, M., Sirena, M., Herranz, G., Bouzehouane, K., Jacquet, E., Fusil, S., Paruch, P., Dawber, M., Contour, J.-P. & Barthélémy, A.: Combining half-metals and multiferroics into epitaxial heterostructures for spintronics. *Appl. Phys. Lett.* **88**, 062502 (2006).
- [30] Eerenstein, W., Morrison, F. D., Dho, J., Blamire, M. G., Scott, J. F. & Mathur, N. D.: Comment on "Epitaxial BiFeO₃ multiferroic thin film heterostructures". *Science (New York, N.Y.)* **307**, 1203; author reply 1203 (2005).
- [31] Béa, H., Bibes, M., Fusil, S., Bouzehouane, K., Jacquet, E., Rode, K., Bencok, P. & Barthélémy, A.: Investigation on the origin of the magnetic moment of BiFeO₃ thin films by advanced x-ray characterizations. *Phys. Rev. B* **74**, 020101 (2006).
- [32] C. P. Hunt, B. M. M. & Banerjee, S. K.: *Rock Physics and Phase Transitions, a Handbook of Physical Constants* (American Geophysical Union, Washington, D.C., 1995).
- [33] Xu, X. S., Brinzari, T. V., Lee, S., Chu, Y. H., Martin, L. W., Kumar, A., McGill, S., Rai, R. C., Ramesh, R., Gopalan, V., Cheong, S. W. & Musfeldt,

- J. L.: Optical properties and magnetochromism in multiferroic BiFeO₃. *Phys. Rev. B* **79**, 134425 (2009).
- [34] Kadomtseva, A. M., Zvezdin, A. K., Popov, Y. F., Pyatakov, A. P. & Vorob'ev, G. P.: Space-time parity violation and magnetoelectric interactions in antiferromagnets. *Journal of Experimental . . .* **79**, 11 (2004).
- [35] Chen, P., Günaydn-en, O., Ren, W. J., Qin, Z., Brinzari, T. V., McGill, S., Cheong, S.-W. & Musfeldt, J. L.: Spin cycloid quenching in Nd³⁺-substituted BiFeO₃. *Phys. Rev. B* **86**, 014407 (2012).
- [36] Cheng, Z. X., Li, a. H., Wang, X. L., Dou, S. X., Ozawa, K., Kimura, H., Zhang, S. J. & Shrout, T. R.: Structure, ferroelectric properties, and magnetic properties of the La-doped bismuth ferrite. *J. Appl. Phys.* **103**, 07E507 (2008).
- [37] Bai, F., Wang, J., Wuttig, M., Li, J., Wang, N., Pyatakov, a. P., Zvezdin, a. K., Cross, L. E. & Viehland, D.: Destruction of spin cycloid in (111)_c-oriented BiFeO₃ thin films by epitaxial constraint: Enhanced polarization and release of latent magnetization. *Appl. Phys. Lett.* **86**, 032511 (2005).
- [38] de Sousa, R., Allen, M. & Cazayous, M.: Theory of Spin-Orbit Enhanced Electric-Field Control of Magnetism in Multiferroic BiFeO₃. *Phys. Rev. Lett.* **110**, 267202 (2013).
- [39] Qi, X., Dho, J., Tomov, R., Blamire, M. G. & MacManus-Driscoll, J. L.: Greatly reduced leakage current and conduction mechanism in aliovalent-ion-doped BiFeO₃. *Appl. Phys. Lett.* **86**, 062903 (2005).
- [40] Petrov, P. K. & Palkar, V. R.: Microwave responce from La- and Dy- doped BiFeO₃ thin films. *Mater. Res. Soc. Symp. Proc.* **966**, 28–33 (2006).
- [41] Mathe, V., Patankar, K., Kothale, M., Kulkarni, S., Joshi, P. & Patil, S.: Preparation, structural analysis and dielectric properties of Bi_xLa_{1-x}FeO₃ perovskite. *Pramana* **58**, 1105–1113 (2002).
- [42] Kim, J. S., Cheon, C. I., Lee, C. H. & Jang, P. W.: Weak ferromagnetism in the ferroelectric BiFeO₃ - ReFeO₃ - BaTiO₃ solid solutions (Re=Dy,La). *J. Appl. Phys.* **96**, 468 (2004).
- [43] Mathe, V., Patankar, K., Patil, R. & Lokhande, C.: Synthesis and dielectric properties of Bi_{1-x}Nd_xFeO₃ perovskites. *J. Magn. Magn. Mater.* **270**, 380–388 (2004).

- [44] Nalwa, K. S. & Garg, A.: Phase evolution, magnetic and electrical properties in Sm-doped bismuth ferrite. *J. Appl. Phys.* **103**, 044101 (2008).
- [45] Uniyal, P. & Yadav, K.: Study of dielectric, magnetic and ferroelectric properties in $\text{Bi}_{1-x}\text{Gd}_x\text{FeO}_3$. *Mater. Lett.* **62**, 2858–2861 (2008).
- [46] Thakuria, P. & Joy, P. A.: High room temperature ferromagnetic moment of Ho substituted nanocrystalline BiFeO_3 . *Appl. Phys. Lett.* **97**, 162504 (2010).
- [47] Prashanthi, K., Chalke, B. A., Barick, K. C., Das, A., Dhiman, I. & Palkar, V. R.: Enhancement in multiferroic properties of $\text{Bi}_{0.7-x}\text{La}_x\text{Dy}_{0.3}\text{FeO}_3$ system with removal of La. *Solid State Commun.* **149**, 188–191 (2009).
- [48] Palkar, V. R., John, J. & Pinto, R.: Observation of saturated polarization and dielectric anomaly in magnetoelectric BiFeO_3 thin films. *Appl. Phys. Lett.* **80**, 1628 (2002).
- [49] Lee, D., Kim, M. G., Ryu, S., Jang, H. M. & Lee, S. G.: Epitaxially grown La-modified BiFeO_3 magnetoferroelectric thin films. *Appl. Phys. Lett.* **86**, 222903 (2005).
- [50] Murashov: Ferromagnetism in crystals of solid solutions $(\text{Bi,Ln})\text{FeO}_3$. *Sov. Phys. Crystallogr.* **35**, 538 (1990).
- [51] Mathe, V. L. & Patankar, K. K.: Studies on structural, dielectric and electrical properties of $\text{Dy}_x\text{Bi}_{1-x}\text{FeO}_3$ solid solutions. *J. Mater. Sci.* **42**, 136–142 (2006).
- [52] Prashanthi, K., Chalke, B. A., Barick, K. C., Das, A., Dhiman, I. & Palkar, V. R.: Enhancement in multiferroic properties of system with removal of La. *Solid State Commun.* **149**, 188–191 (2009).
- [53] Palkar, V. R., Prashanthi, K. & Dattagupta, S. P.: Influence of process-induced stress on multiferroic properties of pulse laser deposited $\text{Bi}_{0.7}\text{Dy}_{0.3}\text{FeO}_3$ thin films. *J. Phys. D: Appl. Phys.* **41**, 045003 (2008).
- [54] Palkar, V. R. & Prashanthi, K.: Observation of magnetoelectric coupling in $\text{Bi}_{0.7}\text{Dy}_{0.3}\text{FeO}_3$ thin films at room temperature. *Appl. Phys. Lett.* **93**, 132906 (2008).
- [55] Zhang, S., Wang, L., Chen, Y., Wang, D., Yao, Y. & Ma, Y.: Observation of room temperature saturated ferroelectric polarization in Dy substituted BiFeO_3 ceramics. *J. Appl. Phys.* **111**, 074105 (2012).

- [56] Barbar, S., Jangid, S., Roy, M. & Chou, F.: Synthesis, structural and electrical properties of $\text{Bi}_{1-x}\text{Dy}_x\text{FeO}_3$ multiferroic ceramics. *Ceram. Int.* **39**, 5359–5363 (2013).
- [57] Kan, D., Cheng, C.-J., Nagarajan, V. & Takeuchi, I.: Composition and temperature-induced structural evolution in La, Sm, and Dy substituted BiFeO_3 epitaxial thin films at morphotropic phase boundaries. *J. Appl. Phys.* **110**, 014106 (2011).
- [58] Uniyal, P. & Yadav, K. L.: Observation of the room temperature magnetoelectric effect in Dy doped BiFeO_3 . *J. Phys.-Condes. Matter* **21**, 12205 (2009).
- [59] Zhu, W.-M., Su, L. W., Ye, Z.-G. & Ren, W.: Enhanced magnetization and polarization in chemically modified multiferroic $(1-x)\text{BiFeO}_3-x\text{DyFeO}_3$ solid solution. *Appl. Phys. Lett.* **94**, 142908 (2009).
- [60] Khomchenko, V. a., Karpinsky, D. V., Kholkin, a. L., Sobolev, N. a., Kakazei, G. N., Araujo, J. P., Troyanchuk, I. O., Costa, B. F. O., Paixao, J. A. & Paixao, J. a.: Rhombohedral-to-orthorhombic transition and multiferroic properties of Dy-substituted BiFeO_3 . *J. Appl. Phys.* **108**, 074109 (2010).
- [61] Tang, Y. H., Han, T. C., Liu, H. L. & Lin, J. G.: Doping Effects on the Magnetoelectricity of Bismuth Ferrite Nanoparticles. *Journal of Superconductivity and Novel Magnetism* **25**, 2753–2755 (2011).
- [62] Kan, D., Pálová, L., Anbusathaiah, V., Cheng, C. J., Fujino, S., Nagarajan, V., Rabe, K. M. & Takeuchi, I.: Universal Behavior and Electric-Field-Induced Structural Transition in Rare-Earth-Substituted BiFeO_3 . *Adv. Funct. Mater.* **20**, 1108–1115 (2010).
- [63] Zhang, S., Yao, Y., Chen, Y., Wang, D., Zhang, X., Awaji, S., Watanabe, K. & Ma, Y.: Effects of magnetic annealing on structure and multiferroic properties of pure and dysprosium substituted BiFeO_3 . *J. Magn. Magn. Mater.* **324**, 2205–2210 (2012).
- [64] Muneeswaran, M. & Giridharan, N. V.: Effect of Dy-substitution on the structural, vibrational, and multiferroic properties of BiFeO_3 nanoparticles. *J. Appl. Phys.* **115**, 214109 (2014).
- [65] Liu, H. L., Su, Y. C., Tang, Y. H. & Lin, J. G.: Variation of the lattice and spin dynamics in $\text{Bi}_{1-x}\text{Dy}_x\text{FeO}_3$ nanoparticles. *J. Appl. Phys.* **115**, 133506 (2014).

- [66] Meštrić, H., Eichel, R.-A., Kloss, T., Dinse, K.-P., Laubach, S., Laubach, S., Schmidt, P., Schönau, K., Knapp, M. & Ehrenberg, H.: Iron-oxygen vacancy defect centers in PbTiO_3 : Newman superposition model analysis and density functional calculations. *Phys. Rev. B* **71**, 134109 (2005).
- [67] Cohen, R. E.: Origin of ferroelectricity in perovskite oxides. *Nature* **358**, 136–138 (1992).
- [68] Ganegoda, H., Kaduk, J. A. & Segre, C. U.: X-ray powder diffraction refinement of $\text{PbTi}_{1-x}\text{Fe}_x\text{O}_{3-\delta}$ solid solution series. *Powder Diffr.* **28**, 238–245 (2013).
- [69] Nelmes, R. & Kuhs, W.: The crystal structure of tetragonal PbTiO_3 at room temperature and at 700 K. *Solid State Commun.* **54**, 721–723 (1985).
- [70] Shannon, R. D.: Revised effective ionic radii and systematic studies of interatomic distances in halides and chalcogenides. *Acta Crystallogr.* **32**, 751–767 (1976).
- [71] Palkar, V. & Malik, S.: Observation of magnetoelectric behavior at room temperature in $\text{Pb}(\text{Fe}_x\text{Ti}_{1-x})\text{O}_3$. *Solid State Commun.* **134**, 783–786 (2005).
- [72] Benguigui, L.: Thermodynamic theory of the morphotropic phase transition tetragonal-rhombohedral in the perovskite ferroelectrics. *Solid State Commun.* **11**, 825 (1972).
- [73] Verma, K. C., Kotnala, R. K. & Negi, N. S.: Improved dielectric and ferromagnetic properties in Fe-doped PbTiO_3 nanoparticles at room temperature. *Appl. Phys. Lett.* **92**, 152902 (2008).
- [74] Ren, Z., Xu, G., Wei, X., Liu, Z., Wang, Y., Xiao, Z., Shen, G. & Han, G.: Ring- and single-crystal-like superstructures of fe-doped pbtio_3 nanocrystals. *J. Cryst. Growth* **311**, 4593–4597 (2009).
- [75] Ren, Z., Xu, G., Wei, X., Liu, Y., Hou, X., Du, P., Weng, W., Shen, G. & Han, G.: Room-temperature ferromagnetism in Fe-doped PbTiO_3 nanocrystals. *Appl. Phys. Lett.* **91**, 063106 (2007).
- [76] Verma, K. C., Kotnala, R. K., Thakur, N., Rangra, V. S. & Negi, N. S.: Resistivity dependent dielectric and magnetic properties of $\text{Pb}(\text{Fe}_{0.012}\text{Ti}_{0.988})\text{O}_3$ nanoparticles. *J. Appl. Phys.* **104**, 093908 (2008).

- [77] Liu, Z., Ren, Z., Wei, X. & Xiao, Z.: Improved Room-Temperature Ferromagnetism in Self-Assembled Disk-Like Superstructures of Fe-Doped PbTiO₃ Nanocrystals. *J. Am. Ceram. Soc.* **93**, 3610–3613 (2010).
- [78] Sun, C., Wang, J., Kang, H., Chen, J., Kim, M. J. & Xing, X.: Ferroelectric and ferromagnetic properties of Pb(Ti_{0.8}Fe_{0.2})O_{3-δ} thin film. *Dalton transactions (Cambridge, England : 2003)* **39**, 9952–5 (2010).
- [79] Sun, C., Cao, Z., Chen, J., Yu, R., Sun, X., Hu, P., Liu, G. & Xing, X.: Negative thermal expansion in the PbTi_{1-x}Fe_xO₃ system. *Physica Status Solidi (B)* **245**, 2520–2523 (2008).
- [80] Schofield, M., Sen, S., Zou, Y., Ray, S., Guptasarma, P., Gajdardziska-Josifovska, M., Chattopadhyay, S., Shibata, T., Balasubramanian, M. & Ren, Y.: High-resolution Transmission Electron Microscopy Study of Compositional Effects on the Atomic Structure of Multiferroic PbTi_{1-x}Fe_xO₃ Nanopowders. *Microsc. Microanal.* **18**, 1896–1897 (2012).
- [81] Eichel, R.-A.: Defect structure of oxide ferroelectrics-valence state, site of incorporation, mechanisms of charge compensation and internal bias fields. *Journal of Electroceramics* **19**, 11–23 (2007).
- [82] Keeble, D. J., Booq, Z. I. Y., Garipov, R. R., Eremkin, V. V. & Smotrakov, V.: Fe³⁺ defect dipole centers in ferroelectric PbTiO₃ studied using electron paramagnetic resonance. *Phys. Rev. B* **80**, 014101 (2009).
- [83] Erdem, E., Kiraz, K., Somer, M. & Eichel, R.-A.: Size effects in Fe³⁺-doped PbTiO₃ nanocrystals - Formation and orientation of defect-dipoles. *J. Eur. Ceram. Soc.* **30**, 289–293 (2010).
- [84] Katsura, H., Balatsky, A. V. & Nagaosa, N.: Dynamical Magnetoelectric Coupling in Helical Magnets. *Phys. Rev. Lett.* **98**, 027203 (2007).
- [85] Cheong, S.-W. & Mostovoy, M.: Multiferroics: a magnetic twist for ferroelectricity. *Nat. Mater.* **6**, 13–20 (2007).
- [86] Basov, D. N., Averitt, R. D., van der Marel, D., Dressel, M. & Haule, K.: Electrodynamics of correlated electron materials. *Rev. Mod. Phys.* **83**, 471–541 (2011).

- [87] Cazayous, M., Gallais, Y., Sacuto, A., De Sousa, R., Lebeugle, D. & Colson, D.: Possible observation of cycloidal electromagnons in BiFeO₃. *Phys. Rev. Lett.* **101**, 037601 (2008).
- [88] Talbayev, D., Trugman, S. A., Balatsky, a. V., Kimura, T., Taylor, a. J. & Averitt, R. D.: Detection of coherent magnons via ultrafast pump-probe reflectance spectroscopy in multiferroic Ba_{0.6}Sr_{1.4}Zn₂Fe₁₂O₂₂. *Phys. Rev. Lett.* **101**, 097603 (2008).
- [89] Kida, N., Takahashi, Y., Lee, J. S., Shimano, R., Yamasaki, Y., Kaneko, Y., Miyahara, S., Furukawa, N., Arima, T. & Tokura, Y.: Terahertz time-domain spectroscopy of electromagnons in multiferroic perovskite manganites. *J. Opt. Soc. Am. B-Opt. Phys.* **26**, A35–A51 (2009).
- [90] Rovillain, P., Sousa, R. D., Gallais, Y., Sacuto, A., Méasson, M. A., Colson, D., Forget, A., Bibes, M., Barthélémy, A., Cazayous, M., De Sousa, R., Méasson, M. A. & Barthélemy, A.: Electric-field control of spin waves at room temperature in multiferroic BiFeO₃. *Nat. Mater.* **9**, 975–979 (2010).
- [91] Talbayev, D., Trugman, S. a., Lee, S., Yi, H. T., Cheong, S.-W. & Taylor, a. J.: Long-wavelength magnetic and magnetoelectric excitations in the ferroelectric antiferromagnet BiFeO₃. *Phys. Rev. B* **83**, 094403 (2011).
- [92] Fox, M.: *Optical Properties of Solids* (Oxford University Press, 2010).
- [93] Singleton, J.: *Band Theory and Electronic Properties of Solids* (Oxford University Press, 2001).
- [94] Blundell, S.: *Magnetism in Condensed Matter* (Oxford University Press, 2001).
- [95] Zhang, Z., Jin, Z., Pan, Q., Xu, Y., Lin, X., Ma, G. & Cheng, Z.: Temperature dependent photoexcited carrier dynamics in multiferroic BiFeO₃ film: A hidden phase transition. *Appl. Phys. Lett.* **104**, 151902 (2014).
- [96] Chen, L. Y., Yang, J. C., Luo, C. W., Laing, C. W., Wu, K. H., Lin, J.-Y., Uen, T. M., Juang, J. Y., Chu, Y. H. & Kobayashi, T.: Ultrafast photoinduced mechanical strain in epitaxial BiFeO₃ thin films. *Appl. Phys. Lett.* **101**, 041902 (2012).
- [97] Pisarev, R. V., Moskvin, a. S., Kalashnikova, A. M. & Rasing, T.: Charge transfer transitions in multiferroic BiFeO₃ and related ferrite insulators. *Phys. Rev. B* **79**, 1–16 (2009).

- [98] Sheu, Y. M., Trugman, S. a., Park, Y.-S., Lee, S., Yi, H. T., Cheong, S.-W., Jia, Q. X., Taylor, a. J. & Prasankumar, R. P.: Ultrafast carrier dynamics and radiative recombination in multiferroic BiFeO₃. *Appl. Phys. Lett.* **100**, 242904 (2012).
- [99] Ruello, P., Pezeril, T., Avanesyan, S., Vaudel, G., Gusev, V., Infante, I. C. & Dkhil, B.: Photoexcitation of gigahertz longitudinal and shear acoustic waves in BiFeO₃ multiferroic single crystal. *Appl. Phys. Lett.* **100**, 212906 (2012).
- [100] Jin, Z. M., Xu, Y., Zhang, Z. B., Li, G. F., Lin, X., Ma, G. H., Cheng, Z. X. & Wang, X. L.: Structural dependent ultrafast electron-phonon coupling in multiferroic BiFeO₃ films. *Appl. Phys. Lett.* **100**, 71105 (2012).
- [101] Chen, L. Y., Yang, J. C., Luo, C. W., Laing, C. W., Wu, K. H., Lin, J., Uen, T. M., Juang, J. Y., Chu, Y. H. & Kobayashi, T.: Ultrafast photoinduced mechanical strain in epitaxial BiFeO₃ thin films. *Appl. Phys. Lett.* **101**, 41902 (2012).
- [102] Doig, K. I., Aguesse, F., Axelsson, a. K., Alford, N. M., Nawaz, S., Palkar, V. R., Jones, S. P. P., Johnson, R. D., Synowicki, R. a. & Lloyd-Hughes, J.: Coherent magnon and acoustic phonon dynamics in tetragonal and rare-earth-doped BiFeO₃ multiferroic thin films. *Phys. Rev. B* **88**, 094425 (2013).
- [103] Rovillain, P., Cazayous, M., Gallais, Y., Sacuto, a., Lobo, R. P. S. M., Lebeugle, D. & Colson, D.: Polar phonons and spin excitations coupling in multiferroic BiFeO₃ crystals. *Phys. Rev. B* **79**, 180411 (2009).
- [104] Ruello, P. & Gusev, V. E.: Physical mechanisms of coherent acoustic phonons generation by ultrafast laser action. *Ultrasonics* (2014).
- [105] Hudert, F., Bartels, a., Dekorsy, T., Kohler, K. & Kohler, K.: Influence of doping profiles on coherent acoustic phonon detection and generation in semiconductors. *J. Appl. Phys.* **104**, 123509 (2008).
- [106] Lim, D., Averitt, R. D., Demsar, J., Taylor, a. J., Hur, N. & Cheong, S. W.: Coherent acoustic phonons in hexagonal manganite LuMnO₃. *Appl. Phys. Lett.* **83**, 4800–4802 (2003).
- [107] Jang, K. J., Lim, J., Ahn, J., Kim, J. H., Yee, K. J., Ahn, J. S. & Cheong, S. W.: Ultrafast ir spectroscopic study of coherent phonons and dynamic spin-lattice coupling in multiferroic LuMnO₃. *New J. Phys.* **12**, 23017 (2010).

- [108] Jang, K. J., Lee, H. G., Lee, S., Ahn, J., Ahn, J. S., Hur, N. & Cheong, S. W.: Strong spin-lattice coupling in multiferroic hexagonal manganite YMnO_3 probed by ultrafast optical spectroscopy. *Appl. Phys. Lett.* **97**, 31914 (2010).
- [109] Thomsen, C., Grahn, H. T., Maris, H. J. & Tauc, J.: Surface generation and detection of phonons by picosecond light pulses. *Phys. Rev. B* **34**, 4129–4138 (1986).
- [110] Sharma, P. a., Ahn, J. S., Hur, N., Park, S., Kim, S. B., Lee, S., Park, J.-G. G., Guha, S. & Cheong, S.-W. W.: Thermal conductivity of geometrically frustrated, ferroelectric YMnO_3 : extraordinary spin-phonon interactions. *Phys. Rev. Lett.* **93**, 177202 (2004).
- [111] Munoz, A., Alonso, J. A., Martinez-lope, M. J., Casais, M. T., Martinez, J. L. & Fernandez-diaz, M. T.: Magnetic structure of hexagonal RMnO_3 ($\text{R} = \text{Y}, \text{Sc}$): thermal evolution from neutron powder diffraction data. *Phys. Rev. B* **62**, 9498–9510 (2000).
- [112] Lee, S., Pirogov, A., Kang, M. S., Jang, K.-H. H., Yonemura, M., Kamiyama, T., Cheong, S.-W. W., Gozzo, F., Shin, N., Kimura, H., Noda, Y. & Park, J.-G. G.: Giant magneto-elastic coupling in multiferroic hexagonal manganites. *Nature* **451**, 805–U4 (2008).
- [113] Lou, S.-T. T., Zimmermann, F. M., Bartynski, R. A., Hur, N. & Cheong, S.-W. W.: Femtosecond laser excitation of coherent optical phonons in ferroelectric LuMnO_3 . *Phys. Rev. B* **79**, 214301 (2009).
- [114] Chen, P., Podraza, N. J., Xu, X. S., Melville, A., Vlahos, E., Gopalan, V., Ramesh, R., Schlom, D. G. & Musfeldt, J. L.: Optical properties of quasi-tetragonal BiFeO_3 thin films. *Appl. Phys. Lett.* **96**, 131907 (2010).
- [115] Ihlefeld, J. F., Podraza, N. J., Liu, Z. K., Rai, R. C., Xu, X., Heeg, T., Chen, Y. B., Li, J., Collins, R. W., Musfeldt, J. L., Pan, X. Q., Schubert, J., Ramesh, R. & Schlom, D. G.: Optical band gap of BiFeO_3 grown by molecular-beam epitaxy. *Appl. Phys. Lett.* **92**, 142908 (2008).
- [116] Fiebig, M., Pavlov, V. V. & Pisarev, R. V.: Second-harmonic generation as a tool for studying electronic and magnetic structures of crystals: review. *Journal of the Optical Society of America B* **22**, 96–118 (2005).

- [117] Degenhardt, C., Fiebig, M., Fröhlich, D., Lottermoser, T. & Pisarev, R.: Non-linear optical spectroscopy of electronic transitions in hexagonal manganites. *Appl. Phys. B* **73**, 139–144 (2001).
- [118] Vasudevarao, A., Kumar, A., Tian, L., Haeni, J. H., Li, Y. L., Eklund, C.-J. J., Jia, Q. X., Uecker, R., Reiche, P., Rabe, K. M., Chen, L. Q., Schlom, D. G. & Gopalan, V.: Multiferroic domain dynamics in strained strontium titanate. *Phys. Rev. Lett.* **97**, 257602 (2006).
- [119] Pimenov, A., Mukhin, A. A., Ivanov, V. Y., Travkin, V. D., Balbashov, a. M. & Loidl, a.: Possible evidence for electromagnons in multiferroic manganites. *Nat. Phys.* **2**, 97–100 (2006).
- [120] Bea, H., Bibes, M., Petit, S., Kreisel, J. & Barthelemy, A.: Structural distortion and magnetism of BiFeO₃ epitaxial thin films: a Raman spectroscopy and neutron diffraction study. *Philos. Mag. Lett.* **87**, 165–174 (2007).
- [121] Kamba, S., Nuzhnyy, D., Savinov, M., Šebek, J., Petzelt, J., Prokleška, J., Haumont, R. & Kreisel, J.: Infrared and terahertz studies of polar phonons and magnetodielectric effect in multiferroic BiFeO₃ ceramics. *Phys. Rev. B* **75**, 1–7 (2007).
- [122] Haumont, R., Kreisel, J., Bouvier, P. & Hippert, F.: Phonon anomalies and the ferroelectric phase transition in multiferroic BiFeO₃. *Phys. Rev. B* **73**, 132101 (2006).
- [123] Singh, M. K., Katiyar, R. S. & Scott, J. F.: New magnetic phase transitions in BiFeO₃. *J. Phys.: Condens. Matter* **20**, 252203 (2008).
- [124] de Sousa, R. & Moore, J.: Optical coupling to spin waves in the cycloidal multiferroic BiFeO₃. *Phys. Rev. B* **77**, 012406 (2008).
- [125] Lobo, R. P. S. M., Moreira, R. L., Lebeugle, D. & Colson, D.: Infrared phonon dynamics of multiferroic BiFeO₃ single crystal. *Phys. Rev. B* **76**, 5 (2007).
- [126] Dekorsy, T., Taubert, R., Hudert, F., Schrenk, G., Barrels, A., Cerna, R., Kotaidis, V. & Plech, A.: High-speed asynchronous optical sampling for high-sensitivity detection of coherent phonons. *J. Phys.: Conf. Ser.* **92**, 012005 (2007).

- [127] Brivio, S., Polli, D., Crespi, A., Osellame, R., Cerullo, G. & Bertacco, R.: Observation of anomalous acoustic phonon dispersion in SrTiO₃ by broadband stimulated Brillouin scattering. *Appl. Phys. Lett.* **98**, 211907 (2011).
- [128] Polyanskiy, M.: Refractive index database. <http://refractiveindex.info/>.
- [129] Institute, I. P.-T.: New semiconductor materials. characteristics and properties. <http://www.ioffe.ru/SVA/NSM/>.
- [130] Jellison, G. E. & Modine, F. a.: Parameterization of the optical functions of amorphous materials in the interband region. *Appl. Phys. Lett.* **69**, 371 (1996).
- [131] Degenhardt, C., Fiebig, M., Frohlich, D., Lottermoser, T., Pisarev, R. V. & Fröhlich, D.: Nonlinear optical spectroscopy of electronic transitions in hexagonal manganites. *Appl. Phys. B-Lasers Opt.* **144**, 139–144 (2001).
- [132] Kumar, A., Denev, S., Zeches, R. J., Vlahos, E., Podraza, N. J., Melville, A., Schlom, D. G., Ramesh, R. & Gopalan, V.: Probing mixed tetragonal/rhombohedral-like monoclinic phases in strained bismuth ferrite films by optical second harmonic generation. *Appl. Phys. Lett.* **97**, 112903 (2010).
- [133] Beard, M. C., Turner, G. M. & Schmuttenmaer, C. A.: Terahertz Spectroscopy. *J. Phys. Chem. B* **106**, 7146–7159 (2002).
- [134] Cook, D. J. & Hochstrasser, R. M.: Intense terahertz pulses by four-wave rectification in air. *Opt. Lett.* **25**, 1210 (2000).
- [135] Nahata, A., Weling, A. S. & Heinz, T. F.: A wideband coherent terahertz spectroscopy system using optical rectification and electro-optic sampling. *Appl. Phys. Lett.* **69**, 2321 (1996).
- [136] Tani, M., Matsuura, S., Sakai, K. & Nakashima, S.-i.: Emission characteristics of photoconductive antennas based on low-temperature-grown GaAs and semi-insulating GaAs. *Appl. Opt.* **36**, 7853 (1997).
- [137] Davies, A. G., Linfield, E. H. & Johnston, M. B.: The development of terahertz sources and their applications. *Phys. Med. Biol.* **47**, 3679–3689 (2002).
- [138] Dai, J., Xie, X. & Zhang, X.-C.: Detection of Broadband Terahertz Waves with a Laser-Induced Plasma in Gases. *Phys. Rev. Lett.* **97**, 103903 (2006).

- [139] QuantumWise: Atomistix ToolKit version 12.2.2, QuantumWise A/S. <http://www.quantumwise.com>.
- [140] Soler, J. M., Artacho, E., Gale, J. D., García, A., Junquera, J., Ordejón, P. & Sánchez-Portal, D.: The SIESTA method for ab initio order- N materials simulation. *J. Phys.: Condens. Matter* **14**, 2745–2779 (2002).
- [141] Du, Y., Cheng, Z. X., Wang, X. L. & Dou, S. X.: Lanthanum doped multiferroic DyFeO₃: Structural and magnetic properties. *J. Appl. Phys.* **107**, 09D908 (2010).
- [142] Chen, L., Li, T., Cao, S., Yuan, S., Hong, F. & Zhang, J.: The role of 4f-electron on spin reorientation transition of NdFeO₃: A first principle study. *J. Appl. Phys.* **111**, 103905 (2012).
- [143] Zdanowicz, M., Harra, J., Mäkelä, J. M., Heinonen, E., Ning, T., Kauranen, M. & Genty, G.: Second-harmonic response of multilayer nanocomposites of silver-decorated nanoparticles and silica. *Scientific reports* **4**, 5745 (2014).
- [144] Kajzar, F., Messier, J., Zyss, J. & Ledoux, I.: Nonlinear interferometry in Langmuir-Blodgett multilayers of polydiacetylene. *Opt. Commun.* **45**, 133–137 (1983).
- [145] Facchetti, A., Annoni, E., Beverina, L., Morone, M., Zhu, P., Marks, T. J. & Pagani, G. A.: Very large electro-optic responses in H-bonded heteroaromatic films grown by physical vapour deposition. *Nat. Mater.* **3**, 910–7 (2004).
- [146] Lloyd-Hughes, J., Jones, S. P. P., Castro-Camus, E., Doig, K. I. & MacManus-Driscoll, J. L.: Modifying the polarization state of terahertz radiation using anisotropic twin-domains in LaAlO₃. *Opt. Lett.* **39**, 1121 (2014).
- [147] Lloyd-Hughes, J.: Generalized conductivity model for polar semiconductors at terahertz frequencies. *Appl. Phys. Lett.* **100**, 122103 (2012).
- [148] Shang, S. L., Sheng, G., Wang, Y., Chen, L. Q. & Liu, Z. K.: Elastic properties of cubic and rhombohedral BiFeO₃ from first-principles calculations. *Phys. Rev. B* **80**, 52102 (2009).
- [149] Newnham, R. E.: *Properties of Materials: Anisotropy, Symmetry, Structure, 1st ed* (Oxford University Press, Oxford, Oxford, UK, 2005).

- [150] Pace, N. G. & Saunders, G. A.: Elastic wave propagation in group-Vb semimetals. *J. Phys. Chem. Solids* **32**, 1585–& (1971).
- [151] Carpenter, M. A., Sinogeikin, S. V., Bass, J. D., Lakshtanov, D. L. & Jacobsen, S. D.: Elastic relaxations associated with the Pm3m-R3c transition in LaAlO(3): I. Single crystal elastic moduli at room temperature. *J. Phys. Condens. Matter* **22**, 035403 (2010).
- [152] Hayward, S. A., Morrison, F. D., Redfern, S. A. T., Salje, E. K. H., Scott, J. F., Knight, K. S., Tarantino, S., Glazer, A. M., Shuvaeva, V., Daniel, P., Zhang, M. & Carpenter, M. A.: Transformation processes in LaAlO₃: Neutron diffraction, dielectric, thermal, optical, and Raman studies. *Phys. Rev. B* **72**, 054110 (2005).
- [153] Dong, H., Chen, C., Wang, S., Duan, W. & Li, J.: Elastic properties of tetragonal BiFeO₃ from first-principles calculations. *Appl. Phys. Lett.* **102**, 182905 (2013).
- [154] Smirnova, E. P., Sotnikov, a., Ktitorov, S., Zaitseva, N., Schmidt, H. & Weihnacht, M.: Acoustic properties of multiferroic BiFeO₃ over the temperature range 4.2-830 K. *The European Physical Journal B* **83**, 39–45 (2011).
- [155] Van Kranendonk, J. & Vleck, V.: Spin Waves. *Rev. Mod. Phys.* **30**, 1–23 (1958).
- [156] Chen, L. Y., Yang, J. C., Shih, H. C., Liang, C. W., Wu, T.-Y. Y., Chou, S. K., Luo, C. W., Wu, K. H., Chu, Y. H. & Kobayashi, T.: Ultrafast Dynamics of BiFeO₃ Thin Films Studied by Dual-Color Femtosecond Spectroscopy. *Journal of Superconductivity and Novel Magnetism* **24**, 731–734 (2010).
- [157] De Sousa, R. & Moore, J. E.: Electrical control of magnon propagation in multiferroic BiFeO₃ films. *Appl. Phys. Lett.* **92**, 22514 (2008).
- [158] Matsuda, M., Fishman, R. S., Hong, T., Lee, C. H., Ushiyama, T., Yanagisawa, Y., Tomioka, Y. & Ito, T.: Magnetic Dispersion and Anisotropy in Multiferroic BiFeO₃. *Phys. Rev. Lett.* **109**, 067205 (2012).
- [159] Abakumov, A. M., Hadermann, J., Batuk, M., D'Hondt, H., Tyablikov, O. A., Rozova, M. G., Pokholok, K. V., Filimonov, D. S., Sheptyakov, D. V., Tsirlin, A. A., Niermann, D., Hemberger, J., Van Tendeloo, G. & Antipov, E. V.: Slicing the perovskite structure with crystallographic shear planes: the A_nB_nO_{3n-2} homologous series. *Inorg. Chem.* **49**, 9508–16 (2010).

- [160] Batuk, M., Turner, S., Abakumov, A. M., Batuk, D., Hadermann, J. & Van Tendeloo, G.: Atomic structure of defects in anion-deficient perovskite-based ferrites with a crystallographic shear structure. *Inorg. Chem.* **53**, 2171–80 (2014).
- [161] Ruddlesden, S. N. & Popper, P.: The compound $\text{Sr}_3\text{Ti}_2\text{O}_7$ and its structure. *Acta Crystallogr.* **11**, 54–55 (1958).
- [162] Lee, C.-H., Orloff, N. D., Birol, T., Zhu, Y., Goian, V., Rocas, E., Haislmaier, R., Vlahos, E., Mundy, J. A., Kourkoutis, L. F., Nie, Y., Biegalski, M. D., Zhang, J., Bernhagen, M., Benedek, N. A., Kim, Y., Brock, J. D., Uecker, R., Xi, X. X., Gopalan, V., Nuzhnyy, D., Kamba, S., Muller, D. A., Takeuchi, I., Booth, J. C., Fennie, C. J. & Schlom, D. G.: Exploiting dimensionality and defect mitigation to create tunable microwave dielectrics. *Nature* **502**, 532–6 (2013).
- [163] Ghosez, P. & Triscone, J.-M.: Multiferroics: Coupling of three lattice instabilities. *Nat. Mater.* **10**, 269–70 (2011).
- [164] Fewster, P. F.: X-ray analysis of thin films and multilayers. *Reports on Progress in Physics* **59**, 1339–1407 (1996).
- [165] Fullerton, E. E., Schuller, I. K., Vanderstraeten, H. & Bruynseraede, Y.: Structural refinement of superlattices from x-ray diffraction. *Phys. Rev. B* **45**, 9292–9310 (1992).
- [166] Takahashi, R., Valset, K., Folven, E., Eberg, E., Grepstad, J. K. & Tybell, T.: Long-range spontaneous structural ordering in barium stannate thin films. *Appl. Phys. Lett.* **97**, 081906 (2010).
- [167] Detemple, E., Ramasse, Q. M., Sigle, W., Cristiani, G., Habermeier, H.-U., Keimer, B. & van Aken, P. A.: Ruddlesden-Popper faults in $\text{LaNiO}_3/\text{LaAlO}_3$ superlattices. *J. Appl. Phys.* **112**, 013509 (2012).
- [168] Björck, M. & Andersson, G.: GenX : an extensible X-ray reflectivity refinement program utilizing differential evolution. *J. Appl. Crystallogr.* **40**, 1174–1178 (2007).
- [169] Alexe, M.: Local mapping of generation and recombination lifetime in BiFeO_3 single crystals by scanning probe photoinduced transient spectroscopy. *Nano Lett.* **12**, 2193–8 (2012).

- [170] Ruppel, W., Von Baltz, R. & Wurfel, P.: The origin of the photo-emf in ferroelectric and non-ferroelectric materials. *Ferroelectrics* **43**, 109–123 (1982).
- [171] Mishina, E. D., Sherstyuk, N. E., Barskiy, D. R., Sigov, A. S., Golovko, Y. I., Mukhorotov, V. M., De Santo, M. & Rasing, T.: Domain orientation in ultrathin (Ba,Sr)TiO₃ films measured by optical second harmonic generation. *J. Appl. Phys.* **93**, 6216 (2003).
- [172] Uhd Jepsen, P., Schairer, W., Libon, I. H., Lemmer, U., Hecker, N. E., Birkholz, M., Lips, K. & Schall, M.: Ultrafast carrier trapping in microcrystalline silicon observed in optical pump-terahertz probe measurements. *Appl. Phys. Lett.* **79**, 1291 (2001).
- [173] Kuzmenko, A.: R e f F I T (2004). <http://optics.unige.ch/alexey/reffit.html>.
- [174] Harbecke, B.: Coherent and incoherent reflection and transmission of multilayer structures. *Applied Physics B Photophysics and Laser Chemistry* **39**, 165–170 (1986).
- [175] Calvani, P., Capizzi, M., Donato, F., Dore, P., Lupi, S., Maselli, P. & Varsamis, C.: Infrared optical properties of perovskite substrates for high-Tc superconducting films. *Physica C: Superconductivity* **181**, 289–295 (1991).
- [176] Shimada, T., Kakimoto, K.-i. & Ohsato, H.: Microwave dielectric properties of lanthanum aluminate ceramics and single crystal. *J. Eur. Ceram. Soc.* **25**, 2901–2905 (2005).
- [177] Ulbricht, R., Hendry, E., Shan, J., Heinz, T. F. & Bonn, M.: Carrier dynamics in semiconductors studied with time-resolved terahertz spectroscopy. *Rev. Mod. Phys.* **83**, 543–586 (2011).
- [178] Lloyd-Hughes, J. & Jeon, T.-I.: A Review of the Terahertz Conductivity of Bulk and Nano-Materials. *J Infrared Milli Terahz Waves* **33**, 871 (2012).
- [179] Merz, E. F. . W. J.: *Ferroelectricity (Selected Topics in Solid State Physics, Volume VII)* (North-Holland Publishing Company, 1967).
- [180] Iliev, M. N., Abrashev, M. V., Mazumdar, D., Shelke, V. & Gupta, A.: Polarized Raman spectroscopy of nearly tetragonal BiFeO₃ thin films. *Phys. Rev. B* **82**, 14107 (2010).

- [181] Foster, C., Li, Z., Grimsditch, M., Chan, S.-K. & Lam, D.: Anharmonicity of the lowest-frequency $A_1(\text{TO})$ phonon in PbTiO_3 . *Phys. Rev. B* **48**, 10160–10167 (1993).
- [182] Vibrationnelle, E. & Strijcturaux, R.: Etude vibrationnelle d'aluminates et de gallates de terres rares - I. Alluminates de structure perovskite. *Spectrochimica Acta Part A: Molecular Spectroscopy* **37**, 985–990 (1981).
- [183] Delugas, P., Fiorentini, V. & Filippetti, A.: Dielectric properties and long-wavelength optical modes of the high- κ oxide LaAlO_3 . *Phys. Rev. B* **71**, 134302 (2005).
- [184] Scott, J.: Raman study of trigonal-cubic phase transitions in rare-earth aluminates. *Phys. Rev.* **557** (1969).
- [185] Abrashev, M. V., Litvinchuk, A. P., Iliev, M. N. & Meng, R. L.: Comparative study of optical phonons in the rhombohedrally. *Phys. Rev. B* **59**, 4146–4153 (1999).
- [186] Solin, S. & Ramdas, A.: Raman spectrum of diamond. *Phys. Rev. B* **1** (1970).
- [187] Temple, P. & Hathaway, C.: Multiphonon Raman spectrum of silicon. *Phys. Rev. B* (1973).